AN INVESTIGATION OF THE EFFECTS OF NOZZLE GUIDE VANE TRAILING EDGE COOLING ON ROTOR HEAT TRANSFER IN A TRANSONIC TURBINE STAGE

by

Aaron J. Gleixner
B.S. Aerospace Engineering
University of Notre Dame (1990)

SUBMITTED IN PARTIAL FULFILLMENT
OF THE REQUIREMENTS OF THE
DEGREE OF

MASTER OF SCIENCE
IN AERONAUTICS AND ASTRONAUTICS

at the
MASSACHUSETTS INSTITUTE OF TECHNOLOGY
September 1992

Signature of Author_____
Department of Aeronautics and Astronautics
August 24, 1992

Certified by_____
Professor Alan H. Epstein
Thesis Supervisor
Department of Aeronautics and Astronautics

Accepted by_____
Professor Harold Y. Wachman
Chairman, Departmental Graduate Committee

An Investigation of the Effects of Nozzle Guide Vane Trailing Edge Cooling on Rotor Heat Transfer in a Transonic Turbine Stage

by

Aaron J. Gleixner

Submitted to the Department of Aeronautics and Astronautics
on August 24, 1992 in partial fulfillment of the
requirements for the degree of Master of Science in
Aeronautics and Astronautics

Abstract

In this study, the effect of nozzle guide vane trailing edge cooling on rotor heat transfer in a transonic turbine stage is investigated. Previous measurements taken in the MIT blowdown turbine facility have shown that nozzle guide vane cooling brings about an increase in the rotor pressure side heat transfer. A computational code (UNSFLO) was used to isolate the cause of the increased heat transfer on the rotor pressure surface.

Two versions of UNSFLO were used so that the relative importance of nozzle guide vane wake temperature versus coolant mass addition on the heat transfer to the rotor could be investigated. The first version of the code did not include mass addition, with the decreased temperature of the wake being simulated by lowering the nozzle guide vane blade temperature. The second version of the code allowed coolant mass addition at the location of the coolant slots on the nozzle guide vane.

The first version of the code did not correctly predict the increase in rotor pressure side Nusselt number due to nozzle guide vane cooling. It was determined that the decreased wake temperature did not alter the shock and wake structures in the flow, and was therefore not responsible for the increased Nusselt number on the rotor.

The second version of the code was able to qualitatively predict the increases in Nusselt number on the rotor. It was found that an inappropriate driving temperature was being used to calculate the Nusselt number, and that when the appropriate driving temperature was used there was only a small increase in the Nusselt numbers on the pressure side of the rotor.

It was determined that the small increases in rotor pressure side heat transfer when injection was added, were due to increased wake thickness and maximum vorticity in the wake. The increase in wake vorticity served to increase the turbulent mixing in the rotor boundary layer during the passing of the wake. In addition, the thickening of the wake exposed the rotor boundary layer to the high turbulence of the wake for a longer period of time. This increase in wake thickness and maximum vorticity was due to a thickening of the nozzle guide vane pressure side boundary layer caused by the addition of the coolant to the boundary layer.

Thesis Supervisor: Dr. Alan H. Epstein
Title: Professor of Aeronautics and Astronautics

This book is dedicated

to

my parents whose constant love and support
have gotten me where I am

and to

my fiancée Heidi
who makes it all worth while

Acknowledgments

As I sit down to write these acknowledgments, it is impossible to remember all of the people who have helped me over the last two years here at MIT. Some have helped me academically, while others have helped me grow in other ways. I hope that I have not forgotten anyone.

I would first like to thank my advisor Professor Alan Epstein, who has guided me through the last two years, and made this paper possible. Without his guidance and suggestions I might never have reached the end.

I would also like to thank Martin Graf who shared in the joyous process of heat flux gauge manufacturing. Without him my first year here would have gone much slower.

While working at the Gas Turbine Laboratory, I have made numerous close friends. Peter Silkowski has been a good friend to me, always there when I needed him. He somehow always manages to keep life interesting, and without him things would have been much more boring. Taras Palczynski was my responsible voice, always making sure that I had things done on time. Without him and his fiancee Tatiana's matchmaking skills, I would never have met my fiancée Heidi. Without Dave Tew, I would be in worse physical shape than I already am. It was he who kept me doing one sport or another, though I never did get very good at any of them. It was Eric Strang who taught me there is more to MIT than books. He was the one who showed me there is more to life than school.

There are many others at the school who have been friends to me over the past two years. Among these are Dan Gysling, Norm Sun, S.J. Song, Knox

Millsaps, and Jon Simon. I would like to thank all of these people who have made my stay here a more enjoyable one.

Finally I would like to thank my family and fiancée, who have always been behind me, and helped me in any way they could. It is their encouragement and persistence that has gotten me through.

My Master's degree here at MIT was made possible by funding from the Air Force Research in Aero Propulsion Technology Scholarship. The project was funded by Rolls Royce Plc. I thank these people for allowing me to advance my education.

Table of Contents

Abstract 2

Acknowledgments 4

Table of Contents 6

List of Figures 9

List of Table 14

Nomenclature 15

Chapter 1 Introduction 17

1.1 Motivation 17

1.2 Governing Equations 18

1.3 Components of Unsteadiness 20

1.3.1 Freestream Turbulence 20

1.3.2 Potential Flow Interactions 22

1.3.3 Wake Interactions 22

1.3.4 Shock Wave Effects 28

1.4 Film Cooling 29

1.5 Previous Work 30

1.6 Present Research Goals 31

Chapter 2 Experimental Facilities and Results 32

2.1 Blowdown Turbine Facility 33

2.1.1 Facility Scaling 33

2.1.2 Facility Hardware 35

2.1.3 Nozzle Guide Vanes 36

2.1.4 Instrumentation 36

2.1.5 Data Acquisition System 38
2.1.6 Pertinent Tests 38
2.2 Blowdown Turbine Results 39
2.2.1 Time-Resolved Measurements 40
Chapter 3 Numerical Predictions 43
3.1 UNSFLO 44
3.1.1 Inviscid Calculations 44
3.1.2 Viscous Calculations 44
3.1.3 Three-Dimensional Effects 45
3.1.4 Nozzle Guide Vane Film Cooling 46
3.2 Code Validation 46
3.2.1 Code Weaknesses for This Application 47
3.3 Test Cases 48
Chapter 4 Computational Results 50
4.1 Version 1 - No Coolant Injection 51
4.1.1 Case 1 (T=0.64) 51
4.1.2 Case 2 (T=0.59) and Case 3 (T=0.45) 52
4.2 Version 2 - Coolant Injection 54
4.2.1 Coolant Injection Results 55
4.2.2 Influence of Coolant Slot Location 55
4.2.3 Effect of Coolant Exit Angle 57
4.2.4 Effect of Increased Ratio of Specific Heats 58
4.2.5 Nusselt Number Time Histories 59
4.2.6 Heat Transfer Time Histories 61
4.2.7 Boundary Layer Profiles 63
4.2.8 Heat Transfer Comparisons 67
4.2.9 Code Shortcomings 68

Chapter 5 Conclusions 70

5.1 Recommendations for Future Work 72

References 74

Figures 77

Tables 155

List of Figures

Chapter 1

Figure 1.1 : Dependence of maximum specific thrust on turbine inlet temperature

Figure 1.2 : Trends in maximum turbine inlet temperature with time [2]

Figure 1.3 : Solution of Orr-Sommerfeld equation for the Falkner-Skan boundary layer profile with various pressure gradients [8]

Figure 1.4 : Effect of varying freestream turbulence on mean rotor heat transfer coefficient [10]

Figure 1.5 : Cutting of the wakes and the associated velocity diagrams showing the wake slip velocity

Figure 1.6 : Circulation pattern between rotor blades due to wake cutting and its associated slip velocity

Figure 1.7 : Use of a "negative jet" to model nozzle guide vane wakes

Figure 1.8 : Drawing of the nozzle guide vane wake / rotor blade interaction at five different time periods for one rotor blade passing

Figure 1.9 : Effect of varying rotor blade incidence on rotor Nusselt number [18]

Figure 1.10 : Time history of the heat transfer for a point on the suction surface for two rotor blade passings showing the transition from laminar to turbulent heat transfer levels due to wake interactions [16]

Figure 1.11 : Time history of the heat transfer for two different points on the suction surface showing the forced transition of the boundary layer due to multiple NGV passings [16]

Figure 1.12 : Effect of wake interactions on rotor Nusselt number for the case of low freestream turbulence [18]

Figure 1.13 : Schlieren photograph of a shock wave impinging on the rotor suction surface and its subsequent reflection back into the flowfield [21]

Figure 1.14 : Time history of the Nusselt number for a point on the rotor suction surface for two rotor blade passings showing the effect of shock waves and wakes on heat transfer [18]

Figure 1.15 : Drawing of shock wave patterns in the MIT blowdown turbine facility for eight different times during one vane passing [19]

Figure 1.16 : Stanton number versus percent wetted surface for nozzle guide vane and no nozzle guide vane cooling by [22]

Chapter 2

Figure 2.1 : Diagram of the blowdown turbine facility

Figure 2.2 : Drawing of the nozzle guide vane profiles, rotor blade profiles, and stage configuration

Figure 2.3 : Velocity triangles for the inlet and outlet of the rotor at the mid-span position

Figure 2.4 : Diagram of the coolant supply facility

Figure 2.5 : Flow path of the coolant gas into the nozzle guide vanes and rotor

Figure 2.6 : Drawing of a nozzle guide vane and the trailing edge cooling slots on the pressure surface

Figure 2.7 : Cross sectional drawing of a heat flux gauge showing the temperature sensors, thin insulating substrate, and adhesive

Figure 2.8 : Drawing of an entire heat flux gauge before mounting on the rotor blade

Figure 2.9 : Diagram of the positions of the heat flux gauges around the rotor

Figure 2.10 : Nusselt number versus fractional wetted surface for nozzle guide vane cooled and uncooled cases in the blowdown turbine facility [19]

Figure 2.11 : Ratio of cooled to uncooled rotor heat transfer for the blowdown turbine and Dunn's [22] results

Figure 2.12 : Nusselt number versus time from the suction surface gauges for the cooled and uncooled nozzle guide vane cases [19]

Figure 2.13 : Nusselt number versus time from the pressure surface gauges for the cooled and uncooled nozzle guide vane cases [19]

Chapter 3

Figure 3.1 : Drawing of the variations in streamtube height through the rotor for constant divergent angles of 0°, 10°, and 20°

Figure 3.2 : Effect of varying streamtube height through the rotor on Nusselt number distributions around the rotor

Figure 3.3 : Comparison of steady UNSFLO calculated Nusselt numbers with UNSFLO calculations by Abhari [19]

Figure 3.4 : Comparison of hade used in current study with that used in the calculations by Abhari [19]

Figure 3.5 : Comparison of Nusselt numbers and surface static pressure distributions for steady UNSFLO calculations by Abhari and experimental data from Ashworth [19]

Figure 3.6 : Blade setup and grid used in UNSFLO calculations

Chapter 4

Figure 4.1 : Comparison of blowdown turbine results with unsteady averaged UNSFLO calculations of Nusselt number for the uncooled nozzle guide vane wall with no coolant injection

Figure 4.2 : Plot of UNSFLO calculated unsteady temperature versus circumferential distance for the cases of uncooled (T=0.64), and cooled (T=0.59), (T=0.45) nozzle guide vane walls with no coolant injection

Figure 4.3 : Drawing of the location of the line probe in Figure 4.2 and Figure 4.4.

Figure 4.4 : Plot of UNSFLO calculated unsteady Mach number versus circumferential distance for the cases of uncooled (T=0.64), and cooled (T=0.59), (T=0.45) nozzle guide vane walls with no coolant injection

Figure 4.5 : Averaged unsteady UNSFLO calculated Nusselt number versus fractional wetted surface for various nozzle guide vane wall temperatures (T=0.64), (T=0.59), and (T=0.45) with no coolant injection

Figure 4.6 : Contour plots of UNSFLO calculated vorticity at an instant in time for various nozzle guide vane wall temperatures (T=0.64), (T=0.59), and (T=0.45) with no coolant injection

Figure 4.7 : Plot of static temperature versus time at the boundary layer edge of Gauge 2 for two NGV blade temperatures (T=0.64) and (T=0.45)

Figure 4.8 : Contour plot of UNSFLO calculated Mach numbers at an instant in time with coolant injection showing injection location and nozzle throat

Figure 4.9 : UNSFLO plot of stage passage length versus passage mass flow with and without nozzle guide vane coolant injection

Figure 4.10 : Averaged unsteady UNSFLO calculated Nusselt number versus fractional wetted surface with and without coolant injection

Figure 4.11 : Contour plot of UNSFLO calculated Mach numbers at an instant in time with downstream coolant injection showing injection location and nozzle throat

Figure 4.12: Averaged unsteady UNSFLO calculated Nusselt number versus fractional wetted surface for the upstream and downstream slot locations

Figure 4.13 : Line probe of UNSFLO calculated averaged unsteady vorticity versus circumferential distance at the interface of the stator and rotor grids

Figure 4.14 : Contour plots of UNSFLO calculated pressure at an instant in time for the upstream and downstream injection locations

Figure 4.15 : UNSFLO plot of stage passage length versus passage mass flow for the upstream and downstream injection locations

Figure 4.16 : Averaged unsteady UNSFLO calculated Nusselt number versus fractional wetted surface for the cases of 0 and 45 degree injection angles

Figure 4.17 : Contour plots of UNSFLO calculated vorticity at an instant in time for the cases of 0 and 45 degree injection angles

Figure 4.18 : Averaged unsteady UNSFLO calculated Nusselt number versus fractional wetted surface for the ratio of specific heats of 1.28 and 1.29 with coolant injection in both cases

Figure 4.19 : UNSFLO calculated time histories of Nusselt number at the five gauge locations on the rotor pressure surface comparing the injection and no injection cases

Figure 4.20 : Averaged unsteady UNSFLO calculated heat transfer versus fractional wetted surface with and without coolant injection

Figure 4.21 : Averaged unsteady UNSFLO calculated temperature versus circumferential distance at the locations of the five rotor pressure side gauges for one rotor blade passage

Figure 4.22 : UNSFLO calculated time histories of heat transfer at the five gauge locations on the rotor pressure surface comparing the injection and no injection cases

Figure 4.23 : UNSFLO calculated time history of heat transfer at the Gauge 2 location on the rotor pressure surface comparing the injection and no injection cases

Figure 4.24 : Contour plots of UNSFLO calculated vorticity at an instant in time at the nozzle guide vane trailing edge for the injection and no injection cases

Figure 4.25 : Boundary layer profile plot of turbulent viscosity versus distance from the blade surface to the first grid point off the wall for four instants in time for the injection and no injection cases

Figure 4.26 : Boundary layer profile plot of vorticity versus distance from the blade surface to the first grid point off the wall for four instants in time for the injection and no injection cases

Figure 4.27 : Line probe of UNSFLO calculated averaged unsteady vorticity versus circumferential distance at the interface of the stator and rotor grids

Figure 4.28 : Contour plot of UNSFLO calculated vorticity at an instant in time for the injection and no injection cases (Time=1)

Figure 4.29 : Contour plot of UNSFLO calculated vorticity at an instant in time for the injection and no injection cases (Time=2)

Figure 4.30 : Contour plot of UNSFLO calculated vorticity at an instant in time for the injection and no injection cases (Time=3)

Figure 4.31 : Contour plot of UNSFLO calculated vorticity at an instant in time for the injection and no injection cases (Time=4)

Figure 4.32 : Boundary layer profile plot of temperature versus distance from the blade surface to the first grid point off the wall for four instants in time for the injection and no injection cases

Figure 4.33 : Averaged unsteady heat transfer versus fractional wetted surface with and without coolant injection for UNSFLO calculated and experimental results

Figure 4.34 : Averaged unsteady heat transfer versus fractional wetted surface with and without coolant injection for UNSFLO calculated and experimental results where the rotor blade temperature is now matched in UNSFLO to the experimental blade temperature instead of design conditions

List of Tables

Chapter 2

Table 2.1 : MIT blowdown turbine facility scaling

Table 2.2 : MIT blowdown turbine facility instrumentation

Table 2.3 : Heat flux gauge locations at mid-span (uncooled blade) [19]

Table 2.4 : Data acquisition timing sequence for the high speed channels

Table 2.5a : Test parameters for the uncooled nozzle guide vane tests at mid-span [19]

Table 2.5b : Ensemble averaged Nusselt numbers and their associated uncertainty for each gauge of the uncooled nozzle guide vane tests at mid-span [19]

Table 2.6a : Test parameters for the cooled nozzle guide vane tests at mid-span [19]

Table 2.6b : Ensemble averaged Nusselt numbers and their associated uncertainty for each gauge of the cooled nozzle guide vane tests at mid-span [19]

Chapter 3

Table 3.1 : Test parameters used by UNSFLO to compare the effect of hade on rotor Nusselt number

Chapter 4

Table 4.1 : UNSFLO input parameters for the no injection cases

Table 4.2 : UNSFLO input parameters for the coolant injection cases

Nomenclature

α	real component of the perturbation potential
a	speed of sound
c	thermal capacity of kapton
c_p	specific heat at constant pressure
c_v	specific heat at constant volume
d	kapton thickness
D	cooling hole diameter
ϕ	perturbation potential
Φ	viscous-dissipation function
F	thrust
γ	ratio of specific heats
g	gravitational acceleration
h	height
k	thermal conductivity
l	Prandtl mixing length
μ	static viscosity
μ_t	turbulent viscosity
m	mass flux
M	Mach number
P	pressure
Pr	Prandtl number
Pr_t	turbulent Prandtl number
q	heat transfer per unit area
ρ	density
R	Reynolds number
t	time
T	temperature
Tu	turbulence intensity
U	freestream velocity

V	velocity
ω	imaginary component of the perturbation potential
ω	frequency of unsteadiness in reduced frequency
ω	vorticity
Ω	reduced frequency
y	normal distance from blade surface

Subscripts:

0	mean conditions
T_4	total rotor inlet

Chapter 1
Introduction

1.1 Motivation

Since the advent of the gas turbine engine, continuous advances have been made in improving the specific thrust of these engines, due to increases in engine pressure ratio and turbine inlet temperature. The effect of increasing turbine inlet temperature on specific thrust can be seen in the following equation for the maximum specific thrust of an ideal turbojet [1]:

$$\left(\frac{F}{\dot{m}}\right)_{max} = a_0\left\{\left[\left(\frac{2}{\gamma-1}\right)\left(\sqrt{\frac{T_{T4}}{T_0}}-1\right)^2 + M_0^2\right]^{\frac{1}{2}} - M_0\right\} \qquad (1.1.1)$$

where a_0, T_0, and M_0 are the ambient values of speed of sound, temperature, and Mach number respectively, and T_{T4} is the turbine inlet temperature. From the above equation it is apparent that increasing the turbine inlet temperature will raise the specific thrust of the ideal turbojet. This dependence of maximum specific thrust on turbine inlet temperature is illustrated in Figure (1.1) for an ideal engine.

Increases in turbine inlet temperature over the years have resulted from both advances in blade materials used, and the use of air-cooled blading. Figure (1.2) shows the increases in turbine inlet temperature with time [2]. From this figure the increase in

turbine inlet temperature due to blade cooling can be seen. It is important to note the large increase in turbine inlet temperature for the cooled blade (1500 K) versus the uncooled blade (800 K). This shows the necessity of using blade cooling in today's gas turbines.

This need for increasing turbine inlet temperature by using blade cooling is what drives the large amounts of research done in this area today. Many methods of blade cooling have been proposed, such as internal cooling using air or water, and film cooling [3]. For aircraft engines, the high mass of water disqualifies its use for internal cooling. This means that air bled from the compressor must be used. Current research centers around minimizing the amount of air needed for cooling to increase cycle efficiency, and minimizing the temperature gradients in the blade in order to reduce the thermal stresses. Reduction of thermal stresses in the blades is important for increasing fatigue life, especially in rotor blades.

1.2 Governing Equations

In order to predict the heat transfer to a blade, the dynamics of the flow around the blade must first be known. The flow can be described using the equation of state and conservation of mass, momentum, and energy. These vector equations in Cartesian coordinates are as follows [4]:

State:

$$f(P,T,\rho) = 0 \tag{1.2.1}$$

Mass:

$$\frac{D\rho}{Dt} + \rho \nabla \cdot \mathbf{V} = 0 \tag{1.2.2}$$

Momentum:

$$\rho \frac{D\mathbf{V}}{Dt} = -\rho g \nabla h - \nabla p + \mu \nabla^2 \mathbf{V} + \frac{\mu}{3} \nabla(\nabla \cdot \mathbf{V}) \tag{1.2.3}$$

Energy:

$$\rho c_v \frac{DT}{Dt} = k\nabla^2 T - p\nabla \cdot \mathbf{V} + \Phi \qquad (1.2.4)$$

Where:

$$\Phi = 2\mu\left[\left(\frac{\partial u}{\partial x}\right)^2 + \left(\frac{\partial v}{\partial y}\right)^2 + \left(\frac{\partial w}{\partial z}\right)^2 + \frac{1}{2}\left(\frac{\partial u}{\partial y} + \frac{\partial v}{\partial x}\right)^2 + \frac{1}{2}\left(\frac{\partial v}{\partial z} + \frac{\partial w}{\partial y}\right)^2 + \frac{1}{2}\left(\frac{\partial u}{\partial z} + \frac{\partial w}{\partial x}\right)^2\right]$$

$$\frac{D\mathbf{V}}{Dt} = \frac{\partial \mathbf{V}}{\partial t} + (\mathbf{V}\cdot\nabla)\mathbf{V}$$

$$\nabla p = \left(\frac{\partial p}{\partial x}, \frac{\partial p}{\partial y}, \frac{\partial p}{\partial z}\right)$$

Here, ρ=density, $\mathbf{V}$ (u,v,w) is the velocity vector, t=time, p=pressure, μ=viscosity, c_V=specific heat capacity at constant volume, k=conductivity, T=temperature, and (x,y,z) are the Cartesian coordinates. The above equations hold for an isotropic, Newtonian fluid.

For a majority of the flow, the inertial terms dominate over the viscous terms, and the flow can be considered inviscid. This allows the above governing equations to be simplified considerably. For high Reynolds number flow like that found in a turbine, the effect of viscosity is confined to a very thin layer close to the blade [5]. It is only in this thin boundary layer that the effects of viscosity must be considered. Inside this boundary layer, certain simplifications in the conservation equations may again be made due to the large velocity gradients across the boundary layer relative to the gradients in the streamwise direction. This boundary layer portion of the flow field may be coupled with the inviscid portion, so that the entire flow field can be solved.

1.3 Components of Unsteadiness

In the typical gas turbine, there are numerous phenomena which contribute to general flow unsteadiness. Among the most important of these in the transonic turbine section are freestream turbulence, potential flow interactions, wake interactions, and shock waves. The freestream turbulence is due to events upstream of the turbine, while potential flow interactions, wake interactions and propagating shock waves result from the moving rotor passing behind a stationary vane.

1.3.1 Freestream Turbulence

Freestream turbulence is a result of turbulent mixing in the combustor, and the magnitude of this turbulence is typically around 15-20% leaving the combustor [6]. This turbulence intensity (RMS of velocity fluctuations divided by freestream velocity) is reduced in the nozzle guide vanes to a value of 3-5% entering the rotor. Increases in freestream turbulence change both the flowfield and the heat transfer to the blade.

Freestream turbulence plays a large role in the location and length of the transition region from laminar to turbulent flow around the blade. Using linear perturbation theory it is found that the flow becomes unstable at a critical Reynolds number given by the two-dimensional Orr-Sommerfeld equation. This equation which is derived from the basic equations of motion is as follows [7]:

$$\left(U-\frac{\omega}{\alpha}\right)\left(\frac{d^2\phi}{dy^2}-\alpha^2\phi\right)-\frac{d^2U}{dy^2}\phi-\frac{1}{i\alpha R}\left(\frac{d^2}{dy^2}-\alpha^2\right)^2\phi=0 \qquad (1.3.1)$$

Where:

U is the mean laminar velocity profile, R is the Reynolds number, and $\phi = \phi(y)\exp[i(\alpha x - \omega t)]$ is the disturbance expanded in a Fourier series with α being the real component, and ω the complex component. The imaginary component of ω

determines whether the perturbations are amplified or damped, so that if ω_i is less than zero, the disturbance is damped, while if ω_i is greater than zero, the disturbance amplifies and the flow eventually becomes turbulent. In figure (1.3) the lines of neutral stability from the Orr-Sommerfeld equation are graphed for the Falkner-Skan boundary layer profile with various pressure gradients [8]. These lines represent the points where flow disturbances will neither amplify nor dampen. For Reynolds numbers to the left of these lines, the disturbances are dampened, and the flow will remain laminar. For Reynolds numbers to the right of these lines, the flow is unstable, and the disturbances known as Tollmein-Schlichting waves will grow and become three-dimensional. From this graph, it can be seen that the critical Reynolds number for a flow with no pressure gradient is approximately 520. This Reynolds number is based on the displacement thickness of the boundary layer. For flow with low levels of freestream turbulence, the Reynolds number at which transition occurs on a flat plate is much higher ($R \cong 2900$) than the critical Reynolds number. As the level of freestream turbulence increases, larger disturbances are present, and the Reynolds number at which transition occurs approaches the critical Reynolds number calculated by the Orr-Sommerfeld equation. On a rotor, this means that for the case of low freestream turbulence ($Tu<0.8\%$) both the pressure and suction sides of the blade are predominantly laminar, while when high freestream turbulence is present ($Tu \cong 3\%$), both the pressure and suction sides are predominantly turbulent [9].

The change in the location of transition due to varying levels of freestream turbulence has a noticeable effect on the heat transfer to the blade. In figure (1.4) the increase in heat transfer coefficient due to increased freestream turbulence levels can be observed from measurements taken by Wittig et al [10]. This graph shows the transition point moving forward on the blade as freestream turbulence is increased. The resulting increase in heat transfer due to the transition to a turbulent boundary layer can also be observed. It is also interesting to note the increase in heat transfer at the

stagnation point due to increasing freestream turbulence. When looking at figure (1.4) it is important to remember that these results are for a rotor bladerow only. The effect of freestream turbulence in an actual gas turbine will not be as large, due to the forced transition of the rotor blade caused by nozzle guide vane wakes, impinging shocks, etc.

1.3.2 Potential Flow Interactions

Due to the close proximity of the rotor blades relative to the stator blades, the inviscid flow field around each blade affects, and is affected by the flow fields of the upstream and downstream bladerows. Calculations by Kemp and Sears [11] for a two-dimensional, incompressible flow show that the effect of this potential flow interaction on the downstream rotor blade is small, while the effect on the upstream stator may be important. The potential flow unsteadiness decays exponentially as you move downstream, so that for gas turbine engines the distance between successive stator and rotor bladerows is large enough that the potential flow effect of the stator is negligible. While the effect of the rotor potential flow on the nozzle guide vanes may not be negligible in a subsonic turbine stage, this is not true for a transonic turbine stage such as the MIT blowdown turbine facility since the exit of the nozzle guide vanes is choked. The supersonic flow conditions at the nozzle guide vane exit ensures that the pressure field from the downstream rotor does not have a major effect on the upstream vanes.

1.3.3 Wake Interactions

A large amount of experimental and theoretical work has been done concerning the effect of upstream stator wakes on the flowfield and heat transfer to downstream rotor blades. The wake leaving the stator is characterized by a region of high turbulence intensity, and a mean velocity profile which is less than the freestream velocity. In addition, if the blades are cooled a decreased temperature profile can be found in the wake. This decrease in wake temperature is due to the decreased coolant

temperature which is located in the wake. As the wake is shed from the stator, it travels downstream and is cut by the rotating rotor. The velocity deficit in the wake decreases the effective angle of incidence inside the wake, and introduces a wake "slip" velocity which was verified experimentally by Kerrebrock and Mikolajczak [12] in a compressor. Figure (1.5) illustrates the cutting of the wakes by the rotor, and shows the wake "slip" velocity vector due to the velocity deficit in the wake. This "slip" velocity causes the wake flow to migrate from the pressure side to the suction side of the turbine blade. The flow migration inside the wake causes two counter rotating circulation regions to develop between adjacent blades, where outside the wake, flow migrates from the suction side to the pressure side. These circulation regions are plotted in figure (1.6). In this figure, the unsteady velocity vectors are drawn so that the counter rotating vortices can be seen. These unsteady velocity vectors are defined as the absolute total minus relative mean velocity . The relative frame of reference changes from the nozzle guide vane reference frame to the rotor reference frame at the point midway between the NGV and rotor, and can be seen by the abrupt change in the unsteady velocity vectors. The absolute frame of reference is the NGV frame of reference. A contour plot of the entropy was also overlaid so that the wake region could be identified. This wake region is highlighted in black. The center of the counter rotating vortices is located in the middle of the wake region. This circulation causes the wake to be diminished on the blade pressure side, while accumulating wake material on the suction surface [13]. This circulation pattern allows the wake to be modeled as a "negative jet " [14]. Experiments performed by Hodson [15] validate the accuracy of this model for predicting flow trends due to wakes. Figure (1.7) illustrates the use of a "negative jet" to model the wake.

Once the wake is cut by the leading edge of the rotor blade, the wake travels along both the suction and pressure surfaces. The high level of freestream turbulence in the wake causes transition of the boundary layer as it passes over the blade. The

boundary layer returns to the laminar state once the wake has passed. This may not be true however if the subsequent wake interacts before the boundary layer has time to return to the laminar state. Work by Doorly and Oldfield [16] has shown that the wake causes the suction side boundary layer to remain turbulent at all times after approximately the 30 percent wetted surface location. On the suction surface, the trailing edge of the wake in the boundary layer travels at approximately one half the freestream velocity, while the rate of travel of the leading edge of the wake is much harder to determine [16]. The rate at which the leading edge of the wake propagates in the boundary layer is harder to determine due to the greater rate at which the wake proceeds in the freestream. The wake in the freestream injects turbulence ahead of the wake traveling in the boundary layer thereby making it hard to determine the beginning of the boundary layer wake. It is known however that the leading edge of the wake in the boundary layer is propagating at a speed greater than the trailing edge of the wake. This propagation rate has been measured to be around 0.88-1.0 times the freestream velocity [9]. This propagation rate is slightly higher than propagation rate measured by Ashworth et. al. [17], which showed the propagation rate to be approximately 0.9 times the freestream velocity at the blade leading edge and decreasing to around 0.7 times the freestream velocity at the 50 percent wetted surface location. This means that the wake is being stretched along the suction surface of the blade. Due to the stretching of the wake and the slow speed at which it travels, the boundary layer on the suction surface is interacting with successive nozzle guide vane wakes through most of the blade passing. On the pressure surface, only a small portion of the blade is being affected by the wake at a specified time. As with the suction surface, the wake on the pressure surface is stretched as it travels along the blade. The passing of the wake on the pressure surface can most easily be seen by the temporary transition of the boundary layer from laminar to turbulent as the wake passes. The effect of the wake on the pressure side of the blade should have a dependence on wake thickness, due to the longer amount of time which a

thicker wake will be traveling over the blade. This should not be so for the suction surface, due to the constant interaction between wake and boundary layer. In Figure (1.8) the wake blade interaction is drawn for five different times during one blade passing. This figure was generated using the code UNSFLO which will be discussed in Chapter 3. Once again, regions of high entropy are contour plotted and outlined in black so that the wakes can be seen. From this figure, the cutting of the wake, along with the stretching of the wake along the blade can be seen. The migration of the wake from the pressure to suction side is also noticeable, especially for the time periods Time=0.8 and Time=1.0 where the wake is no longer contacting the pressure surface.

In order to determine the influence of periodic unsteadiness on the flowfield, it is important to compare the time scale of the unsteadiness with the convection time scale of the unsteadiness through the rotor passage. This ratio of the two is called the reduced frequency and is as follows:

$$\frac{(\text{Length Scale})(\text{Frequency of Unsteadiness})}{(\text{Throughflow Velocity})} = \frac{C\omega}{U} = \Omega \qquad (1.3.2)$$

where the rotor axial chord is used for the length scale. In the case of wake passings, the frequency of the unsteadiness is the number of nozzle guide vane passings per second. For the MIT blowdown turbine facility, the reduced frequency of the unsteadiness caused by the nozzle guide vane wakes was calculated to be approximately 1.1. This reduced frequency shows that the periodic unsteadiness due to the wakes is important.

When looking at the effect of wakes on rotor heat transfer, two opposing phenomena must be considered. The first phenomena is the decrease in incidence inside the wake due to the wake slip velocity. The effect of incidence on rotor Nusselt number was measured experimentally by Ashworth et. al. [18] in a cascade, and the results can be found in Figure (1.9). These measurements were repeated by Abhari [19] in the MIT blowdown turbine facility and the results were found to agree with those of

Ashworth. The decrease in incidence caused by the wake tends to lower the Nusselt number on the suction surface, while the Nusselt number on the pressure surface remains approximately constant. This is due to the large changes in Mach number near the leading edge of the suction surface.

The second phenomena is the high level of freestream turbulence in the wake. This freestream turbulence causes the boundary layer to temporarily transition from laminar to turbulent as the wake passes. Experimental studies by Doorly and Oldfield [16] show the effect of a passing wake on the heat transfer at the 25 percent wetted surface point on the suction surface of a rotor. Figure (1.10) shows the transition of the boundary layer from the laminar to turbulent heat transfer level as the wake passes, and the subsequent relaminarization after the wake has passed. It should be noted that this experiment was performed with one wake passing, and the effect of multiple wakes are not taken into account. In an actual stator-rotor arrangement, the effects of multiple wakes interacting with each other on the suction surface may prevent the boundary layer from completely returning to the laminar state before the next wake causes the boundary layer to again return to the turbulent state. In Figure (1.11a), the heat transfer time history is given for a gauge located at the 25 percent wetted surface location on the suction surface with the test parameters identical to those in Figure (1.10). In this figure however, the frequency of wake passings is set to match an actual gas turbine. From this figure, it can be seen that successive wake interactions keep the boundary layer turbulent for a majority of the time with the boundary layer returning to the laminar state for only a small fraction of time before the next wake interacts. Figure (1.11b) shows the heat transfer time history at the 50 percent wetted surface location on the suction surface for the same test as that in Figure (1.11a). This figure shows that by the 50 percent wetted surface location on the suction surface, successive wakes have merged, and the boundary layer remains turbulent at all times. In the same experiment

without wake interactions, the boundary layer was found to remain laminar until well beyond this point on the blade.

When the effects of decreased incidence and increased turbulence in the wake are superimposed, it is found that the effect of increased turbulence is dominant. Figure (1.12) shows the increase in Nusselt number due to wake interactions for the case of low (Tu≅0.8%) freestream turbulence [18]. From this figure it can be seen that the freestream turbulence of the wake forces transition to occur earlier along the blade on the suction surface. This means the Nusselt number on the suction side is at turbulent levels starting at about 10 percent wetted surface when wakes are present, versus a transition to turbulent levels of heat transfer at about 70 percent wetted surface for the no wake case. At approximately the 70 percent wetted surface location on the suction surface, both the wake and no wake cases exhibit turbulent levels of heat transfer, so the effect of the wake is no longer noticeable. On the pressure surface, transition to turbulent levels of heat transfer again occurs earlier when wakes are present. At about the 50 percent wetted surface location on the pressure surface, the no wake case transitions to turbulent levels of heat transfer, and both the wake and no wake cases exhibit similar levels of heat transfer. For the case with wakes, the pressure side boundary layer transitions at about the 10 percent wetted surface location. It is interesting to note that the stagnation point heat transfer is approximately 30 percent greater for the wake case than for the no wake case. This higher level of heat transfer is due to the period of time that the boundary layer is turbulent due to the wake passing. This increase in heat transfer at the stagnation point will vary depending on the thickness of the wake and the percentage of time per wake passing that this point is in the wake.

1.3.4 Shock Wave Effects

For the case of a transonic turbine, the flow is accelerated to supersonic conditions in the nozzle guide vanes. In addition, the flow is accelerated to supersonic conditions near the exit of the rotor in the rotor frame of reference. This means that a number of shock waves are being formed which vary both the flow field and heat transfer to the rotor. It should be noted that the results given below are for a given blade geometry, and the shock patterns will vary depending on the shape of the blade. The shock waves originate at the trailing edge of both the nozzle guide vane and rotor, and propagate until reflecting from a surrounding blade. The strength of these shocks is dependent on the nozzle guide vane exit Mach number. The shock continues to propagate and reflect off successive blades, each time becoming weaker until the effect of the shock becomes negligible. This shock wave pattern changes with time due to the movement of the rotor relative to the nozzle guide vane.

In experiments conducted in a transonic cascade with upstream moving bars to simulate wakes by Ashworth et. al. [18], it was found that the shock from the nozzle guide vane trailing edge impinges on the suction surface point of maximum rotor blade thickness, and moves forward along the blade to the leading edge. In Figure (1.13) a Schlieren photograph was taken of the shocking impinging on the suction surface and reflecting back into the flowfield. Figure (1.14) gives a Nusselt number time history for a point at 25 percent wetted surface on the suction surface. This time history displays the wake and no wake cases. In the figure, the Nusselt number due to shock impingement initially drops to almost zero, and then jumps to a value over three times the no wake case. The initial drop in Nusselt number is due to boundary layer separation caused by the shock, with the following jump in Nusselt number due to turbulent reattachment. After the shock has passed, the boundary layer returns to its original laminar state. In similar work done by Abhari et.al. [20] using identical blading in a three-dimensional rotating facility, similar results were found. In this study

however, the effects of secondary or reflected shocks on heat transfer can also be seen. Figure (1.15) illustrates the shock wave pattern found by Abhari at eight different times during one vane passing [19]. These shock wave patterns were found using UNSFLO. From this figure, the complexity of the shock wave patterns can be observed.

A theoretical model by Johnson et. al. [21] can be used to predict the effect of impinging shocks on rotor heat transfer. This model involves rapid variation of pressure in the boundary layer close to the blade. This rapid variation in pressure heats the boundary layer by adiabatic compression, thereby producing large temperature gradients in the region close to the blade. These large temperature gradients produce the high rates of heat transfer in the laminar sublayer of the boundary layer that are characteristic of shock wave passings. By measuring the rapidly changing pressure distribution around the blade caused by the shock, the unsteady heat flux was found. The results of this model were found to be in good agreement with experiments taken in a cascade with upstream rotating bars.

1.4 Film Cooling

As discussed earlier, the use of blade film cooling greatly increases the maximum allowable turbine inlet temperature and therefore is a necessity in today's gas turbine engines. Film cooling involves the addition of a secondary coolant to the boundary layer through small holes or slots in the blade. This mass addition to the boundary layer thickens the layer, and reduces the heat transfer to the blade. This secondary coolant is bled from the high pressure compressor, and therefore must be minimized for maximum efficiency. Because the bled air is much cooler than the turbine gases, it can first be used to internally cool the blade. If film cooling is to be used effectively, its effect on the flowfield must be known. In particular, when film cooling is used, additional mass is added to the flowfield which changes the wake and

shock structures interacting with the blades downstream. It is important to know the location where the coolant is added, since addition upstream of the nozzle guide vane throat may have an altogether different effect than coolant added downstream of the throat. In some cases this can have a detrimental effect on the heat transfer and efficiency of the downstream blades. It is for this reason that a detailed knowledge of the coolant flowfield must be known, along with its effect on stator/rotor interactions.

1.5 Previous Work

The effect of nozzle guide vane cooling on rotor heat transfer has been experimentally investigated by Dunn [22] on a Garrett TFE 731-2 hp rotor. In this experiment, the coolant was added through slots on the pressure surface of the nozzle guide vanes at the 63 percent wetted surface location versus the NGV trailing edge for the MIT blowdown turbine facility. Figure (1.16) shows Dunn's heat transfer results in the form of Stanton numbers for no nozzle guide vane cooling, and NGV cooling at two different coolant temperatures. From this figure, it can be seen that the effect of adding nozzle guide vane cooling is to increase the Stanton number over much of the rotor surface; however the reader should keep in mind that this increase is usually not larger than the error bars. It should be noted that there is no portion of the rotor on which the Stanton number decreases when NGV cooling is added. The largest increases in Stanton number due to cooling occur at the leading edge, and the first 20 percent of the suction side wetted surface. At the leading edge, the Stanton number for the injected case is about 18 percent higher than for the no injection case. This increase in Stanton number do to blade cooling becomes approximately 35 percent at the 5 percent wetted surface location on the suction surface, with increases of 9 and 13 percent at the 18 and 20 percent locations respectively. For the remainder of the suction surface, and the first 30 percent of the pressure surface, the influence of nozzle guide vane cooling on

Stanton number is relatively small. From about the 30 percent wetted surface location on the pressure side, the effect of NGV cooling on Stanton number increases along the pressure surface to the trailing edge. The increase in Stanton number due to blade cooling is around 2 percent at the 30 percent wetted surface location on the pressure surface, and increases to approximately 8 percent at the 90 percent wetted surface location. It can also be noted from the figure that coolant temperature plays a relatively small role on the Stanton number.

1.6 Present Research Goals

All of the components of unsteadiness mentioned in the previous sections have an effect on the heat transfer to the rotor. When film cooling is added, the effects of these various forms of unsteadiness can change. This paper will concentrate on nozzle guide vane cooling and its effect on the heat transfer to the downstream rotor. The changes in the various unsteady components due to film cooling will be investigated, and their effect on the heat transfer will be determined. In particular, the experimental results of Abhari [19] will be compared with numerical simulations in a study of increased rotor heat transfer due to nozzle guide vane cooling.

To complete these investigations, a combination of experimental data and numerical calculations will be used. Chapter 2 will provide a brief overview of the experimental facilities used by Abhari [19] to obtain the rotor heat transfer data, and the results of these experiments will be presented. Chapter 3 will cover the numerical code UNSFLO which was used to calculate the flowfield and explain the experimental results. In Chapter 4, the numerical code UNSFLO will be used to help explain the experimental results presented in Chapter 2.

Chapter 2

Experimental Facilities and Results

The experimental results used in this paper were obtained from the MIT blowdown turbine (BDT) facility by R. Abhari [19]. The first part of this chapter will provide a basic overview of the facilities and instrumentation, and the reader is advised to see [23] for a more thorough description. This short duration (0.3 s) test facility is a fully rotational three-dimensional transonic single stage (NGV and rotor) rig, in which actual engine conditions are correctly simulated. Due to the high cost and complexity of using an actual engine for testing, the BDT was designed as a scaled down short duration facility in which most of the aerodynamic and heat transfer phenomena are correctly simulated. The lower operating temperature of the BDT facility makes instrumentation much easier than for an actual engine. This relative ease of instrumentation allows for greater resolution of the measurements, and is well suited for the limited resources available at the university level.

In the second part of the chapter, the results of both the cooled and uncooled nozzle guide vane blowdown turbine tests will be presented, and compared with the results of Dunn which were presented in the first chapter. This comparison will serve to validate the experimental results obtained in the blowdown turbine facility. A comparison of the MIT blowdown turbine cooled versus uncooled nozzle guide vane tests will then be made, so that the effect of nozzle guide vane cooling on rotor heat transfer can be observed. In both this chapter and Chapter 4, Nusselt number plots will be plotted versus rotor fractional wetted surface, with zero percent wetted surface

corresponding to the stagnation point on the rotor, and the suction surface labeled as negative fractional wetted surface. In each case, the heat transfer will be presented in terms of the non-dimensional Nusselt number based on rotor axial chord, inlet rotor relative total minus local blade temperature, and a thermal conductivity based on the local blade temperature unless otherwise specified. The local blade temperatures used were those temperatures measured by the top sensor of the heat flux gauges. For the case of coolant injection, the inlet relative total temperature to the rotor is mass averaged to include the coolant temperature.

2.1 Blowdown Turbine Facility

2.1.1 Facility Scaling

Due to the need for a scaled down facility for cost and complexity reasons, the blowdown turbine facility has a smaller rotor and power output than for a full size engine. If the aerodynamic flowfield and heat transfer distribution in the stage are to be correctly modeled, certain non-dimensional parameters must be matched. These non-dimensional parameters are determined from the non-dimensional governing equations (1.2.1-1.2.4), and were determined to be Reynolds number, corrected speed, corrected mass flow, Prandtl number, ratio of specific heats, and gas to metal temperature ratios [24]. If these above parameters are the same in the blowdown turbine facility as in an actual engine, the fluid flow and heat transfer will be correctly modeled. In order to correctly model these parameters for a smaller geometry facility, certain changes had to be made. The high gas temperature of actual engines makes the testing much more complicated, so reducing the gas temperature in the BDT facility was of primary importance. For correct simulation of the heat transfer, the blade wall temperature also had to be reduced, for the gas to wall temperature ratio to remain constant. For this facility, the blade temperature was set at room temperature, and was assumed constant

throughout the short duration of the test. This set the required gas temperature. The lower operating temperature decreases both the pressure and rotational speed requirements due to matching of the Reynolds number and corrected speed respectively. The ratio of specific heats must also be matched. In order to do this while still keeping other non-dimensional parameters constant, a mixture of Argon-Freon 12 was used. The higher molecular weight of this gas with respect to air allows for the pressure in the supply tank to be lowered for Reynolds number matching, in addition to reducing the speed of sound of the gas. This reduction in the speed of sound means that the rotational speed of the rotor can be much slower in order to keep the tip Mach numbers the same. Table (2.1) shows the scaling of the facility. From this table it can be observed that the size, rotational speed, temperature, pressure, and power output of the blowdown turbine are much less than for an actual engine. This greatly reduces the cost and complexity of testing.

For tests with film cooling, additional non-dimensional parameters must be matched. In order for the film cooling in the blowdown turbine to correctly model cooling in an actual engine, the coolant to main flow mass flux, the coolant to metal temperature ratio, the coolant to main flow momentum ratio, and the coolant ratio of specific heats must be matched [19]. In order to maintain the correct coolant to main flow mass flux, a blowdown facility was designed for the coolant system. This would allow the decay in main flow mass flux over the period of the test to be matched with a similar decay in coolant flow to keep the mass flux ratio constant. The temperature of the cooling gas is set by the required coolant to rotor blade temperature ratio. Because the rotor blade temperature in the blowdown turbine facility is room temperature, a cryogenic gas was needed at 200° K. To get the required ratio of specific heats, a mixture of Argon-Freon 14 was used. Freon 14 was chosen so that condensation of the gas would not occur at the high pressures and low temperatures in the coolant supply tank.

2.1.2 Facility Hardware

The blowdown turbine facility is composed of four main parts; the tanks and fast acting valve, the test section, the eddy current brake, and the coolant supply facility. A diagram of the facility is given in Figure (2.1). From this figure you can see the supply tank is upstream of the fast acting valve. Downstream of the valve is the test section followed by the dump tank. To the side, the coolant tank and associated hardware are drawn. This coolant tank provides the coolant air for tests with blade cooling.

The axial turbine stage which was used is highly loaded (pressure ratio=4.5:1), with the rotor diameter being scaled down to 0.55 m. The stage has been designed by Rolls-Royce Plc., and is called the Advanced Core Engine (ACE). The blade profiles and stage configuration are drawn in Figure (2.2), with 36 nozzle guide vanes and 61 rotor blades per stage. For blade coordinates the reader is advised to see Ashworth [25]. This stage is transonic, with the nozzle guide vanes being choked. The nozzle guide vane and rotor relative exit Mach numbers are 1.22 and 1.10 respectively. This choking of the nozzle guide vanes provides for a constant corrected mass flow throughout the test. The velocity triangles for the inlet and exit of the rotor at midspan are given in Figure (2.3).

The coolant supply facility consists of a coolant supply tank, fast acting valve, and an orifice plate. A diagram of this facility is drawn in Figure (2.4). When the valve is opened, the coolant gas travels through a downstream orifice plate. This orifice is choked, with the discharge hole size set by the supply tank size and the need for a given coolant mass flow decay rate. After passing through the orifice plate, the gas travels to internal nozzle guide vane plenums and the rotor disc plenum. The coolant gas is then discharged through the holes in the blade. In Figure (2.5) the coolant gas path into the nozzle guide vanes can be seen. Because this paper deals with nozzle guide vane

cooling only, the data which is used was taken with the passage to the rotor blades blocked.

2.1.3 Nozzle Guide Vanes

The cooled nozzle guide vanes were designed to simulate the effect of a cooled NGV without the complexity of the cooling holes normally found in a cooled vane. Trailing edge slots were used in place on these cooling holes. Work done by Goldstein et. al. [26] shows that for positions far downstream of the cooling holes ($x/D > 6$) where D is the cooling hole diameter, the effect of film cooling holes can be modeled with an equivalent slot. Because these experiments are concerned with rotor heat transfer, a slot was used instead of the cooling holes since the rotor is located far enough downstream of the nozzle guide vanes. This slot served to model the nozzle guide vane trailing edge slot normally found on the NGV, in addition to modeling the cooling holes at the front of the nozzle guide vane. Figure (2.6) shows the nozzle guide vane used, and the cooling slots on the trailing edge of the pressure surface. For the tests, a mass flow rate of approximately 3.0 % of the main flow was used. This number was chosen to correctly match the coolant to main flow mass flux. In order to determine the state of the coolant gas as it exits the NGV blade, a Kulite pressure transducer and thermocouple were located in the NGV coolant plenum. This allowed for the density of the gas to be found and therefore the coolant exit velocity to be calculated. It was assumed that the coolant exit velocity was injected into the main flow at an angle of 45 degrees to the blade at the location of the cooling slots. It was found that the coolant gas velocity was around 80% of the main flow velocity for the design case.

2.1.4 Instrumentation

Due to the short duration of the experiment, and the need to resolve individual blade passings, there is a need for high speed instrumentation and the associated high

speed data acquisition system. A summary of the instrumentation can be found in Table (2.2). The pressure measurements were taken with Kulite differential transducers, with the exception of the coolant total pressure transducer on the rotor, which was taken with an absolute transducer. For temperature measurements, two different types of sensors were used. Most of the sensors were commercially available J and K type thermocouples. A limited number of resistance thermometers were also used. These resistance thermometers are both platinum and ceramic type sensors.

One of the primary objectives of the blowdown turbine facility is the detailed measurement of unsteady heat flux to the turbine stage. In designing heat flux gauges for this facility, a number of criteria were defined. The first is the ability of the gauge to withstand the relatively high (500° K) gas temperature of the facility. The gauge is also required to endure the high centrifugal forces imposed by rotation on the rotor. Due to the resolution in heat flux required, a large number of gauges need to be placed on the relatively small space of the rotor, in addition to having a frequency response ranging from steady state to ten times the blade passing frequency. Finally, the gauges must not significantly alter the flowfield and heat transfer to the blade.

The type of gauge which was designed to satisfy these criteria was a thin filmed multilayer gauge, in which two temperature sensors, one on either side of a thin insulating substrate, is applied to the blade surface. A drawing of the gauge layers can be seen in Figure (2.7). These gauges were designed by Guenette [27] for the blowdown turbine facility. The thinness of the gauges and their ability to assume the blade shape once applied, provide minimal disturbances to the flowfield and heat transfer to the blade.

The heat flux gauges consist of two nickel temperature sensors ($\approx 10^{-7}$ m thick) deposited on a piece of thin polyamide insulator or Kapton ($\approx 25 \times 10^{-6}$ m thick). The nickel temperature sensors are in a serpentine pattern covering an area of 1.3×10^{-6} m^2. A drawing of the entire gauge is located in Figure (2.8). The gauge positions on the

rotor blade can be found in Figure (2.9) for the mid-span blade, while the gauge locations can be found in Table (2.3). Heat flux measurements are non-dimensionalized and presented as Nusselt number distributions. These heat flux measurements were ensemble averaged with respect to the nozzle guide vane passing for 10 rotor revolutions.

2.1.5 Data Acquisition System

The data acquisition system consists of forty five high speed channels, four sixteen channel multiplexers, thirty two megabyte solid state (RAM) memory unit, digital clock, digital counter, and controlling microprocessor. The high speed channels are 12 bit channels with 200 KHz per channel maximum sampling rate. For the current tests these channels are reserved for the heat flux sensors and tachometers. Sixty four low speed channels are also created by multiplexing sixteen low speed channels on each of four high speed channels. The data acquisition system is controlled by the microprocessor which in turn is programmed interactively on a VAX workstation. One of the functions of the microprocessor is the programming of the digital clock for four different sampling rates throughout the test. Due to limited memory, the sampling rate must be reduced during certain portions of the test. Table (2.4) shows the sampling rates for various portions of the test. Once the test has been completed, the data is transferred from the memory unit to a MicroVax for storage and analysis.

2.1.6 Pertinent Tests

The experiments of interest to this paper are the uncooled rotor case with and without nozzle guide vane cooling. In both cases only the blade mid-span results will be considered. The same instrumented blade was used for both the cooled and uncooled nozzle guide vane cases, with the manufacturing of the blade done by Dr. J.

Guenette. The uncooled nozzle guide vane tests were performed by Dr. Guenette, while the cooled tests were performed by Dr. R. Abhari. [19]

The uncooled nozzle guide vane tests at mid-span are numbered T47, T50, T51, T52, and T53, where test T47 corresponds to the facility design conditions. The test parameters for these runs can be found in Table (2.5a), while the measured Nusselt numbers and their associated uncertainty can be found in Table (2.5b). Similarly, the cooled nozzle guide vane tests at mid-span are numbered T55, T56, T57, T60, and T61. The test parameters for these runs are located in Table (2.6a), while the measured Nusselt numbers and their associated uncertainty are located in Table (2.6b).

2.2 Blowdown Turbine Results

A number of tests were performed by Abhari [19] in the Blowdown Turbine facility for both the cooled and uncooled nozzle guide vane cases. Figure (2.10) shows the Nusselt number distribution at design conditions for the uncooled (T47) and cooled (T56) cases, and the associated uncertainty of the measurements. For the cooled test case (T56), the temperature of the coolant is identical to the rotor blade temperature. From this figure it is interesting to note than at the leading edge and the first 30 percent of the suction surface, the Nusselt number with NGV cooling is lower than without cooling. On the pressure surface, the nozzle guide vane cooling increased the Nusselt number starting at about 30 percent wetted surface, with the largest difference at the trailing edge.

While the heat transfer trends on the pressure surface agree well with Dunn's results from Chapter 1, the effects of nozzle guide vane cooling on the suction surface heat transfer are in disagreement. Dunn shows a considerable increase in heat transfer at the leading edge and first 20 percent of the suction surface, while the blowdown turbine results show exactly the opposite effect. In Chapter 1 it was shown that the heat

transfer over the first 30 percent of the rotor suction surface was greatly influenced by the impinging shock wave shed at the nozzle guide vane trailing edge. The strength and location of this shock is dependent on blade geometry and the location of coolant injection. The difference in these two parameters between the two tests may explain the differences in suction side heat transfer due to NGV cooling. In the next chapter the numerical code UNSFLO will be used to examine the location and strength of this shock in order to test the validity of this argument. In order to better compare the results of Dunn and the blowdown turbine, a plot of the ratio of cooled to uncooled heat transfer over the rotor surface for both experiments is presented in Figure (2.11).

2.2.1 Time-Resolved Measurements

To explain the results above, the components of unsteadiness discussed in Chapter 1 must be considered. When nozzle guide vane cooling is used, the mass of the coolant is being added to the flow. This mass addition will serve to thicken the NGV wake, which will in turn affect the strength and location of the impinging shocks since the Mach number near the injection point is close to one. Work done by Witteg et al. [10] shows that increasing the wake thickness by 65 percent increases the rotor pressure surface heat transfer by approximately 35 percent, while also increasing the suction side heat transfer over the first 50 percent wetted surface. The reader should keep in mind that these tests were for a single stationary blade upstream of the rotor. The results of Dunn are in agreement with those of Witteg, while the blowdown turbine results differ for the suction side of the rotor.

In order to examine the effect of variations in shock wave impingement on suction side heat transfer for the NGV cooled and uncooled cases, plots of Nusselt number versus time for the suction surface gauges over three blade passings are given in Figures (2.12a) through (2.12f). In Figure (2.12b) there is a large difference in Nusselt number between the cooled and uncooled cases. These differences occur at the

points of maximum Nusselt number, which correspond with shock wave passings. This tends to indicate that a change in shock strength is responsible for the changes in Nusselt number. When coolant is added to the main flow, the coolant mass addition causes blockage of the main flow. In a supersonic flow like that found at the exit of the nozzle guide vanes, this blockage serves to lower the main flow Mach number. Because the strength of the nozzle guide vane trailing edge shock is dependent on the Mach number, this decrease in Mach number decreases the strength of the shock. This decreased shock strength would then lower heat transfer due to a shock wave passing. It can also be noticed that aft of the point of blade maximum thickness, the Nusselt number is unaffected by NGV cooling. This is due to the absence of the impinging shock, which impinges at the point of maximum thickness and moves forward. Figures (2.12d) through (2.12f) show that the shock is no longer present, and that the effect of the thicker wake is negligible. This negligible wake effect is reasonable because it was shown in Chapter 1 that the rear portion of the suction surface boundary layer is constantly being affected by the wake regardless of its thickness.

Figures (2.13a) through (2.13f) are plots of Nusselt number versus time for the pressure surface gauges over three blade passings. Both the cooled and uncooled nozzle guide vane cases are plotted. On this side of the blade the effect of impingement shock wave variations on Nusselt number is negligible. It can be noticed from the figures that the Nusselt number for the cooled NGV case is about the same as the uncooled case near the leading edge, but the difference between the two cases gradually becomes larger as you move towards the blade trailing edge. A possible explanation for this phenomena is the stretching of the wake as it moves along the pressure surface. It was shown in Chapter 1 that the leading edge of the wake travels faster than the trailing edge, resulting in a stretching of the wake. For the case of nozzle guide vane cooling, the wake is thicker, and therefore will cause a point on the pressure surface to be affected for a longer period of time by the highly turbulent wake. Because of the

high levels of turbulence in the wake, the Nusselt number at a point on the blade is increased over the period of time when the point is affected by the wake. Figures (2.13c) through (2.13e) show a uniform offset of the cooled case with respect to the uncooled case. If a thickening of the wake was causing the increase in Nusselt number, the Nusselt number levels should be identical between the wakes, assuming the boundary layer has time to return to the laminar state before the passing of the next wake. The Nusselt number levels are not identical between the wakes however, which would suggest that a thickening of the wake is not responsible for the increased Nusselt number with nozzle guide vane cooling.

Chapter 3

Numerical Procedure

While the experimental results presented in the last chapter provide information about the heat flux to the rotor, these results are only measured at the discreet points on the blade where the gauges are located. These experimental results can show the effect of varying a test parameter on the heat flux to the rotor, however the experimental data provides little information as to why the heat flux has changed. It is difficult to infer the changes in the unsteady external flow from the measured unsteady changes in heat flux to the blade. In order to explain why the heat transfer has changed when a test parameter is varied, a computational fluid dynamics (CFD) code has been used in this study. This code is capable of estimating the flowfield around the blade so that the heat transfer to the blade can be calculated. This calculated heat transfer can then be compared with the experimental results, and the calculated flowfield used to explain features in the experimental measurements. The results in following chapters will show that this CFD code is a powerful tool for both explaining the results of the experimental measurements, and predicting the changes in rotor heat transfer when changes in the test parameters are made. This chapter will be concerned with providing a basic understanding of the code, along with its strengths and limitations. In addition, a validation case will be presented to show the validity of the computational technique.

3.1 UNSFLO

The computational fluid dynamics code which has been developed is a compressible, quasi-three dimensional, Reynolds-averaged, unsteady, multi-bladerow, viscous code called UNSFLO. This code was developed by Giles, and the reader is advised to see [28] for a more detailed description than is given in this chapter. The code is unusual in that it uses a hybrid Navier-Stokes / Euler method to increase computational efficiency, while also using a space-time coordinate transformation to allow for computation of stator/rotor interactions with arbitrary pitch ratio.

3.1.1 Inviscid Calculations

Due to the complexity and computation time needed to solve the full Navier-Stokes equations for the entire flowfield, the inviscid section of the flowfield is solved using the Euler equations. The flow can be treated as inviscid in every part of the flowfield with the exception of the thin shear layer around the blade. In this viscous region the flowfield must be solved using the Navier-Stokes equations which will be dealt with in the next section. The inviscid grid is an unstructured finite-element type mesh composed of an arbitrary mix of quadrilateral and triangular cells. The Euler equations are solved using a Ni-type Lax-Wendroff algorithm [29].

3.1.2 Viscous Calculations

For the region close to the blade, the flowfield must be solved using viscous calculations. The grid which is used in this thin shear layer region is a structured O-type mesh which must encompass the entire boundary layer. This grid must also have a large number of mesh points so that the details of the boundary layer can be resolved. The flowfield is solved using the unsteady Reynolds-averaged Navier-Stokes equations.

The Reynolds-averaging provides the mean effect of turbulence over the short turbulence time scales, while ignoring the longer scale turbulence due to wakes and the stator / rotor interaction. The Baldwin-Lomax algebraic turbulence model is used to model the Reynolds stresses caused by the short time scale turbulence [30]. This algebraic turbulence model requires the user to set the beginning and end point of transition.

3.1.3 Three-Dimensional Effects

In order to obtain the correct inlet and outlet mach numbers for the blowdown turbine facility in chapter 2, a quasi-three dimensional solution was needed. UNSFLO has the ability to take into account the effect of varying streamtube height in the third dimension (also known as hade, or axial velocity density ratio, AVDR). The streamtube height variation which was used, was based on the streamline curvature calculations for the tests parameters in the BDT. To test the effect of varying streamtube height on the rotor heat transfer, three different cases were run. All three cases involved a constant divergent angle of the streamtube height through the rotor, with these angles being 0°, 10°, and 20°. The cases used the same test parameters, which were obtained for a typical run of the blowdown turbine facility. These test parameters can be found in Table (3.1). Figure (3.1) shows the variation in streamtube height through the rotor for these three cases. In Figure (3.2) the Nusselt number distributions around the rotor blade can be found. From this figure you notice the largest variations occur near the front of the suction surface, and near the rear of the pressure surface. The changes on the suction surface are due to the variations in Mach number brought about by different streamtube heights.

3.1.4 Nozzle Guide Vane Film Cooling

Two versions of UNSFLO were used to examine the experimental data. The first version did not include coolant injection, and was used to determine the effect of varying nozzle guide vane wake temperature on the rotor heat transfer. A second version was written which allowed for coolant injection. This new code allows for the user to specify the location and amount of coolant to be added to the main flow. The number, size, and location of coolant slots are specified by the user. In addition, the mass flux, velocity, and enthalpy of the coolant flow need to be specified. This code is capable of modeling some aspects of coolant mass addition to the flow, and therefore does a much better job of predicting the effect of NGV film cooling on rotor heat transfer.

3.2 Code Validation

Before UNSFLO can be used to predict the flow field and heat flux in a turbine stage, the code must be validated. To do this, the UNSFLO calculations were compared with UNSFLO calculations by Abhari [19] for a typical run of the blowdown turbine facility. The input parameters used in the calculations can be found in Table (3.1). Figure (3.3) is a plot of steady state Nusselt number versus fractional wetted surface for the present calculations, and the calculations done by Abhari. In this figure you can see the Nusselt numbers are approximately the same for the two cases. The small differences over the first 10 percent of the suction surface and 40 percent of the pressure surface are due to small differences in hade between the two cases. Figure (3.4) is a plot of hade versus passage length for the present results and those of Abhari [19]. From this plot you can see the small differences in the hade specifications.

The validation of UNSFLO by Abhari [19] was done by comparing the calculated results with experimental data taken by Ashworth et al. [18] in a cascade rig

with equivalent blade geometry to that of the blowdown turbine facility. For this case, the streamtube height was set at a constant divergence angle of 10 degrees to match the cascade geometry. Figure (3.5a) is a plot of steady state Nusselt number comparing Abhari's computational results with the experimental data of Ashworth [19] for the cases of high and low freestream turbulence. In this figure you can see that UNSFLO does a good job of matching the turbulent data, when the boundary layer has been specified to be turbulent over the entire rotor. An overprediction occurs over the first 40 percent of the suction surface, but it would appear that this is due to the boundary layer in the experimental data staying laminar until transition to a turbulent state around the 40 percent wetted surface location. In Figure (3.5b) the static pressure distribution around the rotor calculated by Abhari is compared with the experimental results of Ashworth [19]. In this figure you can see that UNSFLO does an excellent job of matching the static pressure distribution.

3.2.1 Code Weaknesses for This Application

As you can see from the previous section, the code does a reasonably good job of predicting the heat transfer to a rotor. One feature which the code has, is the turbulence model's inability to predict the transition point on the suction surface of the rotor blade. The beginning and end of transition must be specified by the user. For a rotor experiencing high freestream turbulence, the transition point is set at the leading edge. For cases of low freestream turbulence, the transition point must be determined from experimental results. Fortunately this is not an important issue here since the rotor sees a high turbulence intensity level. Another problem with the use of an algebraic turbulence model, is its calculation of local turbulent viscosity based on the instantaneous local velocity profile. The turbulence model has no history effects, and responds instantaneously to any changes in the external flow. In the actual flow, the turbulence has a physical time constant.

The code also has no way of taking into account the effect of freestream turbulence. There is no coupling of the freestream turbulence into the boundary layer. This means that the freestream turbulence in the wakes is not present. This absence of freestream turbulence in the wakes will tend to lessen the turbulent mixing in the boundary layer when the wake comes in contact with the rotor. This will result in an underprediction of the turbulent viscosity and therefore the heat transfer to the rotor for the period of time when the rotor is affected by the wake.

Another weakness of the code is the inviscid treatment of the nozzle guide vane wakes. Due to the inviscid nature of the wake, the wake does not decay as it propagates downstream.

3.3 Test Cases

Two versions of UNSFLO were used to solve a number of different test cases. For all of these cases, two rotor blades and four nozzle guide vanes were used. In addition, the same grid was used for each case. The grid consisted of approximately 16,000 points. The inviscid portion of the grid contains 100 and 80 grid points in the direction of flow with 34 and 16 grid points normal to the flow for each stator and rotor blade passage respectively. In the viscous grid there are 18 grid points across the boundary layer for both the stator and rotor blades. Figure (3.6) shows the blade setup and grid used for the calculations. Initially the steady state solution was calculated, where the average nozzle guide vane exit flux components were iterated to match the average rotor inlet components. The unsteady solution was then calculated for each case, taking into account the different number of stators and rotors. The calculations were done on a Stellar GS1000 super-mini computer and took about 20 hours to solve the unsteady solution for one case.

The plotting program GRAFIC [31] was used to visualize the main flow and surface quantities for the steady solution. The unsteady solution was visualized using VISUAL 2 [32]. This program allowed the solution to be visualized using color contour plotting. The variables of Mach number, temperature, pressure, entropy, etc. in the flowfield can be contour plotted along with the various surface quantities. The color contour plots allow the various surface quantities to be explained and linked to the features of the flow. The contour plots also allow for the visualization of wake-rotor interactions and shock wave patterns.

Chapter 4

Computational Results

In Chapter 2, experimental results from the blowdown turbine facility showed that the observed effect of nozzle guide vane cooling was to decrease the Nusselt number over the first 30 percent of the suction surface, while increasing the Nusselt number over the aft 70 percent of the pressure surface. In this chapter the numerical code UNSFLO will be used to calculate the entire stage flowfield, as well as predict the Nusselt number. These predictions will be compared to the experimental results of Chapter 2, and the code will be used to explain the effect of nozzle guide vane cooling on rotor heat transfer.

Two versions of the code were used. The first version did not include coolant mass injection, thus the effect of wake cooling but not blockage effects could be simulated by lowering the nozzle guide vane blade temperature. This did not change the shape of the wake, but rather lowered the wake temperature, allowing for the effect of wake temperature on rotor heat transfer to be investigated. The second version of the code included coolant mass injection, where the user was able to specify the amount, location, velocity, and enthalpy of the coolant gas. This version with mass addition simulates film cooling in an actual engine much more accurately than the first version. The mass addition serves to thicken the nozzle guide vane wake. This dual code version approach permitted exploration of the relative importance of wake temperature

versus coolant mass addition on the heat transfer to the rotor due to nozzle guide vane cooling.

4.1 Version 1 - No Coolant Injection

For this version of the code with no coolant mass injection, three cases were run. The first case (T=0.64) corresponds to an uncooled nozzle guide vane, where T is the ratio of vane temperature to stator inlet total temperature. This is the blade to gas temperature ratio measured in the blowdown turbine experiments with no film cooling. This case was used to compare the results from UNSFLO with the no coolant injection results from the last chapter. In the second case (T=0.59), the nozzle guide vane temperature was matched with the coolant temperature actually achieved in the blowdown turbine experiments. This case was used to model the cooled wake, and the results were compared with the coolant injection results of the last chapter. The final case (T=0.45) which was run, matched the vane temperature to the coolant gas temperature at the correct coolant gas to main gas temperature ratio at engine design conditions.

4.1.1 Case 1 (T=0.64)

In order to test the validity of using UNSFLO to predict the heat transfer to the rotor, the nozzle guide vane temperature was set to match the vane temperature in the blowdown turbine tests with no coolant injection. All of the other experimental test parameters were matched by UNSFLO as well. The UNSFLO input parameters for the no injection cases are listed in Table (4.1). Figure (4.1) is a plot of calculated averaged unsteady Nusselt number versus fractional wetted surface for the rotor. The experimental results included in this figure were averaged over approximately 20 rotor

revolutions or 720 nozzle guide vane passings. In this figure and all the figures to follow, the rotor boundary layer has been set to be fully turbulent over the entire chord. The nozzle guide vane boundary layer has been set to transition from laminar to turbulent at about 50 percent wetted surface on the suction side, and about 70 percent wetted surface on the pressure side. These transition locations were determined from measurements taken on the nozzle guide vanes in the blowdown turbine facility.

This figure shows that UNSFLO slightly overpredicts the pressure side heat transfer, while overpredicting the heat transfer at the leading edge by about 20 percent. The code also underpredicts the heat transfer over the first 30 to 50 percent of the suction surface. It is interesting to note that on the initial portion of the suction surface, UNSFLO is underpredicting the heat transfer, even though the rotor boundary layer has been specified fully turbulent. Figure (3.2) showed that the first 30 percent of the suction surface is very sensitive to changes in streamtube height. There is no reason to believe that this influence of streamtube height on rotor Nusselt number is linear. Due to the unsteady nature of the stator/rotor combination, the true streamtube height is varying with time. This means that the influence of streamtube height on rotor Nusselt number could be a first order effect, and therefore be responsible for the underprediction of the rotor Nusselt number over the first 30 percent of the suction surface.

4.1.2 Case 2 (T=0.59) and Case 3 (T=0.45)

For these two cases, the temperature of the nozzle guide vane has been lowered to simulate NGV coolant injection. In case 2 (T=0.59), the NGV blade temperature was set to match the coolant temperature achieved in the blowdown turbine experiments, while in case 3 (T=0.45), the NGV blade temperature was set at the engine design coolant temperature. This difference in coolant temperature was due to

the inability of the blowdown turbine coolant supply facility at that time to bring the cryogenic coolant gas down to the required temperature.

Figure (4.2) is a plot of averaged unsteady NGV relative static temperature versus circumferential distance where the temperature is non-dimensionalized by the inlet total temperature. The plot consists of two nozzle guide vane passings, and is axially located at the interface of the stator and rotor grids. The location of this line probe is drawn in Figure (4.3). Referring again to Figure (4.2), the position of the wake is marked, so that the drop in wake temperature due to nozzle guide vane cooling can be seen. For case 3 (T=0.45) the wake temperature is around 4 percent lower than for the uncooled blade case (T=0.64). The mass averaged decrease in total temperature due to the cooled NGV for the entire flow is approximately 0.5 percent. Figure (4.4) is a similar plot, where the averaged unsteady Mach number is plotted versus circumferential distance at the same axial location. This plot shows that the Mach number distribution is unaffected by nozzle guide vane wake temperature. In the next section it will be shown that mass injection is required to affect the Mach number distribution. Figure (4.5) is a plot of the calculated averaged unsteady Nusselt number versus fractional wetted surface for the three cases. From this figure it can be seen that the effect of wake temperature on Nusselt number is negligible compared to the experimental findings.

In order to explain why wake temperature does not have an effect on the Nusselt number distribution around the rotor, the unsteady solution was analyzed. As was expected, the temperature of the wake did not alter the strength or position of the shock waves. In addition, the thickness of the wake remained unchanged. Figure (4.6) is a contour plot of vorticity with the three cases overlayed for comparison. From this figure, the identical wake thickness for the three cases may be observed. In Figure (4.7), a plot of static temperature versus time is given at the boundary layer edge

location at the Gauge 2 position. From this figure you can see that the change in wake temperature does not change the temperature history seen by the gauge.

4.2 Version 2 - Coolant Injection

The second version of UNSFLO which was used allows for the addition of coolant mass into the mainstream flow. The user must specify the location on the nozzle guide vane where the coolant slot is located along with the width of the slot. In addition, the specification of the coolant velocity and enthalpy are required. The code then equally distributes the mass flux over the slot area specified.

For all of the following test cases, the coolant mass flux was set at 3 percent of the main flow mass flux in order to match the experimental results of the last chapter. Table (4.2) is a list of the input parameters used in the following cases The cooling slot was specified to be located on the pressure side of the nozzle guide vane between the 91 and 94 percent axial chord location, with the coolant gas exiting the slot at a 45 degree angle relative to the blade at the slot location. Figure (4.8) is a contour plot of Mach number, with the lines representing a Mach number of one. The location of the cooling slot has been highlighted in black. From this figure you can see that the coolant is being injected upstream of the nozzle throat. The coolant velocity was approximately 80 percent of the freestream velocity. This blowing ratio matches that from the blowdown turbine tests.

In order to verify that the new version of the code is correctly adding the coolant mass flux, a plot of passage length versus passage mass flow can be found in Figure (4.9). The passage mass flow plotted has been non-dimensionalized by inlet density and speed of sound. From this figure, the 3 percent jump in mass flux can be seen to

occur around the X=0.92 location. This location corresponds to the 92 percent axial chord location of the nozzle guide vane.

4.2.1 Coolant Injection Results

When the second version of UNSFLO was run with the injection parameters set as described above, a noticeable increase in rotor pressure side Nusselt number was observed. This increase in Nusselt number of around 10 percent can be seen in Figure (4.10) which is a plot of calculated averaged unsteady Nusselt number versus fractional wetted surface. In this figure the experimental results from the blowdown turbine facility were also included for comparison. On the pressure surface, the trends found in the computational results agree qualitatively with those of the experimental data. The injection and no injection Nusselt numbers are approximately the same over the first 10 percent of the pressure surface, with the difference between the injection and no injection Nusselt numbers growing to approximately 10 percent as you move towards the trailing edge of the blade. While the results obtained from UNSFLO follow the same trends as the experimental results, the computational results underpredict the fractional increase in Nusselt number on the pressure surface due to coolant injection by on the order of 25 percent at the second gauge location increasing to 60 percent at the last gauge location. Possible reasons for this underprediction will be discussed in more detail later in the chapter.

4.2.2 Influence of Coolant Slot Location

Because the coolant is being injected near the throat of the nozzle guide vanes, it is important to know the effect of varying coolant slot location on rotor Nusselt number. In particular, it may be important to know whether the coolant is being added upstream or downstream of the throat. This positioning upstream or downstream could

have a large influence on the position and shape of the NGV throat and trailing edge shock. To investigate the importance of slot positioning, the slot was moved downstream of the throat position for the no injection case to the 97 to 98 percent axial chord location. In Figure (4.11) a contour plot of Mach number is given with the old and new locations of the coolant slot highlighted in black. The contour plot of Mach number for the case of upstream injection is overlaid, so the effect of slot location on the nozzle throat can be seen. From this figure you can see that the downstream injection moves the location of the nozzle guide vane throat downstream when compared with the upstream injection case. The location of the NGV throat is moved aft of the coolant injection location, with the throat no longer coming in contact with the pressure side of the NGV. This means that the pressure side nozzle guide vane trailing edge shock is no longer needed to match the pressure at the trailing edge, and the shock no longer exists when the coolant slot is moved downstream. Figure (4.12) is a plot of calculated averaged unsteady Nusselt number versus fractional wetted surface for the upstream versus downstream slot location. From this figure you can see that the location of the downstream injection brings about a small increase in the Nusselt number of the rotor. To determine if this increase was due to the change in shock structure, or a change in the wake, the averaged unsteady vorticity is plotted versus circumferential distance at the X=1.17 position (See figure 4.3) for the upstream and downstream injection locations in Figure (4.13). From this figure you can see that the thickness of the wake, along with the maximum vorticity in the wake remains unchanged. This means that the changes in Nusselt number are due to the changes in the shock structure. In Figure (4.14), contour plots of pressure are given for the upstream and downstream injection locations at an instant in time. The upstream case is plotted in Figure (4.14a), and the downstream case plotted in Figure (4.14b). For both cases, the NGV trailing edge shocks are highlighted in black for clarity. From

these figures you can see that the suction side trailing edge shock remains approximately the same, with the large differences occurring on the pressure side. When the coolant is injected at the trailing edge of the NGV, the nozzle guide vane pressure side boundary layer is smaller than for the case of upstream injection. This thinner boundary layer due to downstream injection serves to decrease the blockage which drives up the axial mass flow through the machine. Figure (4.15) is a plot of axial mass flow versus passage length for the upstream and downstream injection locations. This figure shows the increase in passage mass flow with downstream injection. This increase in mass flow of approximately 1.5 percent for the downstream injection case may be responsible for the small increase in heat transfer to the rotor. The similarity of the suction side trailing edge shock explains why there is only a small change in the rotor Nusselt number. Because the suction side trailing edge shock impinges on the rotor suction surface, changes in the strength and location of this shock would bring about large changes in the rotor heat transfer. This is not true for the pressure side trailing edge shock however, since this shock does not directly impinge on the rotor surface, and the effects of the reflected shock are relatively small.

4.2.3 Effect of Coolant Exit Angle

Another parameter which may have an effect on the rotor Nusselt number is the angle of coolant injection. To investigate the importance of this effect, the coolant was injected at a 0 degree injection angle or tangent to the blade so that it could be compared with the case of 45 degree injection. Figure (4.16) is a plot of calculated averaged unsteady Nusselt number versus fractional wetted surface for the cases of 0 degree and 45 degree injection angles. This figure shows a negligible decrease in the pressure side Nusselt number when the angle is decreased from 45 degrees to 0 degrees. A possible explanation for the slight decrease in Nusselt number is the decrease in wake

thickness due to the tangent exit velocity. Figure (4.17) is a contour plot of vorticity for both the 0 and 45 degree cases. From this figure, the increased wake thickness due to increased injection angle can be seen. This area of increased wake thickness due to the larger injection angle is hatched in the figure As the injection angle increases, the coolant velocity normal to the blade increases, thereby causing a thickening of the wake. It was seen in Chapter 1 that the heat transfer to the pressure side of the rotor blade is proportional to the amount of time that the blade is exposed to the highly turbulent wake. This wake passing time increases as the thickness of the wake increases.

4.2.4 Effect of Increased Ratio of Specific Heats

When the cooled tests were performed in the blowdown turbine facility, the coolant gas which was used had a ratio of specific heats of 1.66. This means that the wake fluid had a higher ratio of specific heats than the surrounding fluid, as is the case in an engine. UNSFLO is not able to model this increase in the ratio of specific heats in the wake. This is due to the code's use of one ratio of specific heats throughout the calculations. In order to try and simulate the effect of increased ratio of specific heats, the mass averaged ratio of specific heats for both the coolant and main flows was used. The addition of the coolant raised the mass averaged ratio of specific heats from 1.28 to 1.29. Figure (4.18) is a plot of calculated averaged unsteady Nusselt number versus fractional wetted surface for the two ratios of specific heats. As would be expected, the small increase in the ratio of specific heats had a negligible effect on the Nusselt number.

4.2.5 Nusselt Number Time Histories

In section 4.2.1, it was shown that UNSFLO correctly predicted the increase in averaged unsteady rotor pressure side Nusselt number when coolant injection was added. In order to explain the reason for this increase, the UNSFLO calculated time histories of Nusselt number are plotted at the five gauge locations on the pressure surface in Figures (4.19a) through (4.19e) for two nozzle guide vane passings. For all of these figures both the calculated injection and no injection cases have been plotted. At all five gauge locations the injection case appears to be uniformly offset from the no injection case. The injection case appears to be shifted upward with respect to the no injection case. This offset agrees with the offset found in the experimental data of Chapter 2. Looking again at Figure (2.13d), you can see that the offset in Nusselt number is approximately 300 at the center of the wake passing. This offset is approximately the same as the UNSFLO calculated offset for the same gauge at the center of the wake passing which can be seen in Figure (4.19d).

To explain this offset, the calculated averaged unsteady heat flux (W/m^2) was plotted versus fractional wetted surface. This plot can be found in Figure (4.20). This figure shows that the actual heat transfer to the blade increases only a very small amount on the pressure side when coolant injection is added. One possible explanation for the offset is the use of an inappropriate non-dimensionalizing driving temperature difference when calculating the Nusselt numbers. For both the experimental results of Chapter 2, and the computational results so far, the driving temperature difference used in calculating the Nusselt numbers was the rotor relative inlet total temperature minus the blade temperature. For the case of coolant injection, the coolant temperature was mass averaged with the main flow temperature to find the rotor relative inlet total temperature. The rotor relative inlet total temperature was calculated to decrease by 2.1 percent when coolant injection was added.

In the flow, the actual driving temperature difference is not the rotor relative inlet total temperature minus blade temperature, but rather the local temperature at the boundary layer edge minus the blade temperature. In Figures (4.21a) through (4.21e) the averaged unsteady static temperature versus circumferential distance is plotted at the five gauge locations for one rotor blade passage. In each of these figures the location of the blade can be seen by the drop in temperature to the blade temperature. The blade suction and pressure sides are labeled in the figure. These figures show that while the temperature at the boundary layer edge on the suction surface is decreased due to coolant injection, the temperature at the edge of the boundary layer on the pressure surface remains unchanged. This means that on the pressure side of the blade, the actual driving temperature difference does not change with coolant injection.

This raises the question as to why the local temperature on the pressure side of the blade does not drop with coolant injection even though the rotor relative inlet total temperature drops with coolant injection. This question can be answered by looking at the path traveled by the coolant. Looking again at Figures (4.21a) through (4.21e) you can pinpoint the location of the coolant by noticing the sharp drop in temperature relative to the uncooled case at the point where the wake passes. The location of the coolant passing is near the suction surface for all of the gauge locations. This means that the coolant is migrating towards the suction surface. Work done by Roback and Dring [33] confirms this migration of the coolant from the pressure to the suction surface. Their experiments, performed in a turbine stage with nozzle guide vane trailing edge cooling, show that for injection velocities less than the freestream velocity, the coolant accumulates on the rotor suction surface. As the injection velocity decreases, accumulation of the coolant on the suction surface increases, until at some point the coolant does not reach the pressure surface. From Figures (4.21a) through (4.21e) it appears that this is the case.

4.2.6 Heat Transfer Time Histories

While the use of the inappropriate driving temperature difference in calculating the Nusselt number explains part of the Nusselt number difference between the injection and no injection cases, there is still approximately a 4 percent increase in the heat transfer on the pressure side of the blade when coolant injection is added. This means that coolant injection is causing an increase in the heat transfer coefficient on the pressure side of the blade. To help determine the cause of this increased heat transfer, plots of calculated heat transfer versus time at the five gauge locations on the pressure surface of the blade can be found in Figures (4.22a) through (4.22e) for two nozzle guide vane passings.

In order to better analyze what is causing the increased heat transfer on the pressure side of the blade when nozzle guide vane cooling is added, the calculated heat transfer to gauge 2 will be analyzed in depth. Figure (4.23) is the identical calculated heat transfer time history for gauge 2 found in Figure (4.22d). From this figure, you can see that the heat transfer increases due to coolant injection occur in the wake region, with the injection and no injection heat transfer being identical during the time when the gauge is not being influenced by the wake. In the figure, four different instants in time are labeled Time 1 through Time 4. Using the visualization code, the location of the wake region was determined. It was found that time 1 corresponds to a local heat flux maximum due to the portion of the wake generated by the nozzle guide vane suction side boundary layer. Time 2 corresponds to the portion of the wake generated by the nozzle guide vane pressure side boundary layer. Time 3 corresponds to an instant in time right before the wake has completely passed. At time 4, the wake has passed and the heat transfer to the rotor is no longer being influenced by the wake.

From Figure (4.23) it appears that there are two phenomena which are increasing the heat transfer when injection is added. The first of these phenomena is a thickening of the wake. Figure (4.24) is a contour plot of vorticity at the trailing edge of a nozzle guide vane with the injection case overlaid on top of the no injection case. The hatched region is the thickening of the boundary layer and wake due to the coolant injection. Referring again to Figure (4.23), it can be seen that for the case of nozzle guide vane cooling the increased levels of heat transfer due to the wake occur for a longer fraction of a vane passing period. This longer period of increased heat transfer due to the thicker wake is one of the reasons for the higher averaged unsteady heat transfer to the rotor when coolant injection is added. It can also be seen that levels of heat transfer for that portion of the wake caused by the nozzle guide vane suction side boundary layer remain the same when injection is added as would be expected, since the coolant is not being added to the NGV suction side boundary layer. The portion of the wake region which thickens when coolant injection is added is due to a thickening of the pressure side boundary layer. This thickening of the boundary layer on the pressure side of the nozzle is due to the coolant being added into the boundary layer.

The second phenomena which increases the heat transfer to the blade when injection is added, is an increased level of heat transfer for the injection case in that portion of the wake caused by the nozzle pressure side boundary layer. The passing of that portion of the wake created by the NGV pressure side boundary layer occurs around Time 2, which shows an increase in heat transfer of approximately 6 percent when coolant injection is added. In order to determine the reason for this increased heat transfer, the boundary layer profiles for the injection and no injection cases will be compared in the next section for Time 1 through Time 4.

4.2.7 Boundary Layer Profiles

When calculating the heat transfer to the blade, UNSFLO uses the following heat conduction formula:

$$\dot{q} = k\frac{(T_2 - T_1)}{(y_2 - y_1)} \tag{4.2.1}$$

where location 2 is at the first grid point off the blade, and location 1 is at the surface of the blade. In a turbulent boundary layer such as the one specified by UNSFLO on the pressure side of the rotor, the thermal conductivity, k, is determined from the turbulent Prandtl number set by the user, and the turbulent viscosity calculated by UNSFLO. The equation is as follows:

$$\frac{k}{C_p} = \frac{\mu}{Pr} + \frac{\mu_t}{Pr_t} \tag{4.2.2}$$

This equation illustrates the relationship between the thermal conductivity and the turbulent viscosity. As the turbulent viscosity rises, so does the heat transfer to the blade. The turbulence model which is being used by UNSFLO is due to Cebeci and Smith [34]. In this model, the Prandtl-Van Driest formulation is used in the inner region of the boundary layer, and is as follows:

$$(\mu_t)_{inner} = \rho l^2 |\omega| \tag{4.2.3}$$

where l is the Prandtl mixing length with the Van Driest exponential damping term and ω is the magnitude of the vorticity. To avoid the need for small grid spacing at the wall, Spaulding's law-of-the-wall formula [8] has been used to calculate the turbulent viscosity and shear stress at the wall. This turbulent viscosity at the wall is calculated using the velocity at the first point off the wall which is calculated using the turbulent viscosity from Equation (4.2.3). It is the value of turbulent viscosity at the wall which is used in determining the heat transfer to the blade.

Looking again at Equations (4.2.1) and (4.2.2), you can see the heat transfer to the blade depends on the level of turbulent viscosity at the blade surface, and the slope of the temperature between the blade and the first grid point off the blade. Figure (4.25) is a boundary layer profile plot of turbulent viscosity versus distance from the blade surface to the first grid point off the wall for the four instants in time (Time=1 through 4) shown in Figure (4.23) for the injection and no injection cases. In Figure (4.25) you can see that for the three cases inside the boundary layer (Time=1,2, and 3) the turbulent viscosity at the wall has increased due to coolant injection, while for the case outside the boundary layer (Time=4) the wall turbulent viscosity is identical. In addition, for the cases near the center of the wake (Time=1 and 2) the turbulent viscosity at the wall is highest, with the lowest wall turbulent viscosity occurring for the case outside the wake (Time=4). These trends in turbulent viscosity at the wall agree with the trends in heat transfer in Figure (4.23). The largest increase in turbulent viscosity at the wall when coolant injection is added occurs at Time=2, which corresponds to the point of largest heat transfer increase due to injection in Figure (4.23).

Looking again at Equation (4.2.3), it can be seen that the turbulent viscosity (i.e. the heat transfer) is proportional to the vorticity in the boundary layer. It has just been shown that when injection is added, the turbulent viscosity at the wall increases during the passing of the wake. It follows then that the increase in turbulent viscosity (heat transfer) when injection is added, is due to increases in vorticity in the boundary layer. In Figure (4.26) the boundary layer profile is plotted for vorticity versus distance from the blade surface to the first grid point off the wall for the four instants in time (Time=1 through 4) shown in Figure (4.23) for the injection and no injection cases. As would be expected, Figure (4.26) agrees with the results of Figure (4.25). Inside the wake (Time=1,2, and 3), coolant injection causes an increase in vorticity near the wall, with

no increase occurring at the point outside the wake (Time=4). The highest levels of vorticity occur for the two points (Time=1 and 2) near the center of the wake. Once again, Time=2 shows the largest increase due to coolant injection.

We have just seen that the vorticity in the rotor blade boundary layer increases due to coolant injection only during the wake passing. This indicates that the reason for the increased heat transfer to the blade is due to increased vorticity inside the wake. Figure (4.27) is a plot of averaged unsteady vorticity versus circumferential distance at the junction of the stator and rotor grids (X=1.17). This figure shows a noticeable increase in the maximum vorticity of the wake when injection is added, especially in that region of the wake caused by the nozzle guide vane pressure side boundary layer. In this region, the injection brings about a 33 percent increase in the maximum vorticity of the wake. The thickening of the boundary layer on the pressure side due to coolant injection is greatly increasing the vorticity in the wake.

To better see the increase in size and vorticity of the wake, contour plots of vorticity are plotted in Figures (4.28) through (4.31) for the injection and no injection cases at the four times Time=1 through Time=4. Due to the complexity and inevitable confusion which would be caused by overlaying the injection and no injection cases, the no injection case contour plots can be found in (a), with the injection case contour plots located in (b). In each of these contour plots, the areas of moderate vorticity are hatched while the areas of high vorticity are cross hatched. In addition, the location of Gauge 2 is marked on each plot. A blowup of the Gauge 2 location is also given for each plot, with the vorticity contours highlighted in black, and the unsteady velocity vectors (Total-Mean) plotted so that the increased vorticity of the wake can be seen interacting with the boundary layer. At Time=1, you can see that the wake caused by the vane suction side boundary layer is interacting with the rotor boundary layer at the Gauge 2 location. Comparing Figures (4.28a) and (4.28b) shows that this portion of the

wake remains approximately the same size, with the region of high vorticity slightly increased. At Time=2 (Figures 4.29a) and (4.29b), you can see the wake caused by the vane pressure side boundary layer interacting with the rotor boundary layer at the Gauge 2 position. This portion of the wake however is noticeably larger for the injection case, in addition to a large increase in the region of high vorticity for the injection case. At Time=3 (Figures 4.30a) and (4.30b), notice that the wake has almost passed at the Gauge 2 location for the no injection case. For the injection case however, the trailing edge of the wake is still interacting with the rotor boundary layer at the Gauge 2 location. This is due to the increased thickness of the wake. Also notice the larger unsteady velocity vectors interacting with the boundary layer at the Gauge 2 location for the injection case. At Time=4 (Figures 4.31a) and (4.31b), the wake is no longer interacting with the rotor boundary layer at the Gauge 2 location. It is interesting to note that in each of the last four figures, the wake with coolant injection has been displaced towards the suction surface. This confirms the concept of coolant migration towards the suction surface.

Equation (4.2.1) shows that the heat transfer is not only dependent on the thermal conductivity, but on the temperature gradient near the wall as well. Figure (4.32) is a boundary layer profile plot of temperature versus distance from the blade surface to the first grid point off the wall for the four instants in time (Time=1 through 4) shown in Figure (4.23) for the injection and no injection cases. For the two points near the center of the wake (Time=1 and 2), there is a small decrease in the temperature gradient near the wall for Time=1 and a small increase for Time=2 when injection is added. At Time=1, this small decrease in temperature gradient cancels the small increase in turbulent viscosity at the wall due to coolant injection. This means the heat transfer at Time=1 remains approximately the same when injection is added. This is what is seen in Figure (4.23). At Time=2, the large increase in turbulent viscosity at the

wall in addition to the small increase in temperature gradient when cooling is added, brings about a large increase in the heat transfer. At Time=3, there is a large increase in the temperature gradient near the wall when injection is added. The author is currently unsure of the reason for this, though one possible explanation is the migration of the coolant from the pressure to the suction side of the rotor. This large increase in temperature gradient coupled with a moderate increase in turbulent viscosity at the wall causes the heat transfer to rise with injection. This increase in heat transfer due to injection at Time=3 is approximately 12 percent. 6 percent of this increase is due to the increased temperature gradient while the other 6 percent is due to the increased turbulent viscosity. At Time=4, the temperature gradient remains unchanged with coolant injection as would be expected.

4.2.8 Heat Transfer Comparisons

It has been shown that the rise in Nusselt number on the pressure side of the rotor is due both to an inappropriate choice of driving temperature, and an increase in wake thickness and maximum vorticity. Figure (4.33) is a plot of averaged unsteady heat transfer versus fractional wetted surface with and without coolant injection for both the computed and experimental data. The experimental data has much lower levels of heat transfer when compared to the calculated levels of heat transfer, due to the setting of the rotor blade temperature to the design blade temperature in UNSFLO instead of matching it with the blade temperature measured in the experimental data. This design blade temperature is about 15 percent lower than the experimental blade temperature. From this figure you can see that UNSFLO greatly underpredicts the increase in heat transfer due to coolant injection on the pressure surface. To get a better feel for this underprediction, the areas under the heat transfer curves have been integrated and divided by the rotor relative inlet stagnation enthalpy. This gives a

measure of the amount of heat transfer to the blade with respect to the energy of the incoming flow. For the experimental results, it was found that the above quantity increased by 15.5 percent when injection was added. This increase was only 3.5 percent for the calculated results. One possible reason for this underprediction of heat transfer increase due to coolant injection is the setting of the blade temperature in UNSFLO to design conditions. This means the blade temperature for the injection and no injection cases is the same. In the experimental data, the blade temperature for the injection case was 3 percent lower than the no injection case. This lower temperature increased the driving temperature difference for the injection case. To check this hypothesis , the rotor blade temperatures in UNSFLO were set to match the experimental conditions. Figure (4.34) is a plot of averaged unsteady heat transfer versus fractional wetted surface for the injection and no injection cases with these new blade temperatures. This figure shows that UNSFLO does a much better job of predicting rotor pressure side heat transfer when the rotor blade temperatures are matched with the experimental data, though the code greatly underpredicts the heat transfer to the suction side of the blade with the largest differences between the injection and no injection cases occurring over the first 20 percent of the suction surface. On the pressure side, the fractional increase in heat transfer becomes larger as you move towards the trailing edge of the blade. This agrees with the experimental data, but was not predicted when the rotor blade temperatures in UNSFLO were set at design conditions. In this case, the ratio mentioned above increases 21 percent when injection is added, as compared to 15.5 percent for the experimental data. It should be noted however that a significant portion of this increase occurs at the leading edge and first 20 percent of the suction surface.

4.2.9 Code Shortcomings

While this version of UNSFLO was correctly able to qualitatively predict the increase in pressure side rotor heat transfer due to nozzle guide vane trailing edge cooling, it underpredicted the magnitude of this increase. One possible reason for this underprediction is the inability of the code to take into account the different ratio of specific heats of the coolant and the main gas. The different ratio of specific heats of the wake could have an effect on rotor heat transfer, though the author feels that this effect is negligible.

The incorrect hade specification is also another possible reason for this underprediction. Figure (3.2) showed that varying the hade causes the pressure side heat transfer to vary. The mass addition to the flow in the case of coolant injection will change the correct hade to be used. In all of the work done in this paper the hade was kept constant for both the injection and no injection cases. While the hade models the changes in streamtube height in the third dimension, it does not model other three dimensional effects such as rotor tip flows, or the migration of coolant gases in the third dimension.

Another possible reason for the underprediction of heat transfer increase due to coolant injection is the inability of UNSFLO to model the freestream turbulence within the wake. UNSFLO is not able to take into account the increase in rotor heat transfer due to the increased freestream turbulence in the wake caused by the coolant injection. The increase in turbulent viscosity in the rotor boundary layer due to coolant injection is underpredicted due to the lack of increased mixing caused by the increase in wake freestream turbulence with coolant injection.

Chapter 5
Conclusions

The experimental data of Abhari [19] presented in Chapter 2 showed that when nozzle guide vane cooling was implemented in the MIT blowdown turbine facility, the Nusselt numbers on the rotor increased on the aft 90 percent of the pressure surface. This paper used the numerical code UNSFLO to determine the cause of this increased Nusselt number. The following results were found.

1) It is the coolant mass addition and resulting thickening of the pressure side nozzle guide vane boundary layer that is responsible for the increased heat transfer to the rotor, not the decreased temperature of the wake due to the coolant.

2) The coolant slot location on the pressure surface has only a small effect on the Nusselt number of the rotor. Moving the slot downstream serves to move the location of the NGV choked point downstream as well, so that the choked point remains downstream of the injection location. When the slot is moved far enough downstream, the choked region no longer comes in contact with the NGV pressure surface, and the pressure side trailing edge shock is no longer needed to equalize the pressure at the nozzle guide vane trailing edge. As the injection point moves downstream, the nozzle guide vane pressure side boundary becomes thinner thereby decreasing the flow

blockage due to the injection. This decrease in flow blockage increases the mass flow through the stage causing an increase in rotor pressure side heat transfer.

3) Simulating the increased ratio of specific heats of the coolant by mass averaging the coolant and main flow ratio of specific heats, did not have a noticeable effect on the rotor pressure side Nusselt number.

4) The injection angle of the coolant had a small effect on the rotor pressure side heat transfer. As the angle was increased, the heat transfer to the pressure side of the rotor increased. This was due to a thickening of the wake as the injection angle was increased.

5) A portion of the increase in Nusselt number when injection is added, is due to the use of an inappropriate driving temperature when calculating the Nusselt number. The local boundary layer edge minus blade temperature is the appropriate driving temperature instead of total rotor relative inlet minus blade temperature, however the boundary layer edge temperature is usually not known for experimental data. This leaves the problem of finding a more appropriate way of presenting the convective heat transfer coefficient. Using the total rotor relative inlet temperature is inappropriate due to the migration of the coolant towards the suction surface of the rotor.

6) The increase in heat transfer to the pressure side of the rotor is due to an increase in wake thickness, along with increased vorticity in the wake. This increase in wake thickness and maximum vorticity is due to the coolant injection on the pressure side of the nozzle guide vane, which thickens the boundary layer when injected.

7) It was found that the large underprediction of heat transfer increase on the rotor pressure surface by UNSFLO when injection was added, was due to the incorrect specification of the rotor blade temperatures. When the rotor blade temperatures in UNSFLO were matched with the experimental blade temperatures the code did a much better job of predicting the heat transfer increase due to coolant injection

5.1 Recommendations for Future Work

It was seen in Chapter 3 that hade has a large effect on the calculated heat transfer to the blade. When coolant injection is added, the correct hade specification should change, however this was not included in the calculations in this paper. The hade for injection should be determined and tried in the code.

While UNSFLO is able to qualitatively predict the heat transfer increase to the pressure side of the rotor when coolant injection is added, it underpredicts this increase. This is due to a few shortcomings in the code. To correct these shortcomings the following changes should be made to the code.

1) The current algebraic turbulence model is unable to predict transition and take into account any history effects. A more sophisticated turbulence model increase the accuracy of the code.

2) The increased freestream turbulence in the wake due to coolant injection is not modeled. It is believed that the underprediction in pressure side heat transfer increase due to injection is caused by this lack of freestream turbulence in the wake. Finding a way to model the effect of freestream turbulence would solve this problem.

3) In the last chapter we saw that matching the experimental rotor blade temperatures in the UNSFLO calculations brought about a large change in the heat transfer to the rotor. It would make sense to look at the time histories of heat transfer in order to make sure the causes of increased heat transfer due to coolant injection agree with those presented in this paper.

References

1. Oates, G.C., Aerothermodynamics of Gas Turbine and Rocket Propulsion, AIAA, 1988

2. Kerrebrock, J.L., Aircraft Engines and Gas Turbines, MIT Press, 1977

3. Wilson, D.G., The Design of High-Efficiency Turbomachinery and Gas Turbines, MIT Press, 1984

4. Potter, M.C., and Foss, J.F., Fluid Mechanics, Great Lakes Press, Inc., 1982

5. Schlichting, H., Boundary-Layer Theory, 7th Edition, McGraw-Hill Publishing Company, 1987

6. Schafer, H.J., Koch, B. and Pfeifer, H.J., Application of LDV Techniques to High Speed Combustion Flow, ICIASF, pp31-39, 1977

7. Landahl, M.T., and Mollo-Christensen, E., Turbulence and Random Processes in Fluid Mechanics, Cambridge University Press, 1986

8. White, F.M., Viscous Fluid Flow, McGraw-Hill Publishing Company, 1974

9. LaGraff, J.E., Ashworth, D.A., Schultz, D.L., Measurement and Modeling of the Gas Turbine Blade Transition Process as Disturbed by Wakes, ASME 88-GT-232, 1988

10. Wittig, S., Schulz, A., Bauer, H.J., Sill, K.H., Effects of Wakes on the Heat Transfer in Gas Turbine Cascades, AGARD-CP-390, May 1985

11. Kemp, N.H., and Sears, W.R., Aerodynamic Interference Between Moving Blade Rows, Journal of the Aeronautical Sciences, Vol. 20, No.9, September 1953, pp. 585-597

12. Kerrebrock, J.L., and Mikolajczak, A.A., Intra Stator Transport of Rotor Wakes and Its Effect on Compressor Performance, ASME Journal of Engineering for Power, 1970, pp 359-370

13. Binder, A., Forster, W., Kruse, H., Rogge, H., An Experimental Investigation Into the Effect of Wakes on the Unsteady Turbine Rotor Flow, ASME 84-GT-178, 1984

14. Lefcourt, M.D., An Investigation Into Unsteady Blade Forces in Turbomachines, ASME Journal of Engineering For Power, October 1965, pp. 345-354

15. Hodson, H.P., Measurements of Wake-Generated Unsteadiness in the Rotor Passages of Axial Flow Turbines, ASME 84-GT-189, 1984

16. Doorly, D.J., and Oldfield, M.L.G., Simulation of the Effects of Shock Wave Passing on a Turbine Rotor Blade, ASME 85-GT-112, 1985

17. Ashworth, D.A., LaGraff, J.E., Schultz, D.L., Unsteady Interaction Effects on a Transitional Turbine Blade Boundary Layer, ASME Journal of Turbomachinery, April 1989

18. Ashworth, D.A., LaGraff, J.E., Schultz, D.L., Grinrod, K.J., Unsteady Aerodynamic and Heat Transfer Processes in a Transonic Turbine Stage, ASME 85-GT-128, 1985

19. Abhari, R.S., An Experimental Study of the Unsteady Heat Transfer Process in a Film Cooled Fully Scaled Transonic Turbine Stage, PhD Thesis, 1991

20. Abhari, R.S., Guenette, G.R., Epstein, A.H., Giles, M.B., Comparison of Time-Resolved Turbine Rotor Blade Heat Transfer Measurements and Numerical Calculations, ASME, 1991

21. Johnson, A.B., Rigby, M.J., Oldfield, M.L.G., Ainsworth, R.W., Surface Heat Transfer Fluctuations on a Turbine Rotor Blade Due to Upstream Shock Wave Passing, ASME 88-GT-172, 1988

22. Dunn, M.G., Heat Flux Measurements for the Rotor of a Full-Stage Turbine: Part 1 - Time-Averaged Results, ASME 86-GT-77, 1986

23. Epstein, A.H., Guenette, G.R., Norton, R.J.G., The Design of the MIT Blowdown Turbine Facility, MIT, Gas Turbine Lab Report #183, April 1985

24. Guenette, G.R., A Fully Scaled Short Duration Turbine Experiment, PhD Thesis, 1985

25. Ashworth, D.A., Unsteady Aerodynamics and Heat Transfer Processes in a Transonic Turbine Stage, D.Phil Thesis, 1987

26. Goldstein, R.J., Eckert, E.R.G., Burggraf, F., Effect of Hole Geometry and Density on Three-Dimensional Film Cooling, International Journal of Heat and Mass Transfer, Vol 17, pp 595-607, 1974

27. Epstein, A.H., Guenette, G.R., Norton, R.J.G., Yuzhang, C., High Frequency Response Heat Flux Gauge, Review of Scientific Instrumentation, Vol 57, No.4, 1986, pp 639-649

28. Giles, M.B., UNSFLO : A Numerical Method For Unsteady Inviscid Flow In Turbomachinery, Technical Report 195, MIT Gas Turbine Laboratory, 1988

29. Ni, R.H., A Multiple Grid Scheme for Solving the Euler Equations, AIAA Journal, Vol 20, No.11, 1981, pp 1565-1571

30. Baldwin, B.S., Lomax, H., Thin Layer Approximation and Algebraic Model for Separated Turbulent Flows, AIAA 78-257, 1978

31. GRAFIC, Massachusetts Institute of Technology

32. Haimes, Robert, Visual 2, Massachusetts Institute of Technology

33. Roback, R.J., Dring, R.P., Hot Streaks and Phantom Cooling in a Turbine Rotor Passage Part 1 - Separate Effects, ASME 92-GT-75, 1992

34. Cebeci, T., Smith, A.M.O., Analysis of Turbulent Boundary Layers, Academic Press, 1974

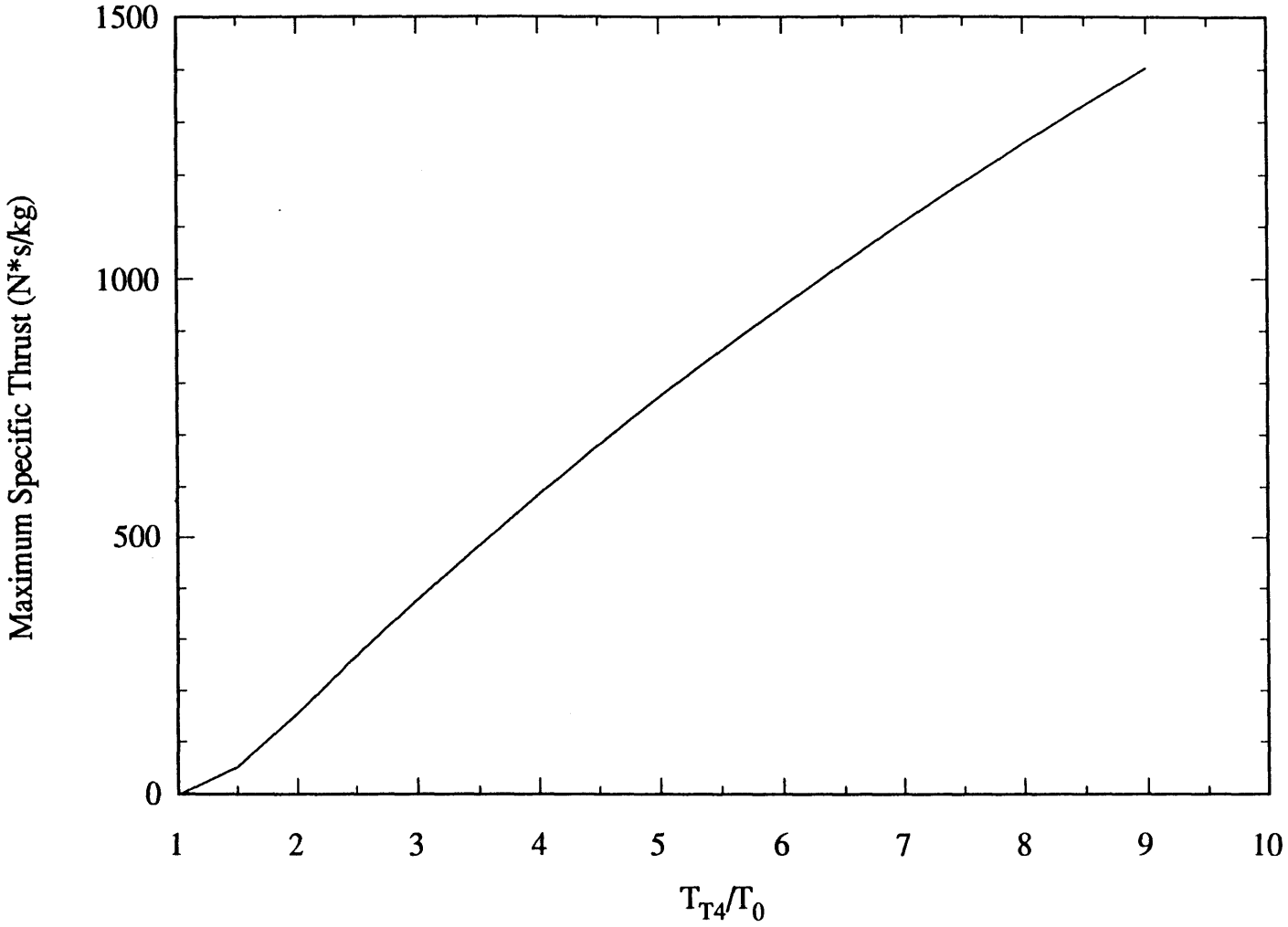

Figure (1.1) : Effect of Turbine Inlet Temperature on Maximum Specific Thrust for a Typical Gas Turbine Engine

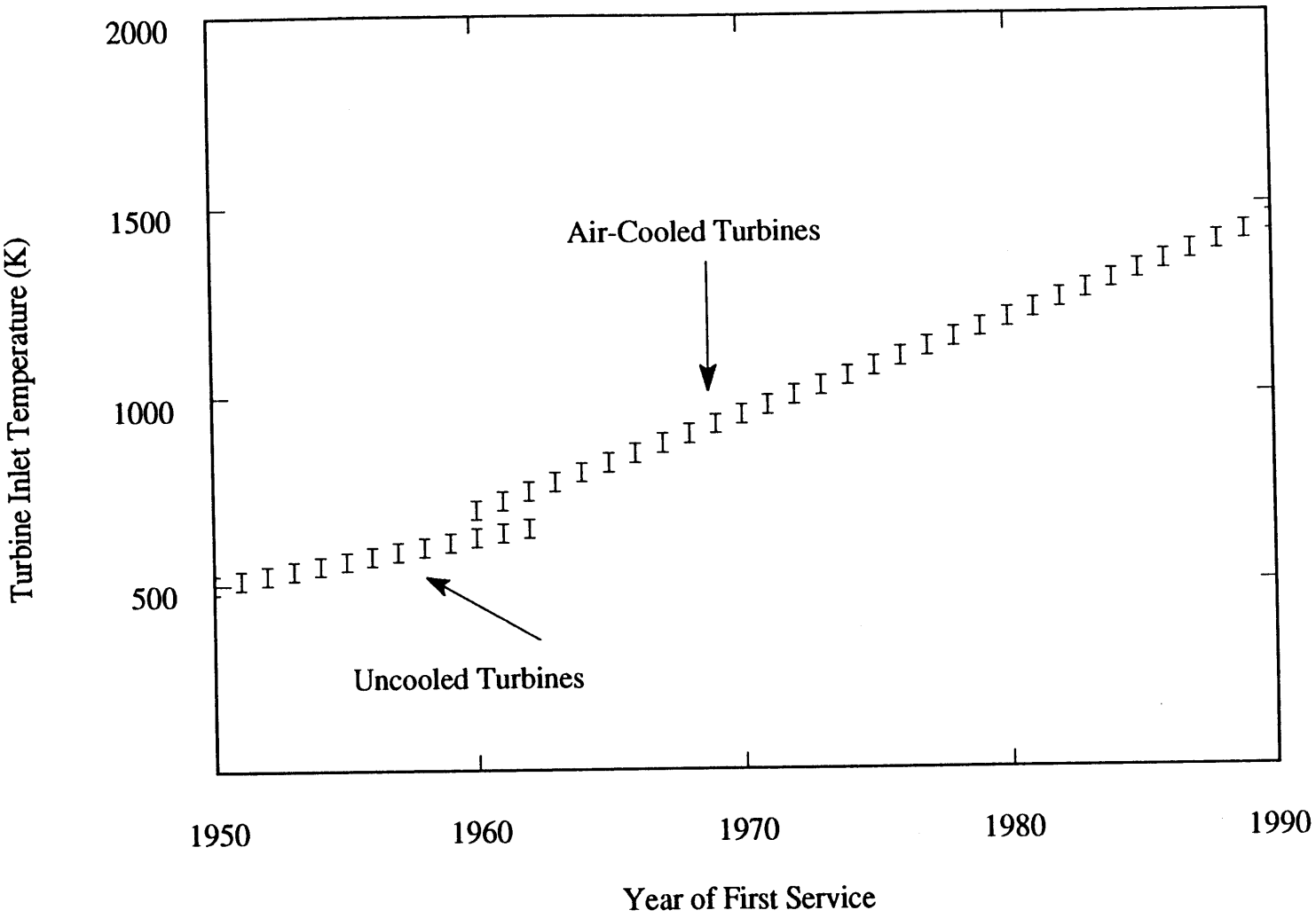

Figure (1.2) : Trends in Maximum Turbine Inlet Temperature with Time [2]

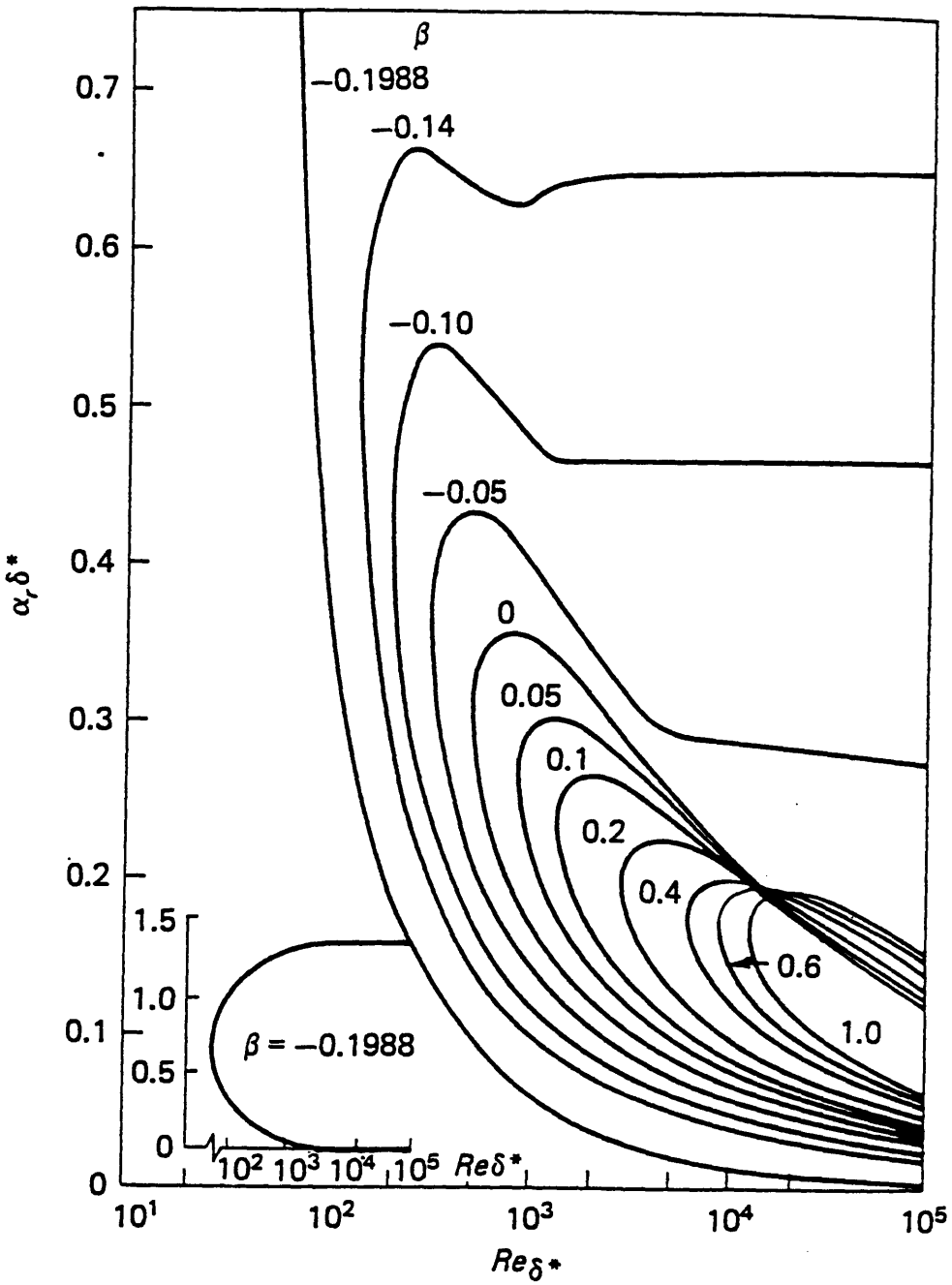

Figure (1.3) : Orr-Sommerfeld Equation Neutral-Stability Curves for the Falkner-Skan Boundary Layer [8]

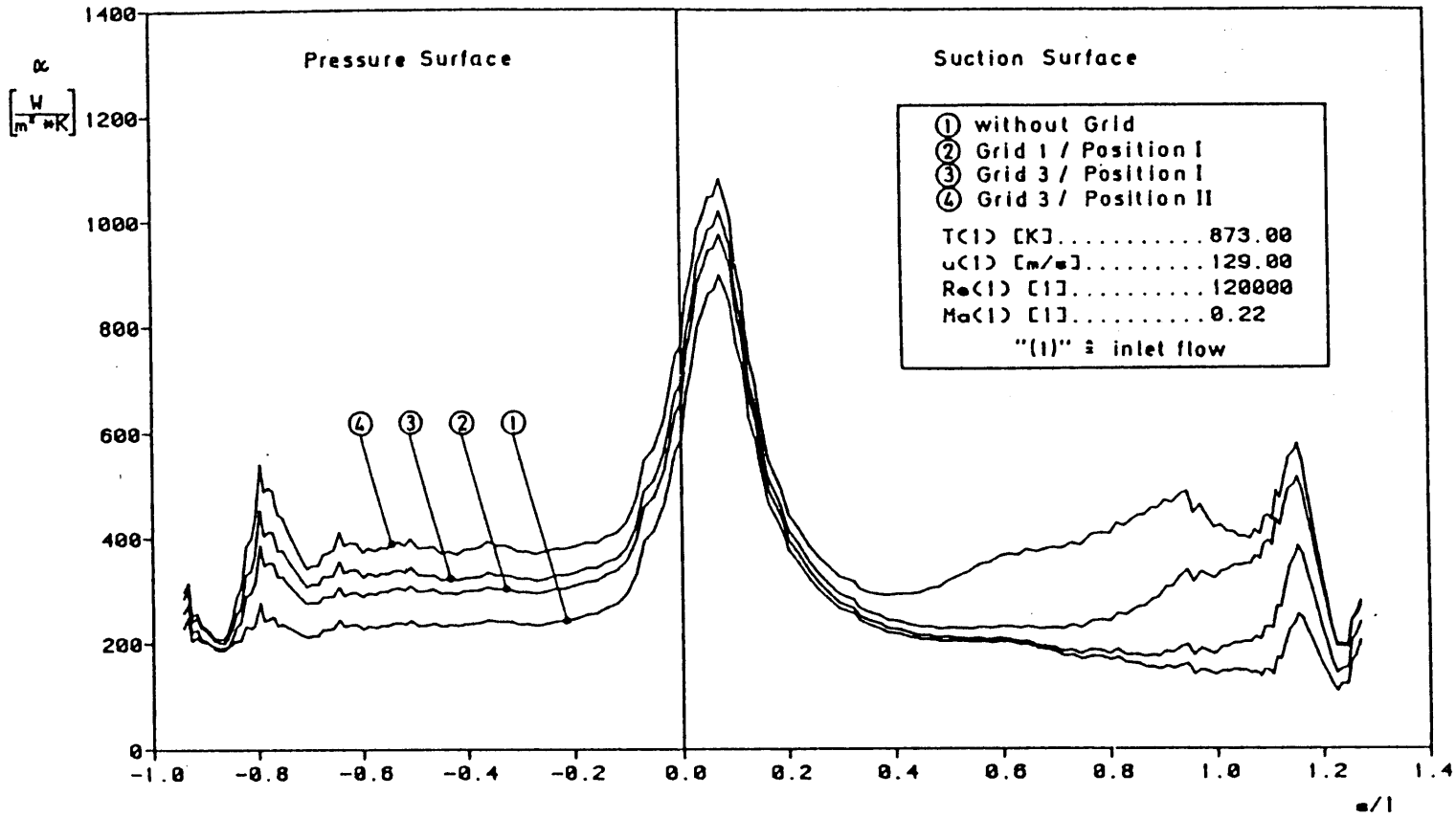

Figure (1.4) : Effect of Freestream Turbulence on Rotor Heat Transfer Coefficient [10]
Tu = 1.4%, 4.8%, 7.6% and 14.0%

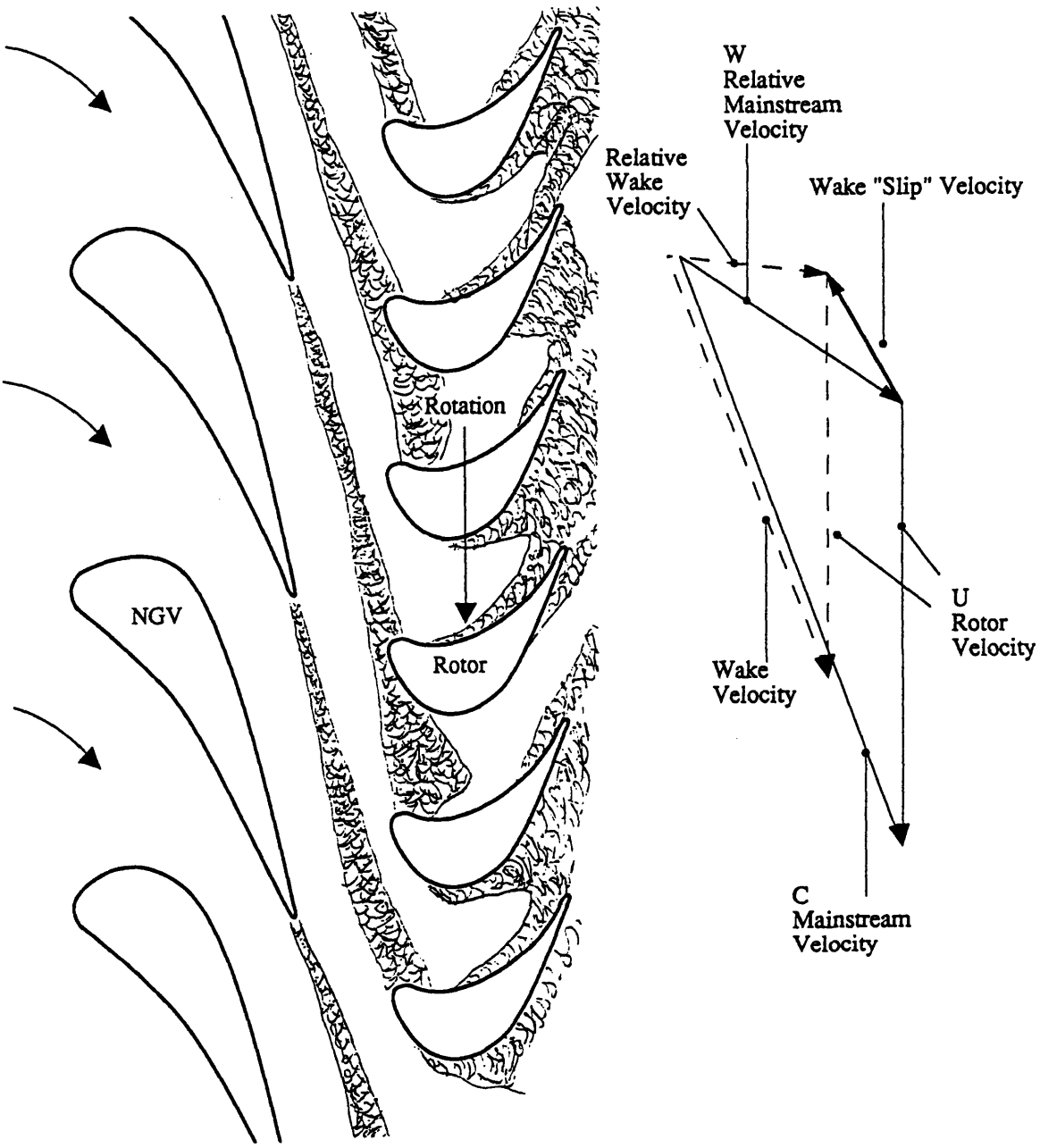

Figure (1.5) : Cutting of Nozzle Wakes and the Associated Slip Velocity

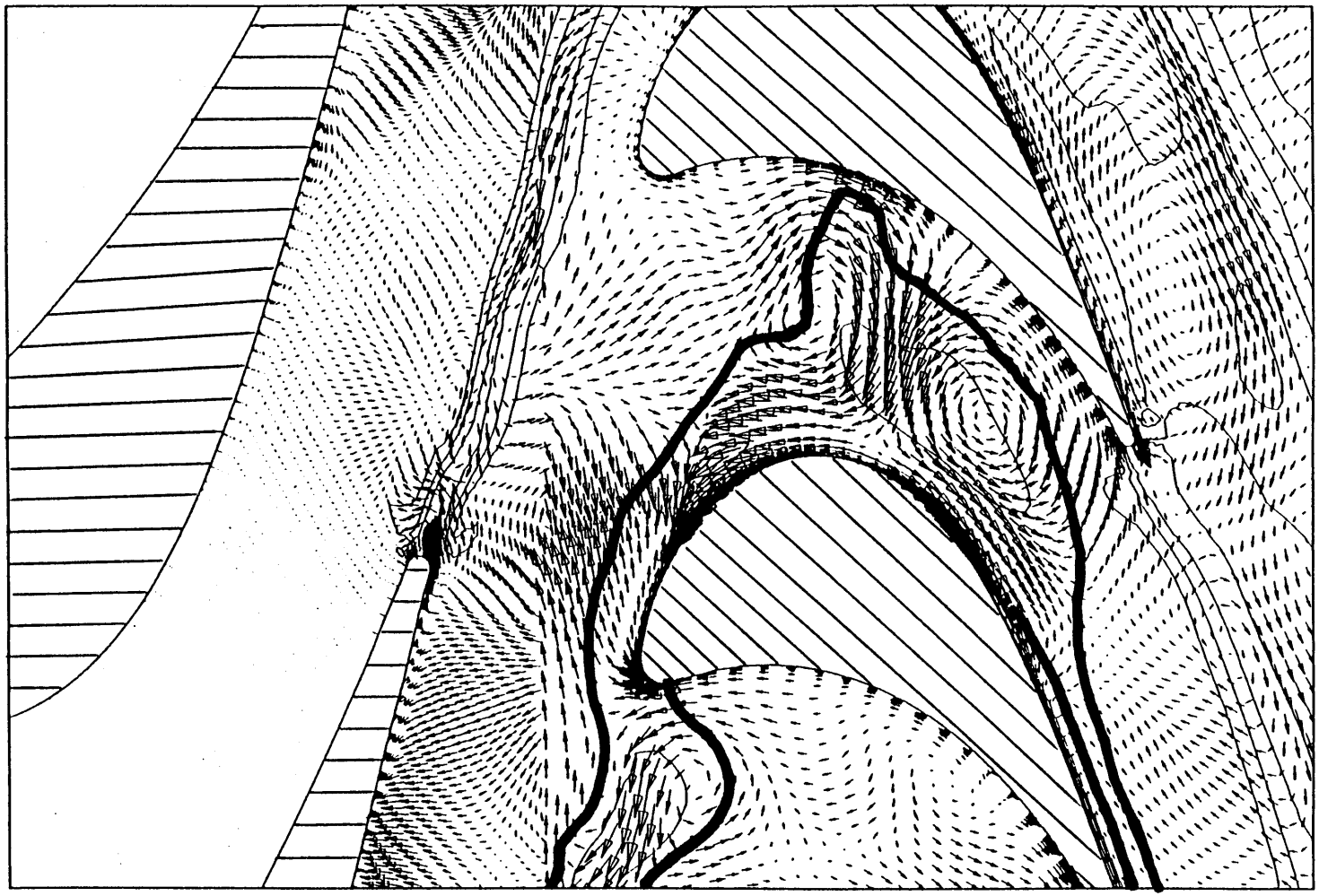

Figure (1.6) : Unsteady Velocity Vectors (Absolute Total-Relative Mean) Showing Circulation Pattern Due to Wake Slip Velocity

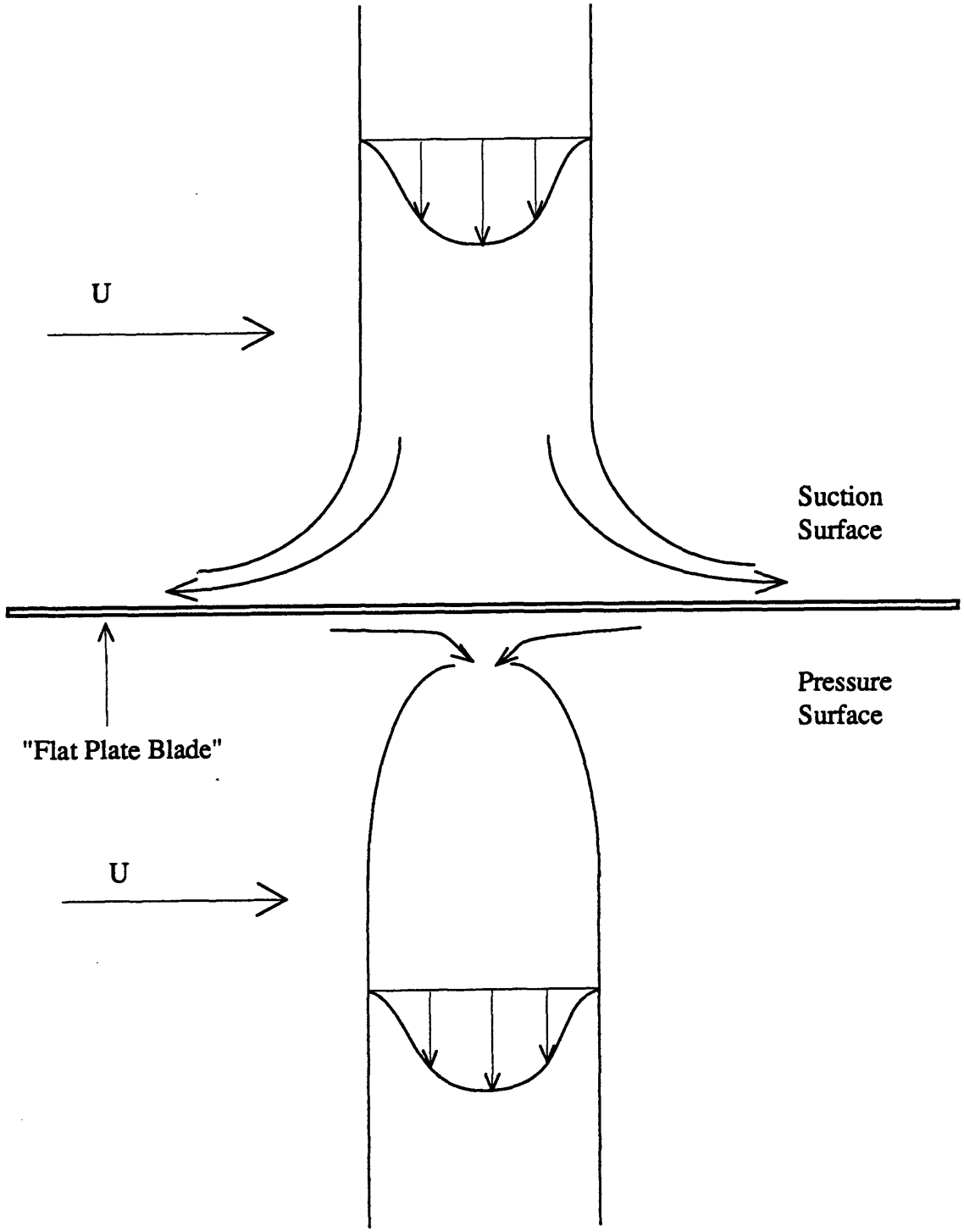

Figure (1.7) : Use of "Negative Jet" to Model NGV Wakes

Time = 0.2

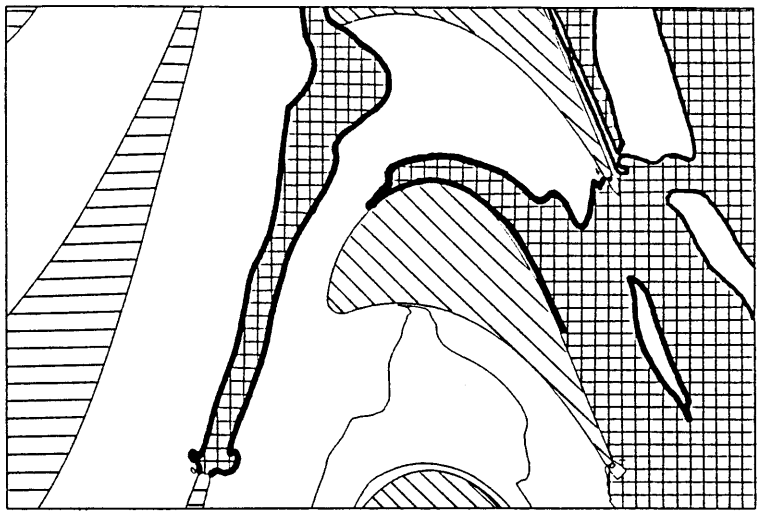

Time = 0.4

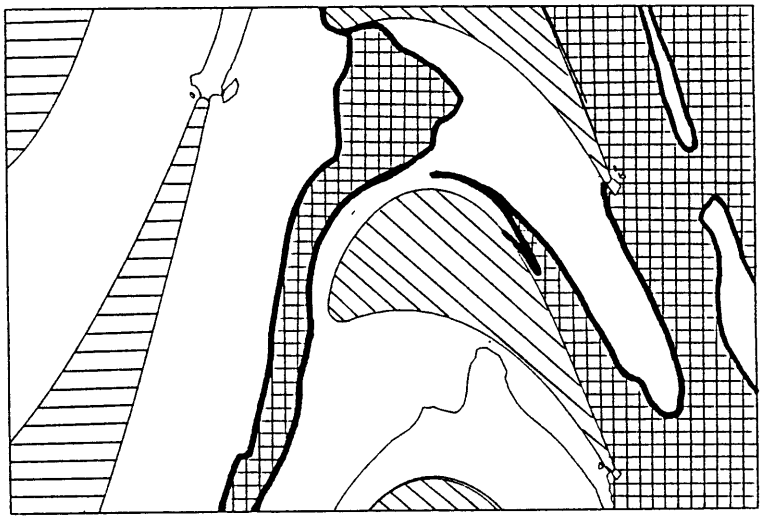

Time = 0.6

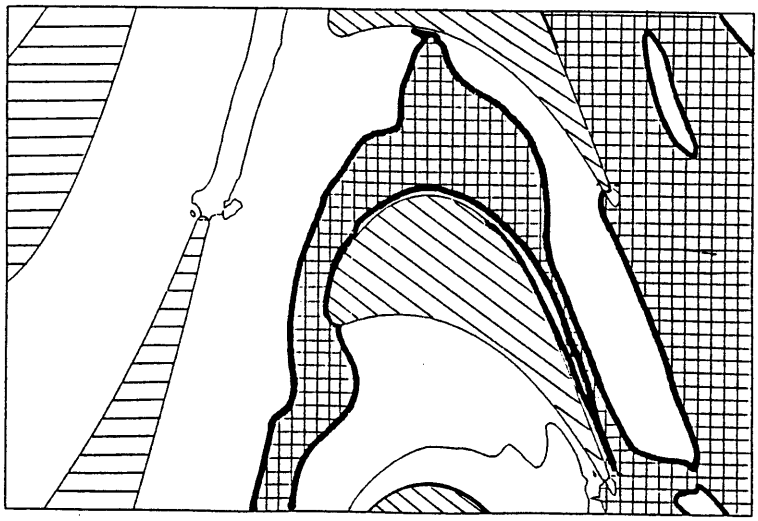

Figure (1.8) : Wake / Rotor Interaction for Five Time Periods

Time = 0.8

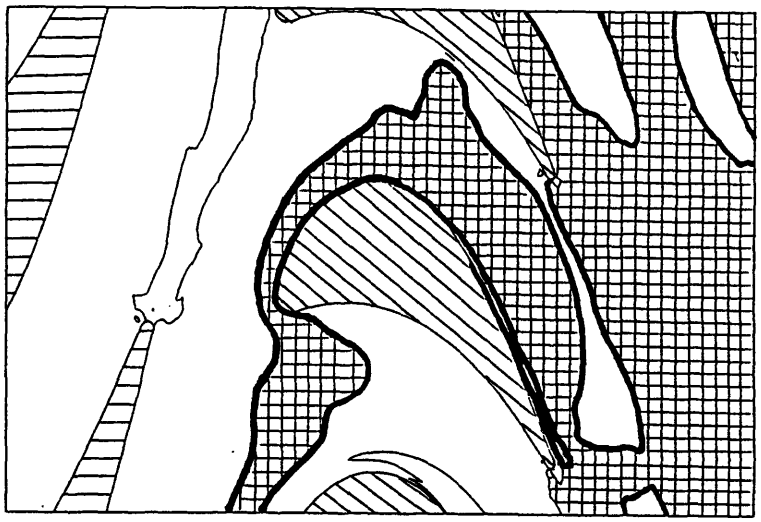

Time = 1.0

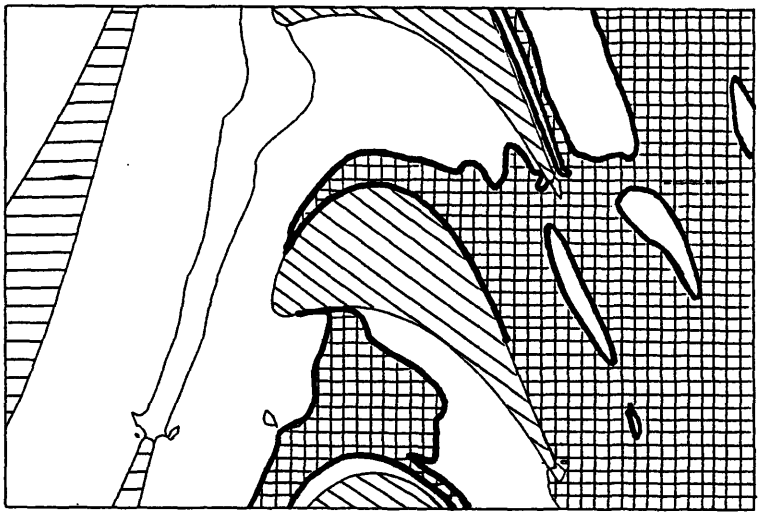

Figure (1.8) : Continued; Wake / Rotor Interaction for Five Time Periods

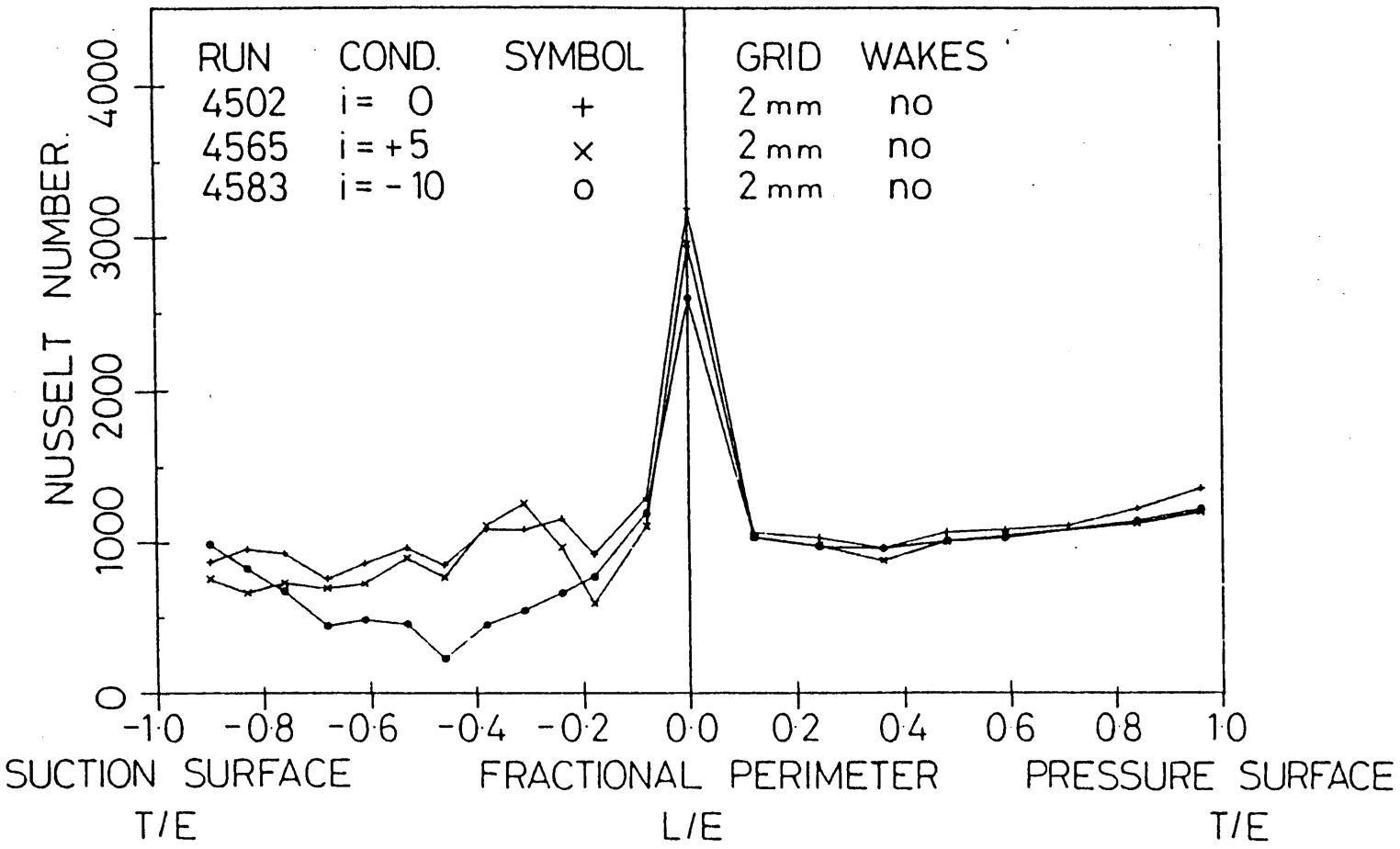

Figure (1.9) : Effect of Rotor Incidence on Steady State Nusselt Number in a Cascade [18]

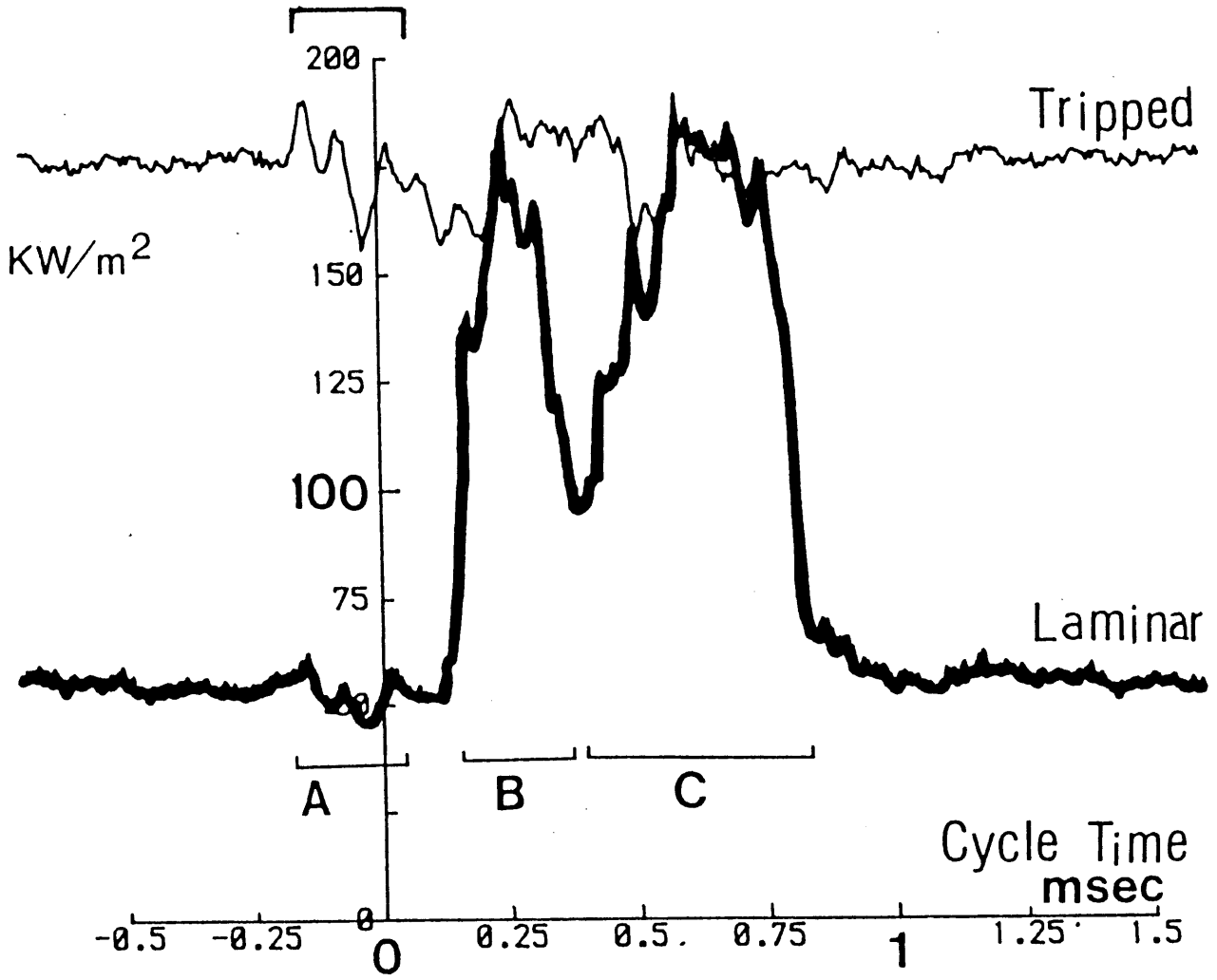

Figure (1.10) : Heat Transfer Time History for a Point at 25 Percent Wetted Surface on Rotor Suction Surface in a Cascade [16]

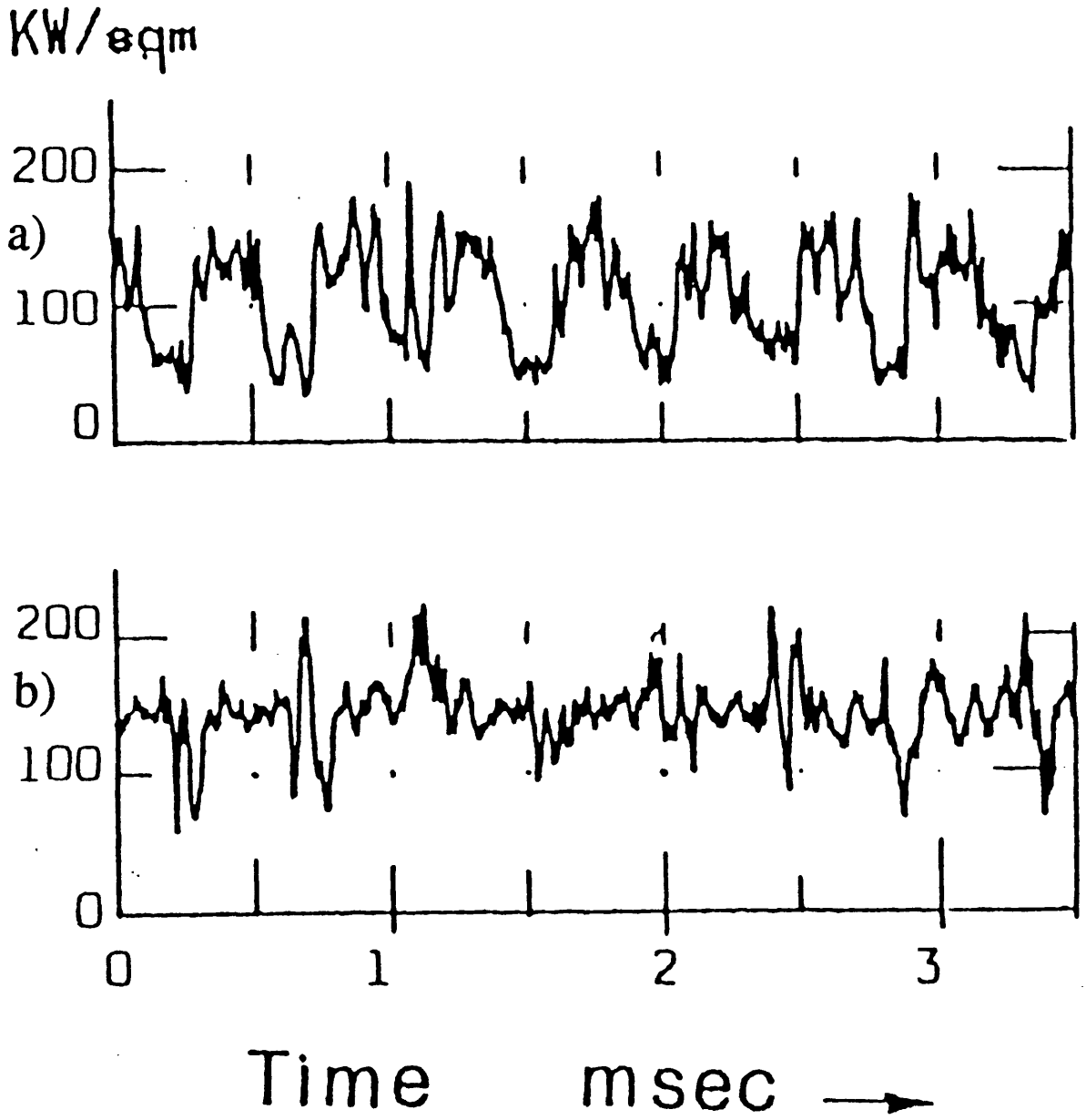

Figure (1.11) : Heat Transfer Time History for Two Points on Rotor Suction Surface Showing Forced Transition Due to NGV Passing [16]

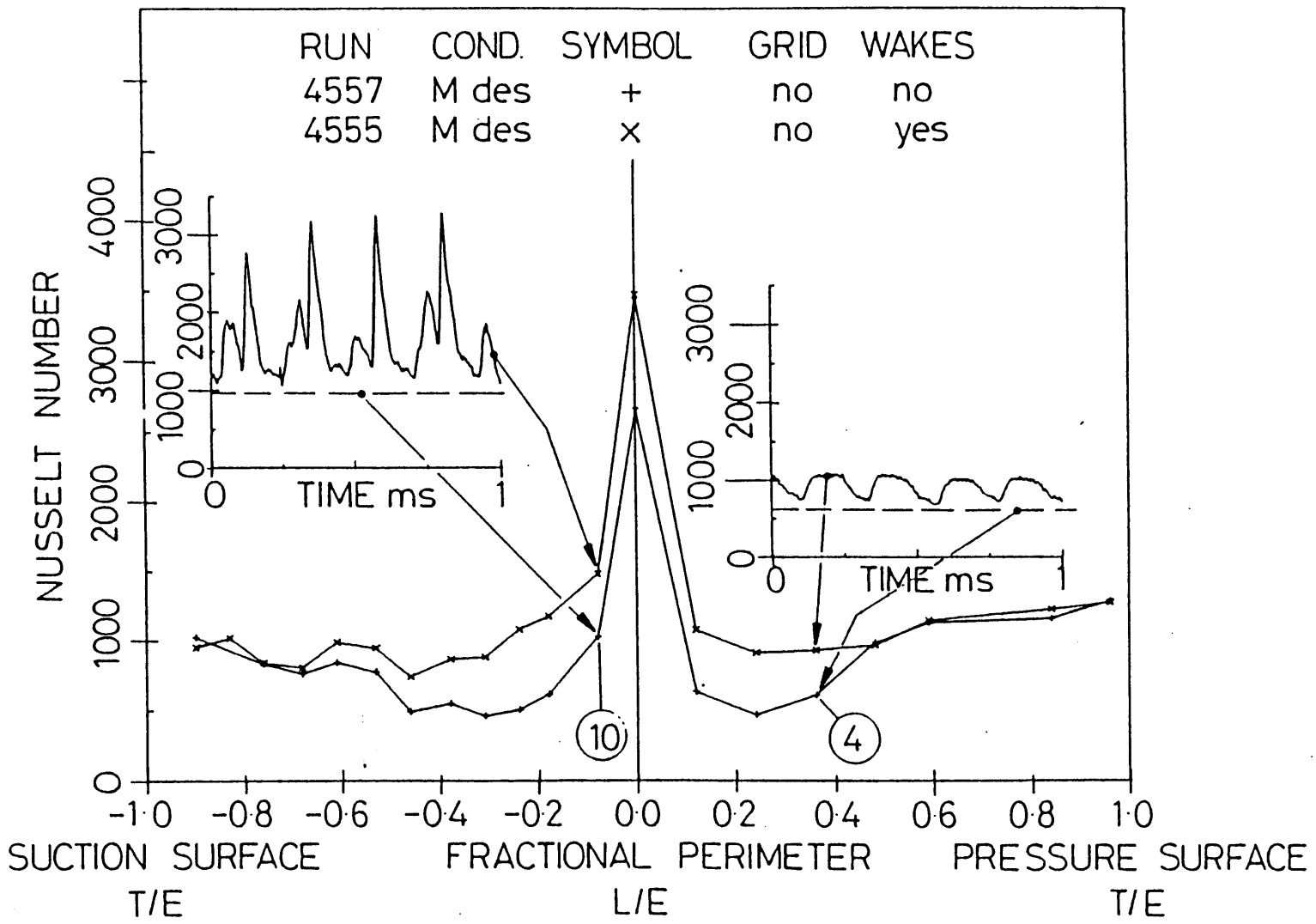

Figure (1.12) : Effect of Wakes on Rotor Nusselt Number in a Cascade [18]

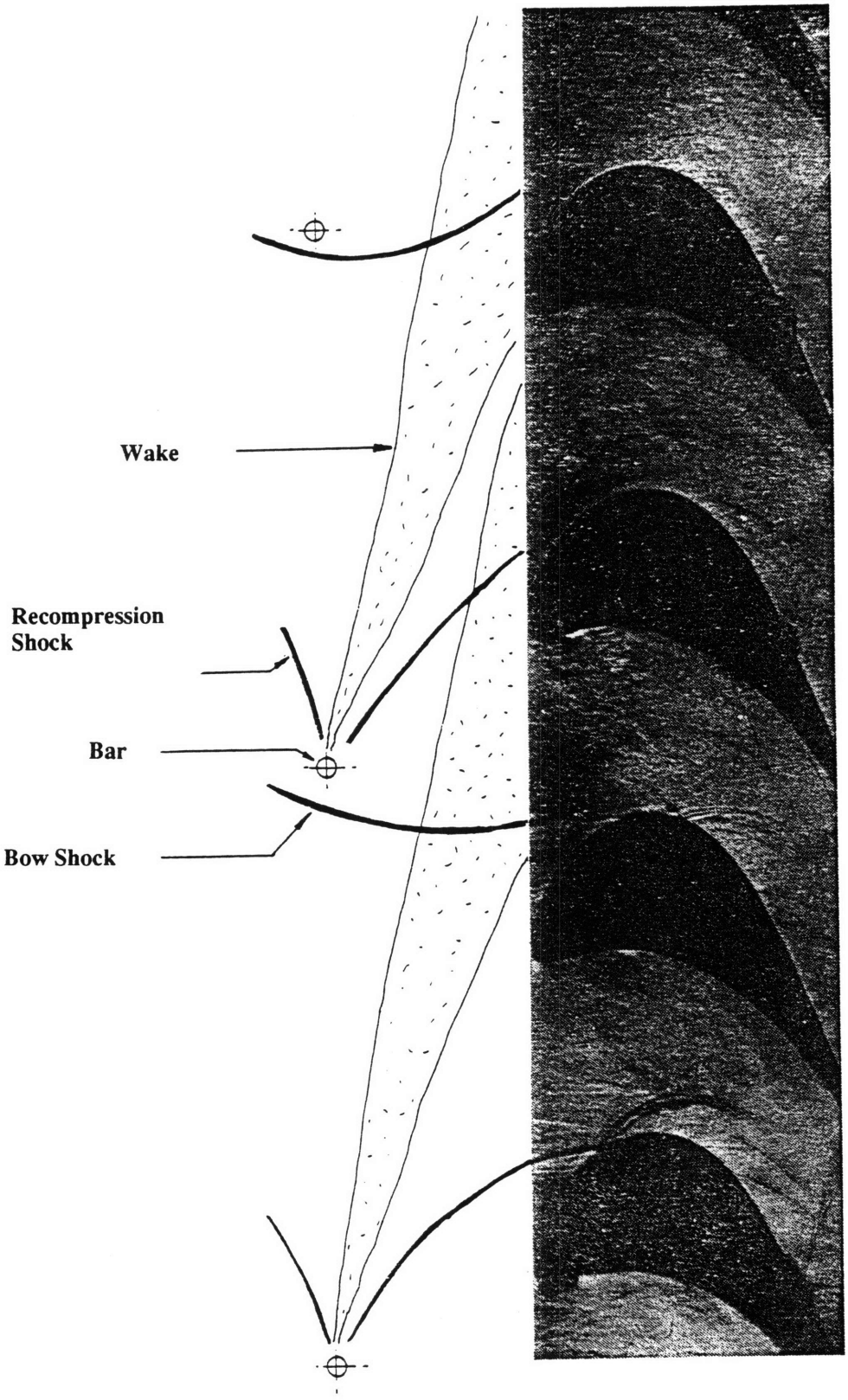

Figure (1.13) : Schlieren Photograph of Shock Wave Impingement on Rotor Suction Surface [21]

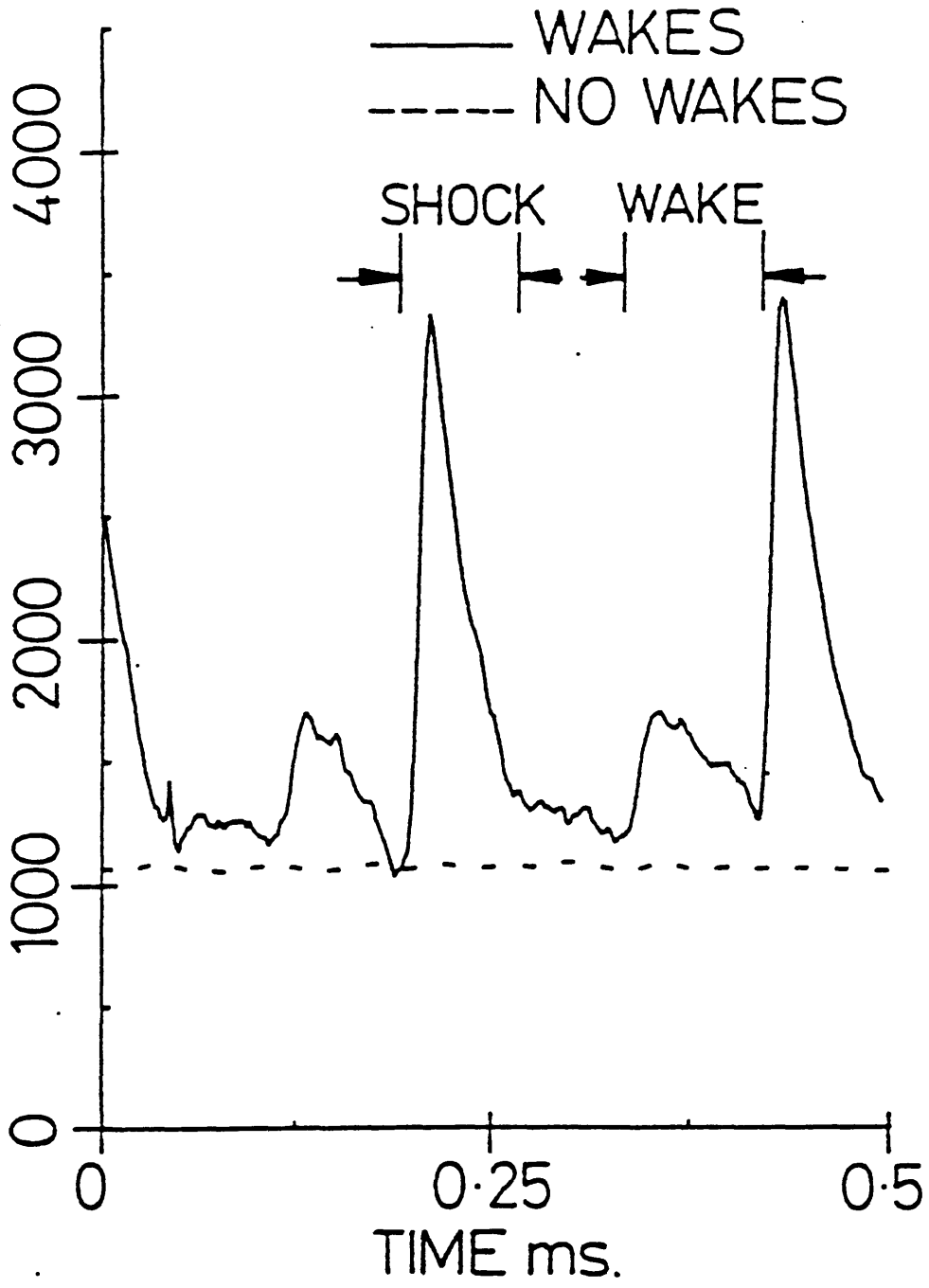

Figure (1.14) : Nusselt Number Time History for a Point at 25 Percent Wetted Surface on Rotor Suction Surface in a Cascade [18]

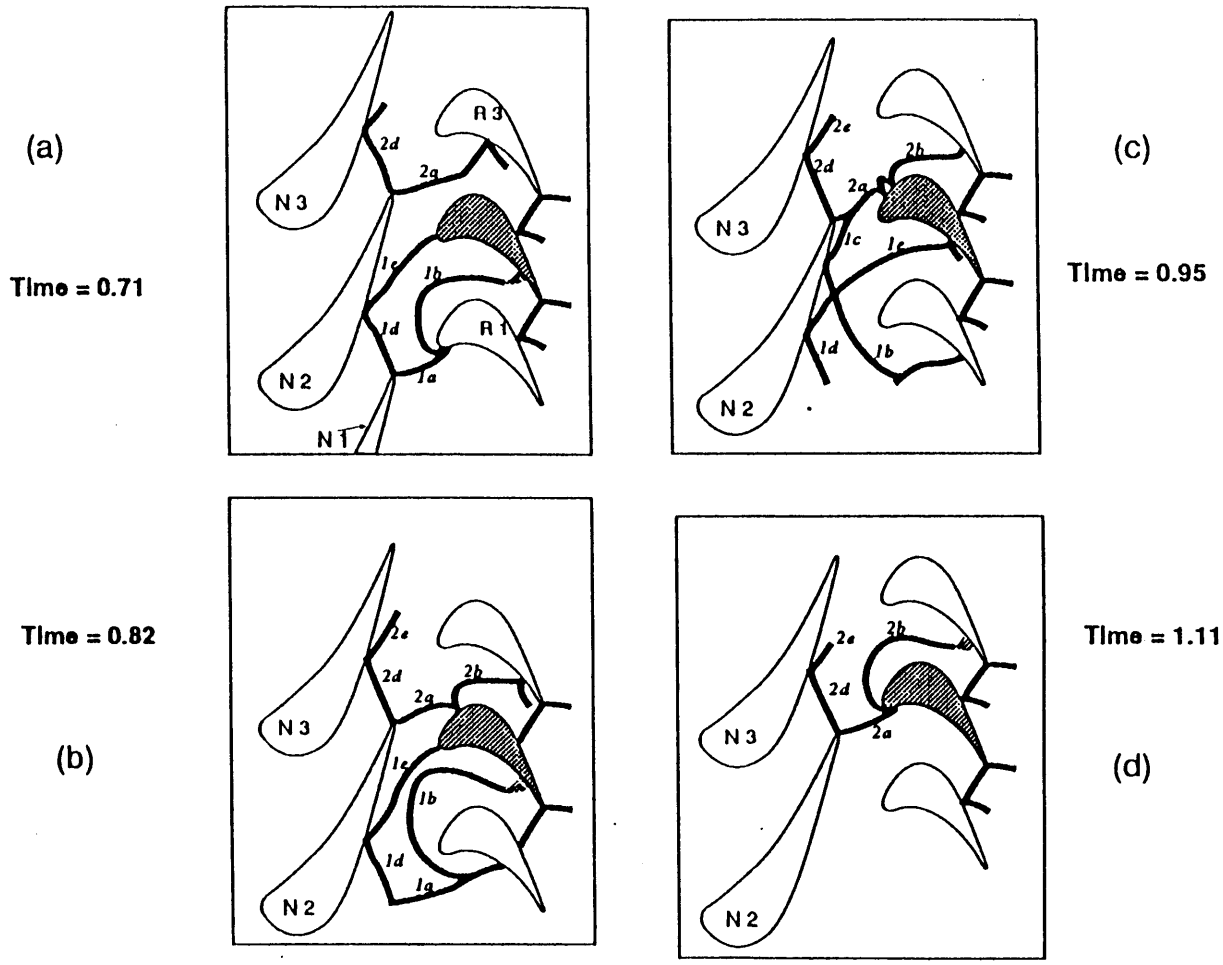

Figure (1.15) : Shock Wave Patterns at Eight Times During One Vane Passing [19]

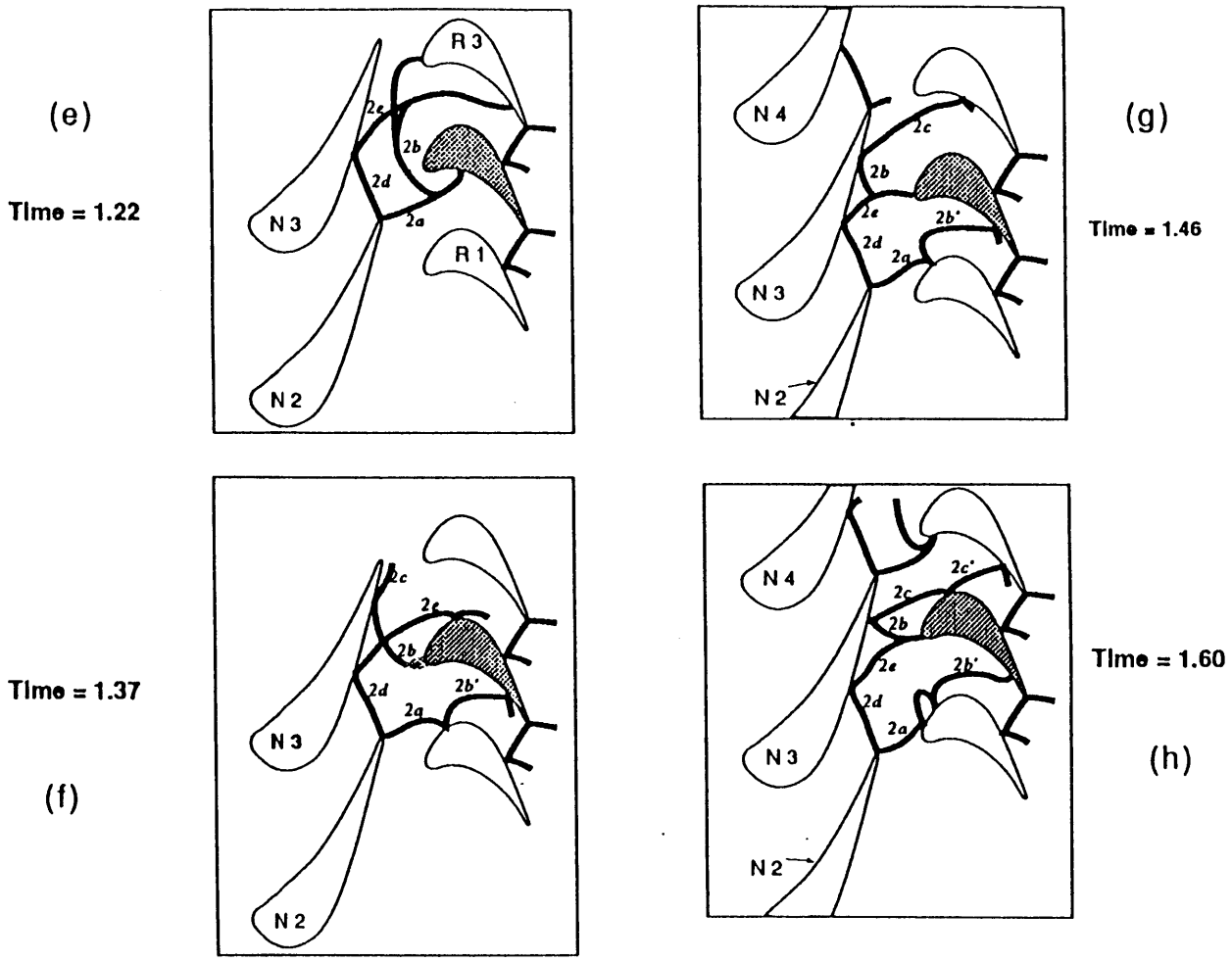

Figure (1.15) : Continued; Shock Wave Patterns at Eight Times During One Vane Passing [19]

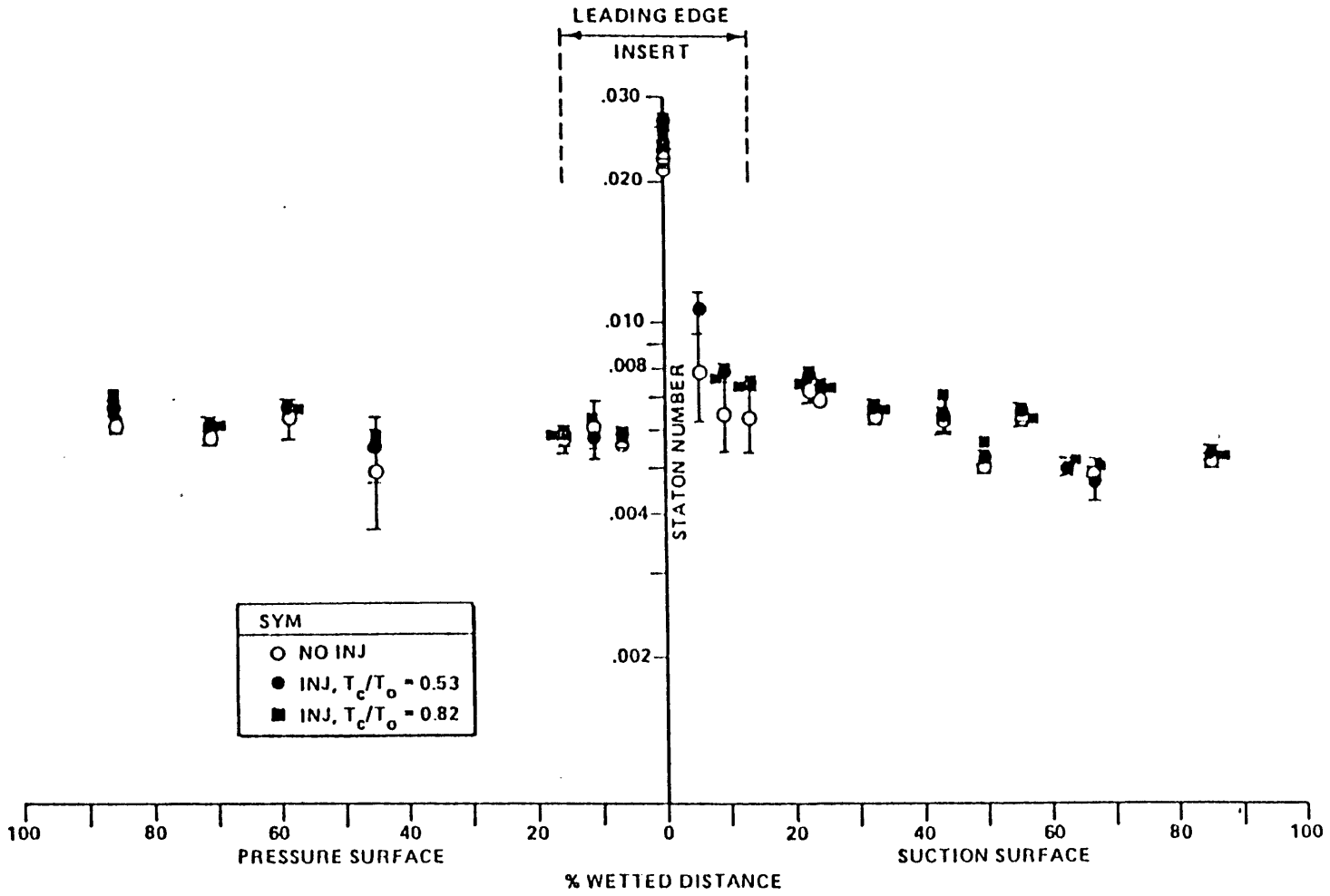

Figure (1.16) : Stanton Number Versus Percent Wetted Surface for Nozzle Guide Vane and No Nozzle Guide Vane Cooling [22]

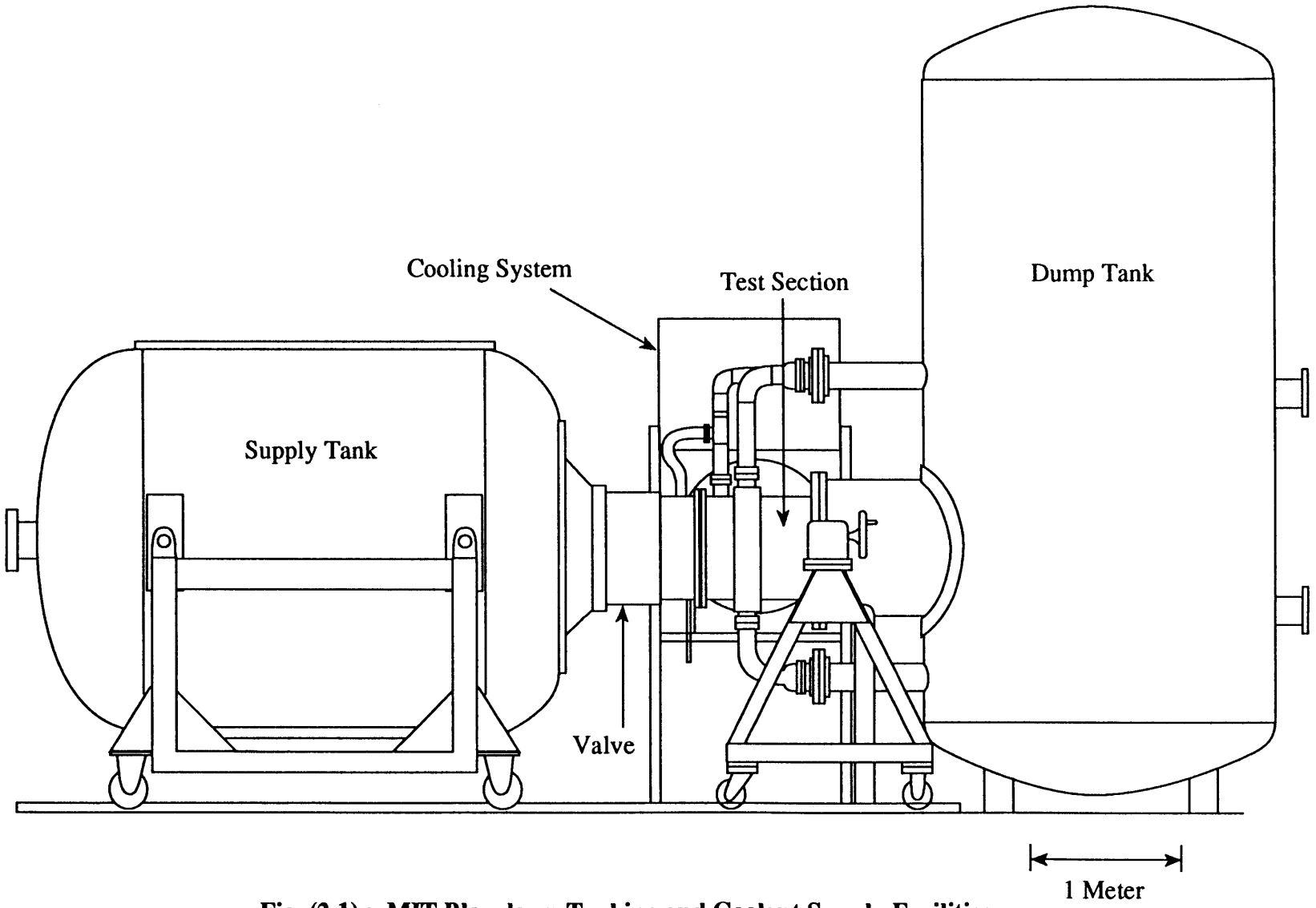

Fig. (2.1) : MIT Blowdown Turbine and Coolant Supply Facilities

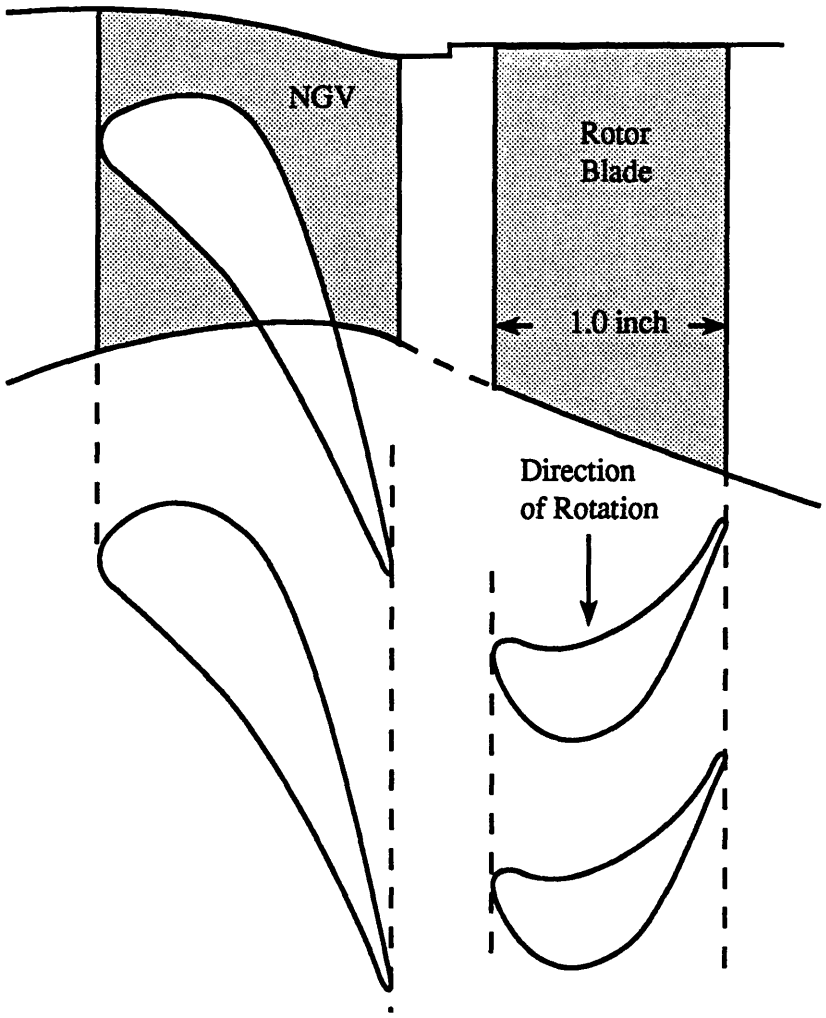

Figure (2.2) : Blade Profiles and Stage Configuration

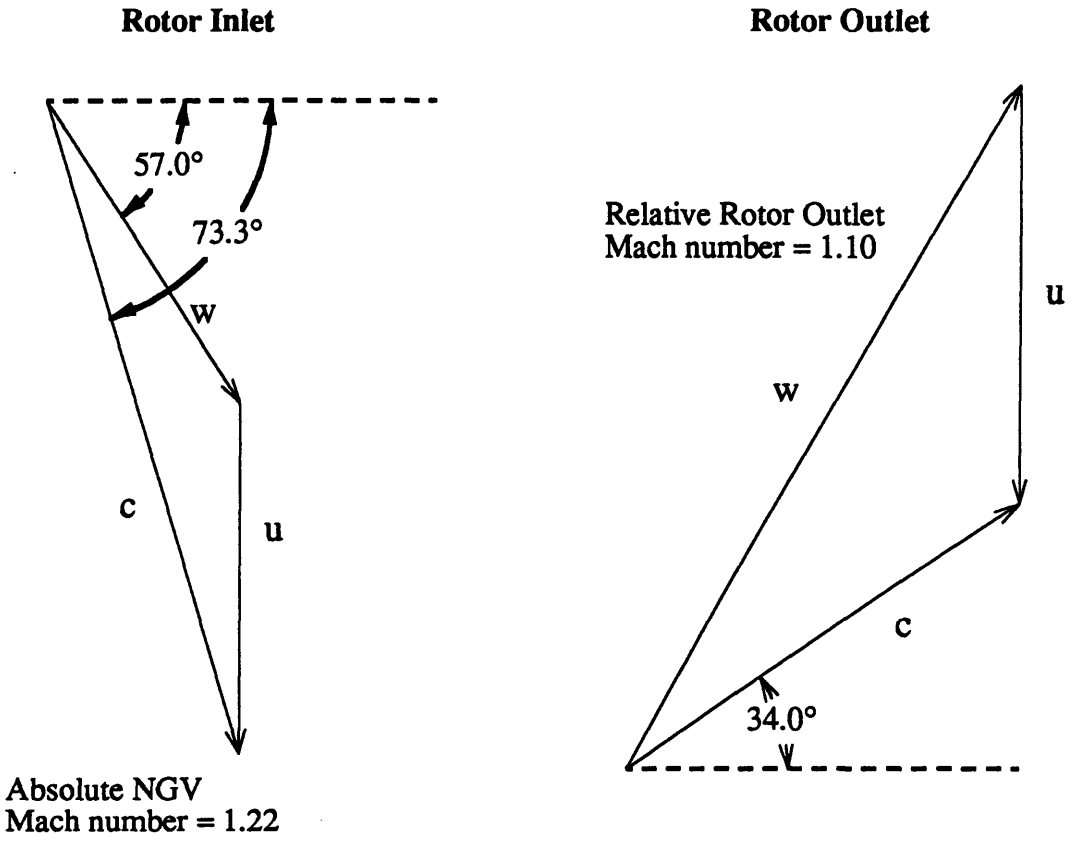

Figure (2.3) : Velocity Trianges for Rotor Inlet and Exit at Mid-Span

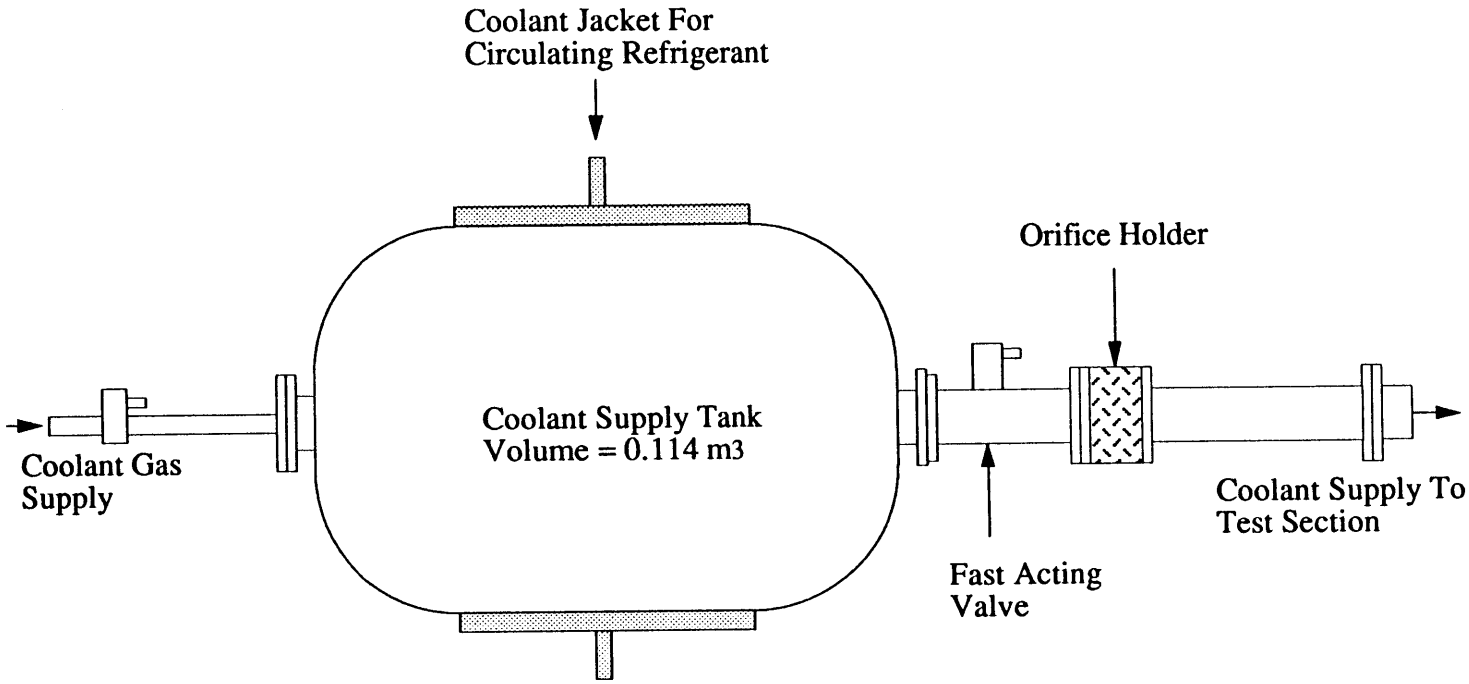

Figure (2.4) : Diagram of Coolant Supply Facility

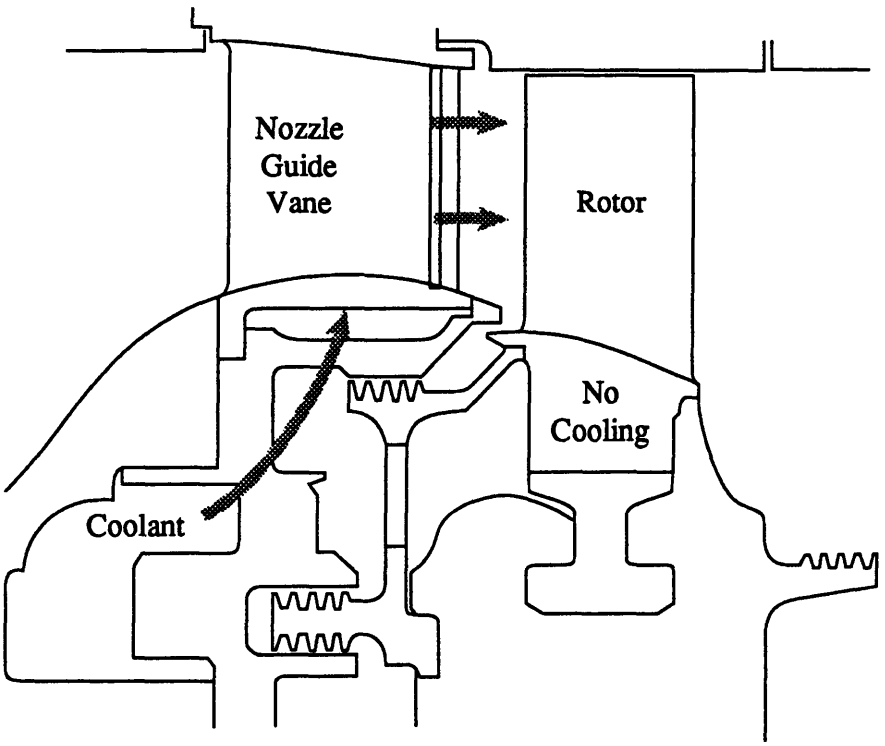

Figure (2.5) : Flow Path of Coolant for NGV Cooling Only Tests

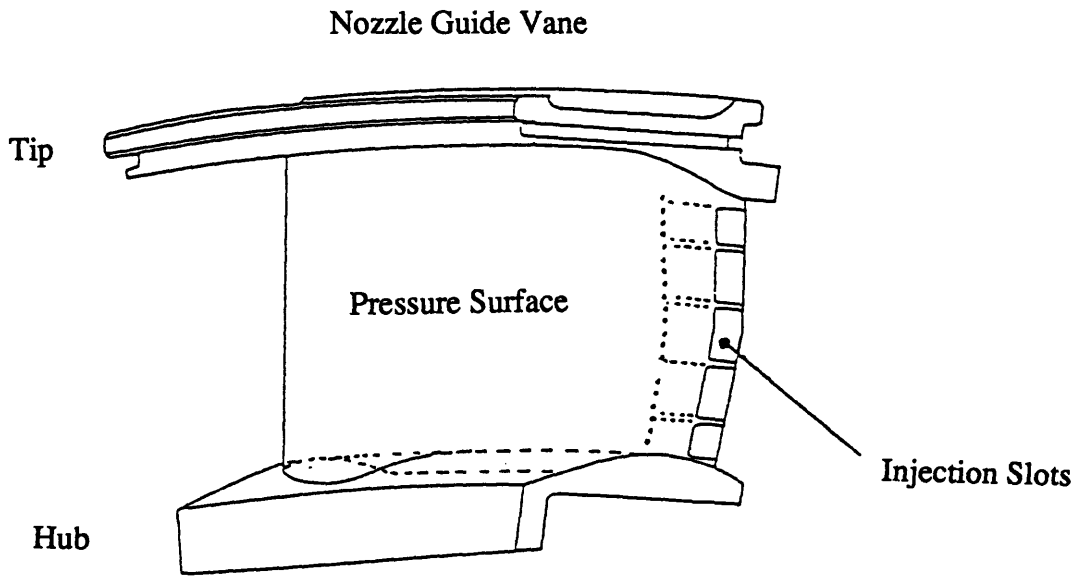

Figure (2.6) : Nozzle Guide Vane and Trailing Edge Cooling Slots on the Pressure Surface

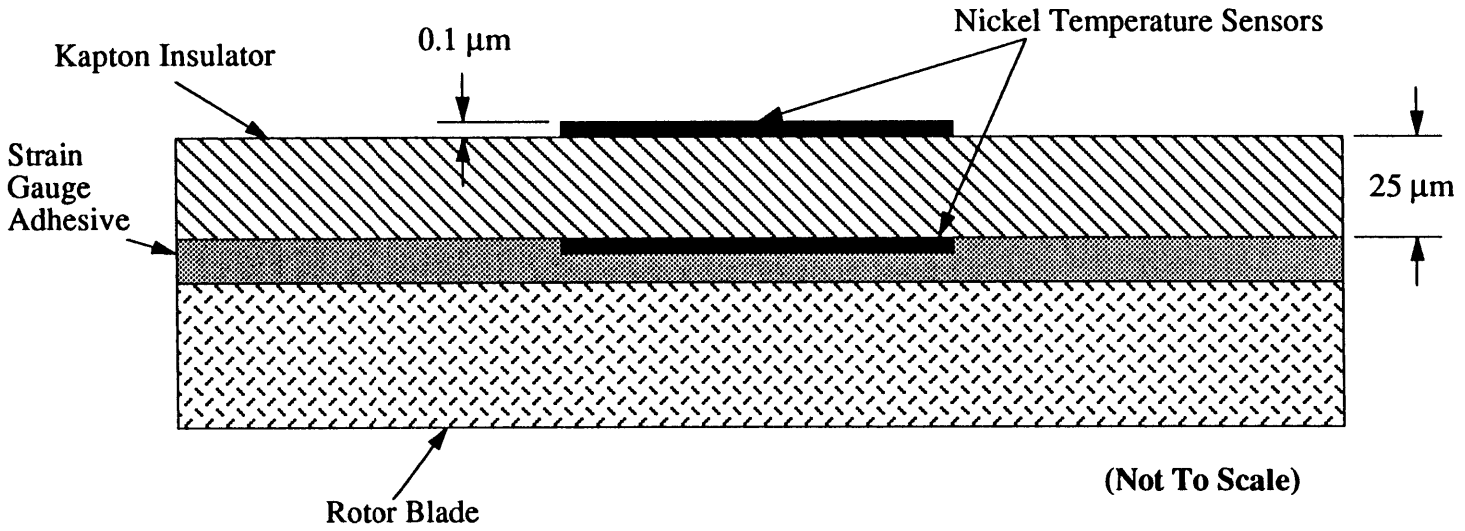

Figure (2.7) : Cross Sectional Schematic of Heat Flux Gauge

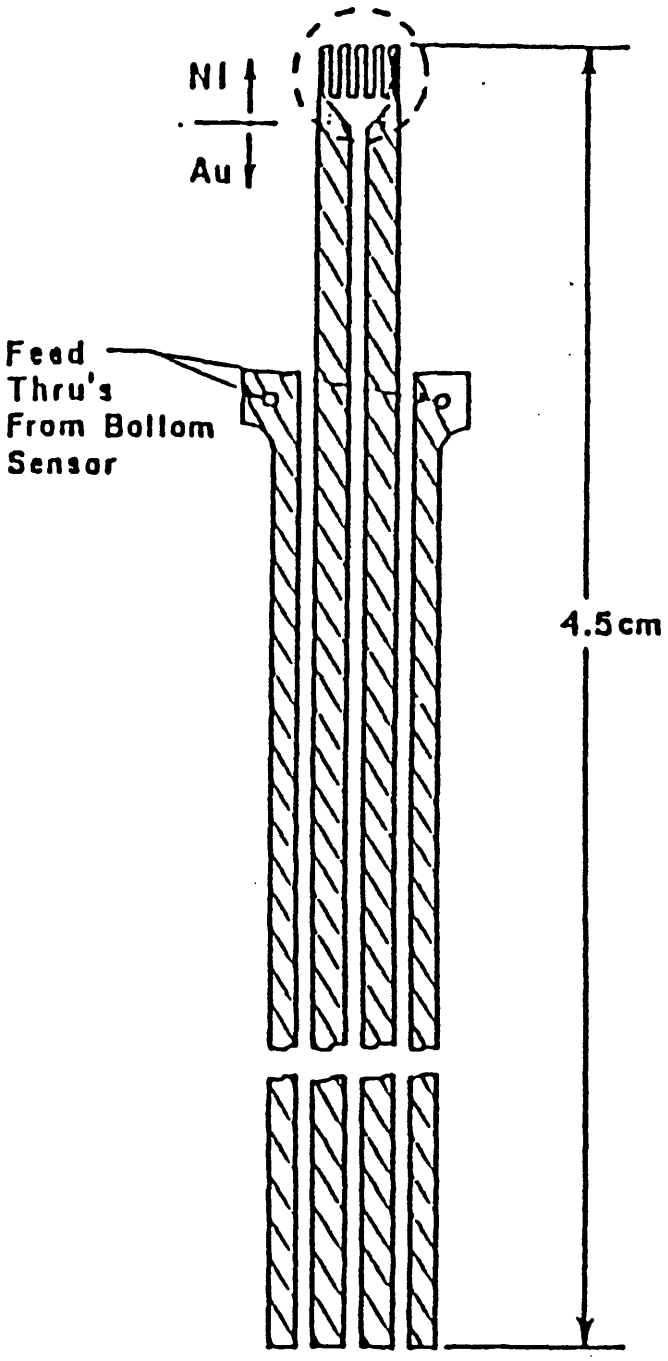

Figure (2.8) : Drawing of a Heat Flux Gauge Before Mounting

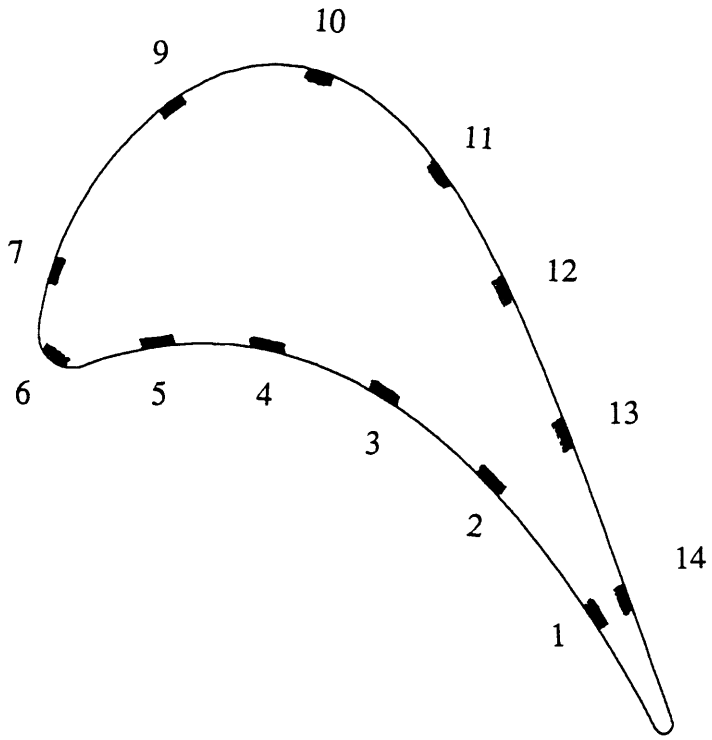

Figure (2.9) : Picture of Heat Flux Gauge Positions on the Rotor

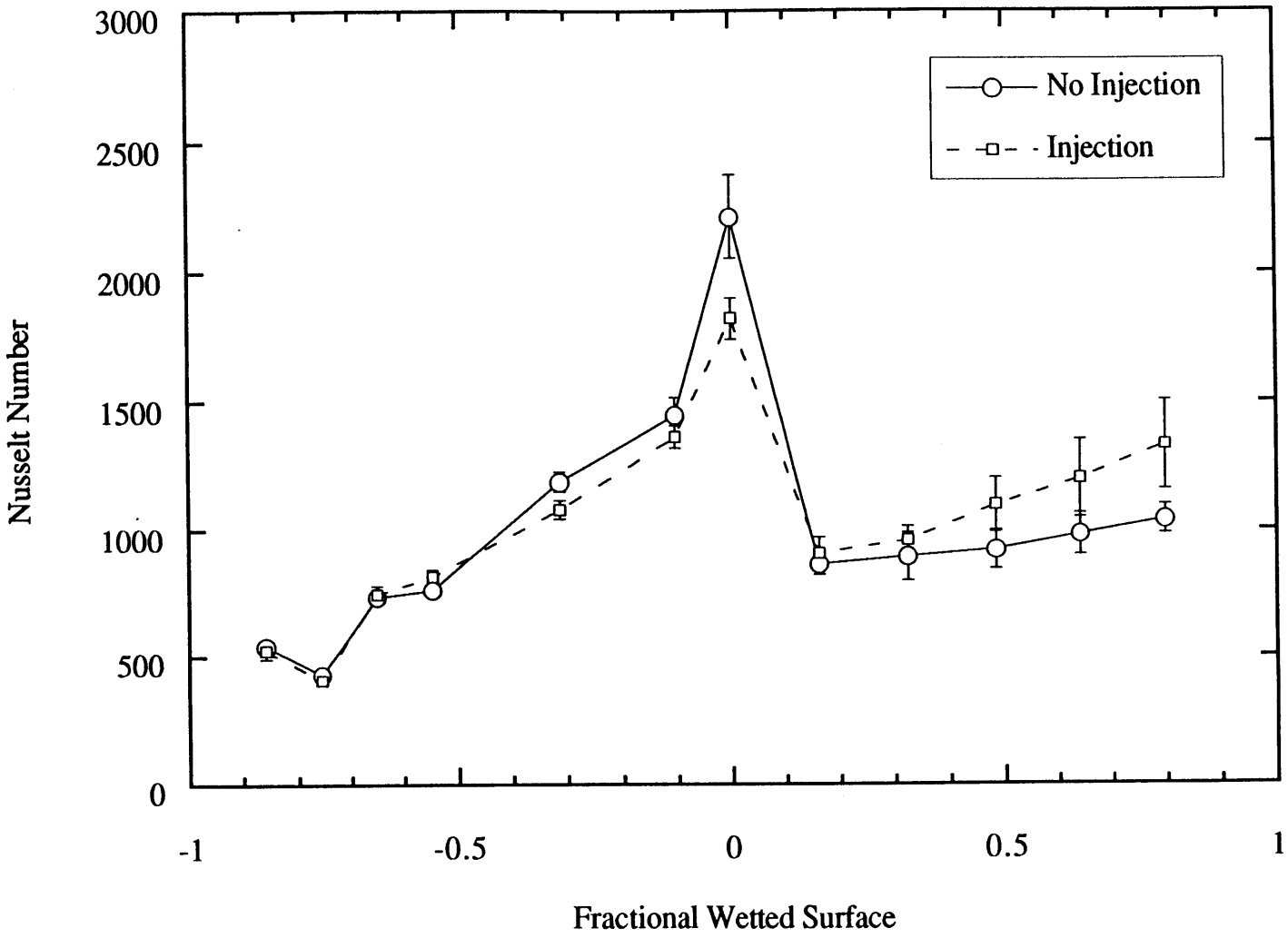

Figure (2.10) : Nusselt Number Distribution for Uncooled (T47) and Cooled (T56) NGV [19]

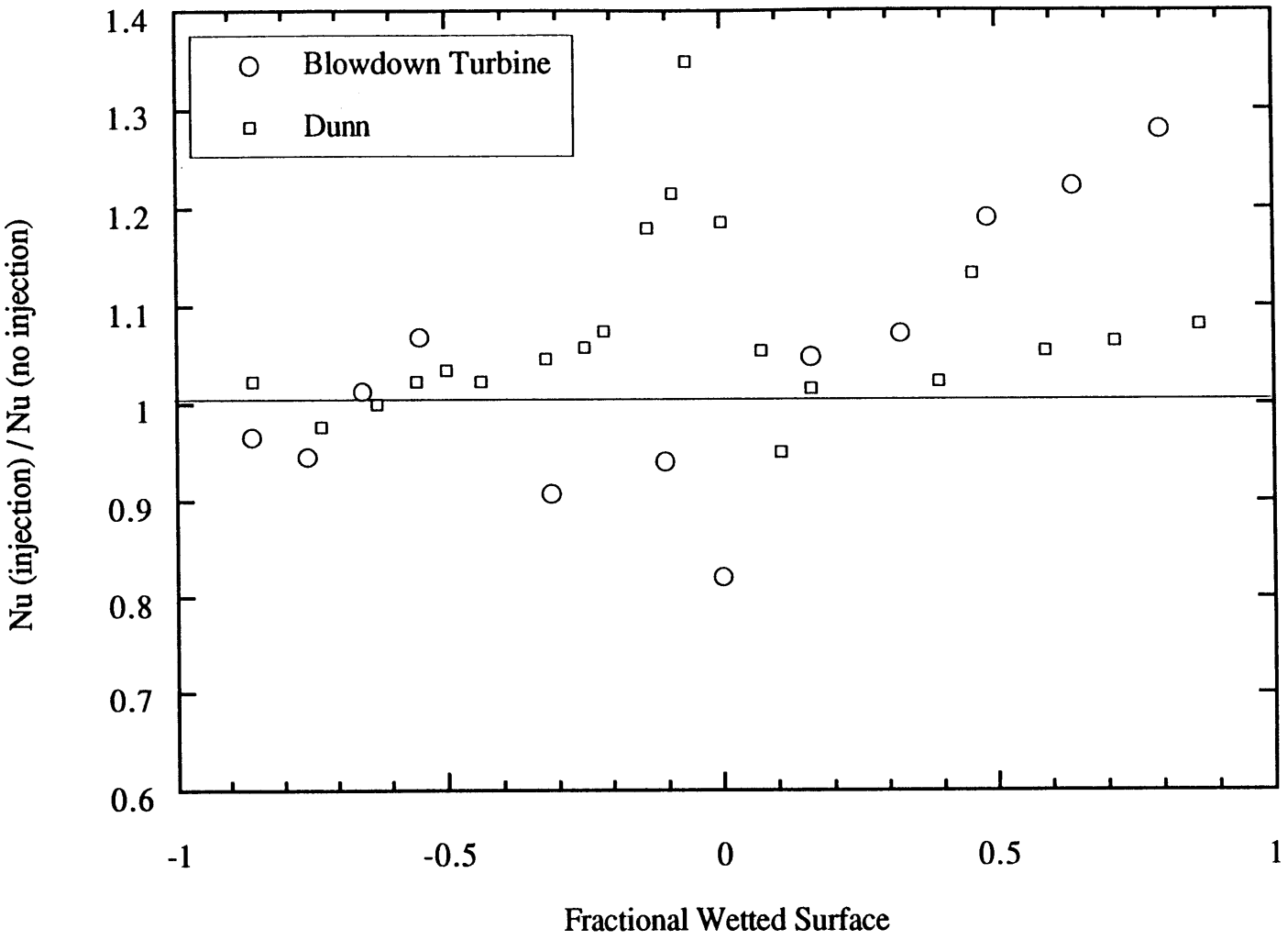

Figure (2.11) : Ratio of Cooled to Uncooled Heat Transfer for the Blowdown Turbine and Dunn's Results [19]

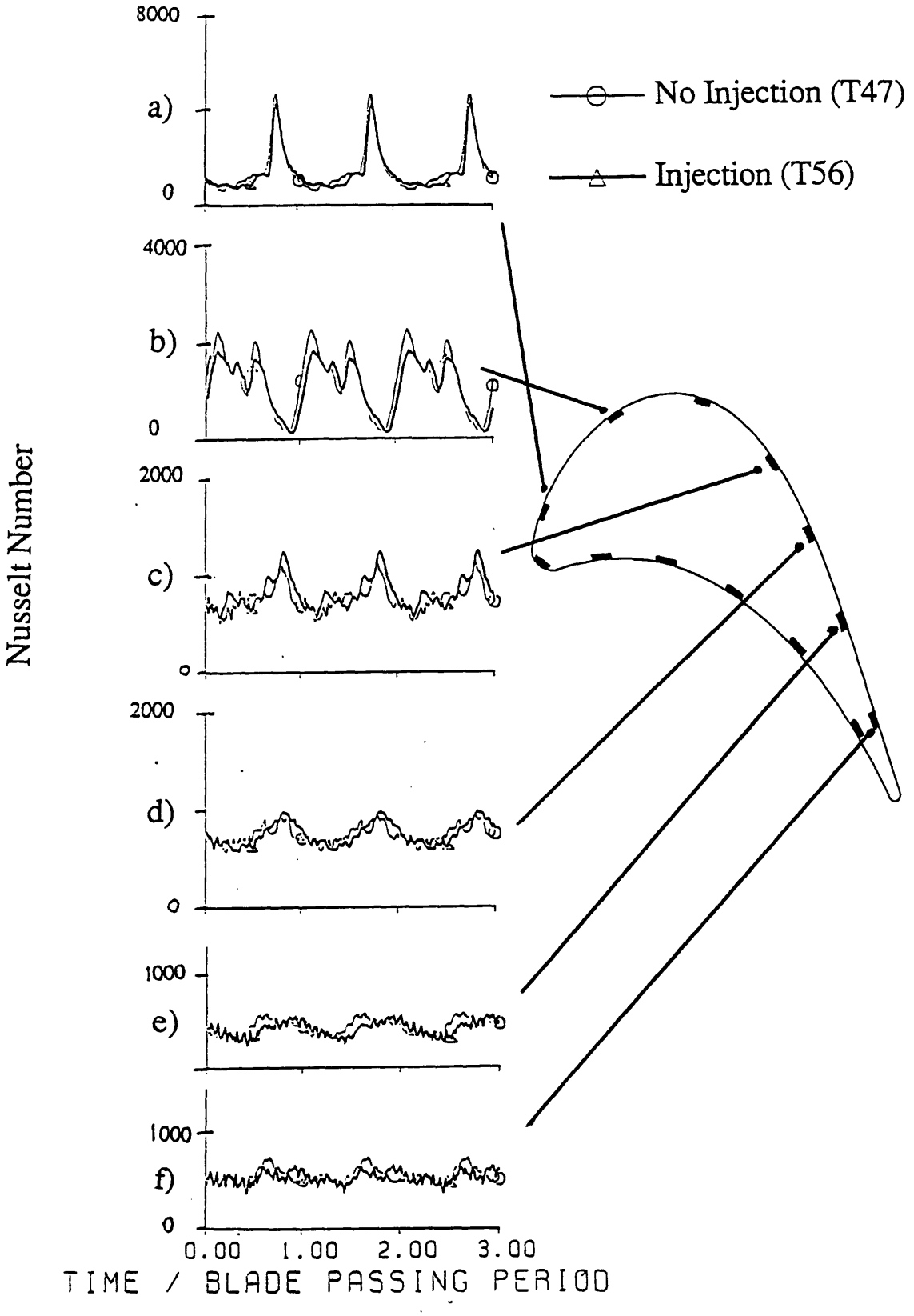

Figure (2.12) : Nusselt Number Versus Time From Suction Surface Gauges for the Cooled and Uncooled Nozzle Guide Vane Cases [19]

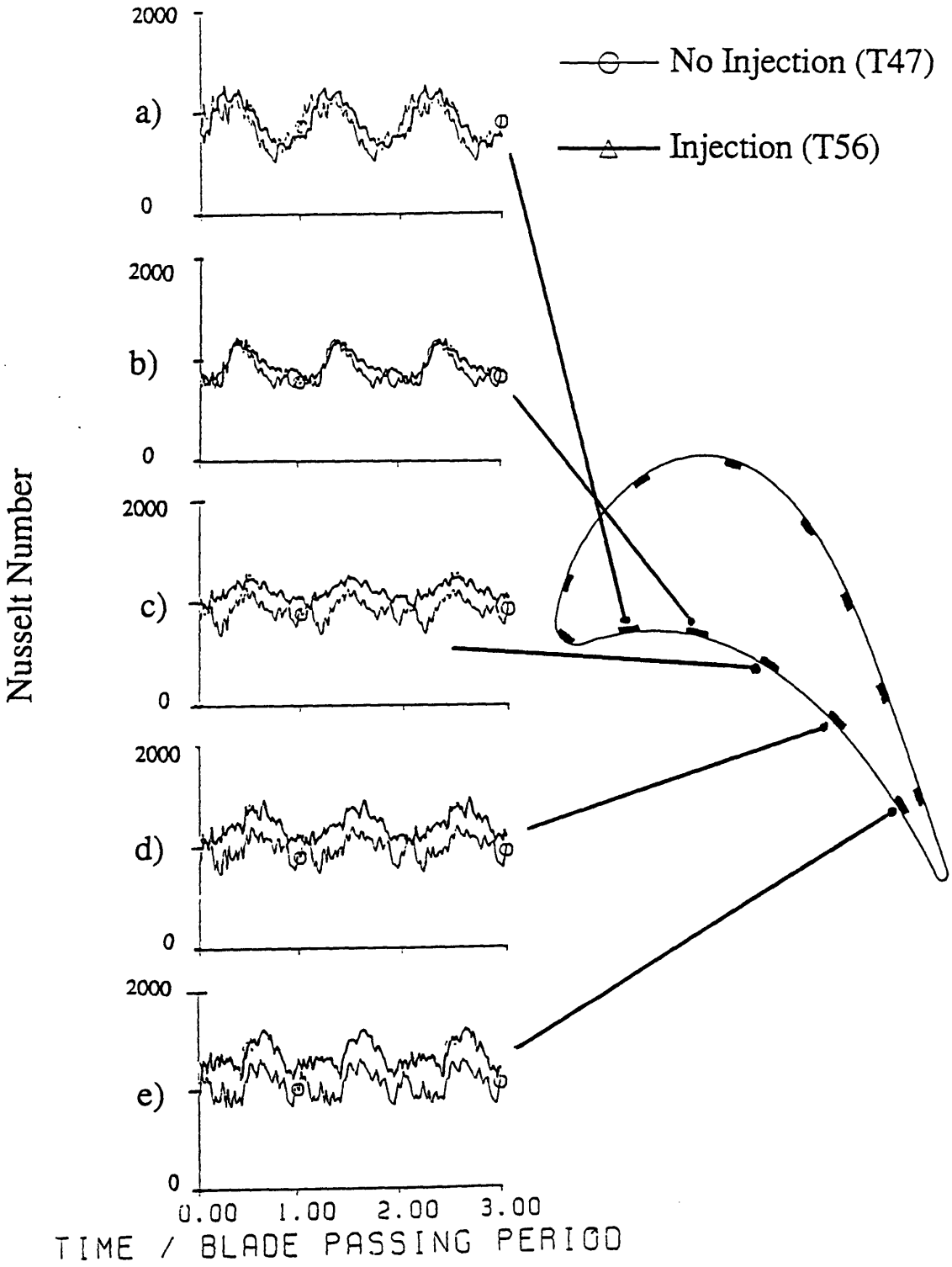

Figure (2.13) : Nusselt Number Versus Time From Pressure Surface Gauges for the Cooled and Uncooled Nozzle Guide Vane Cases [19]

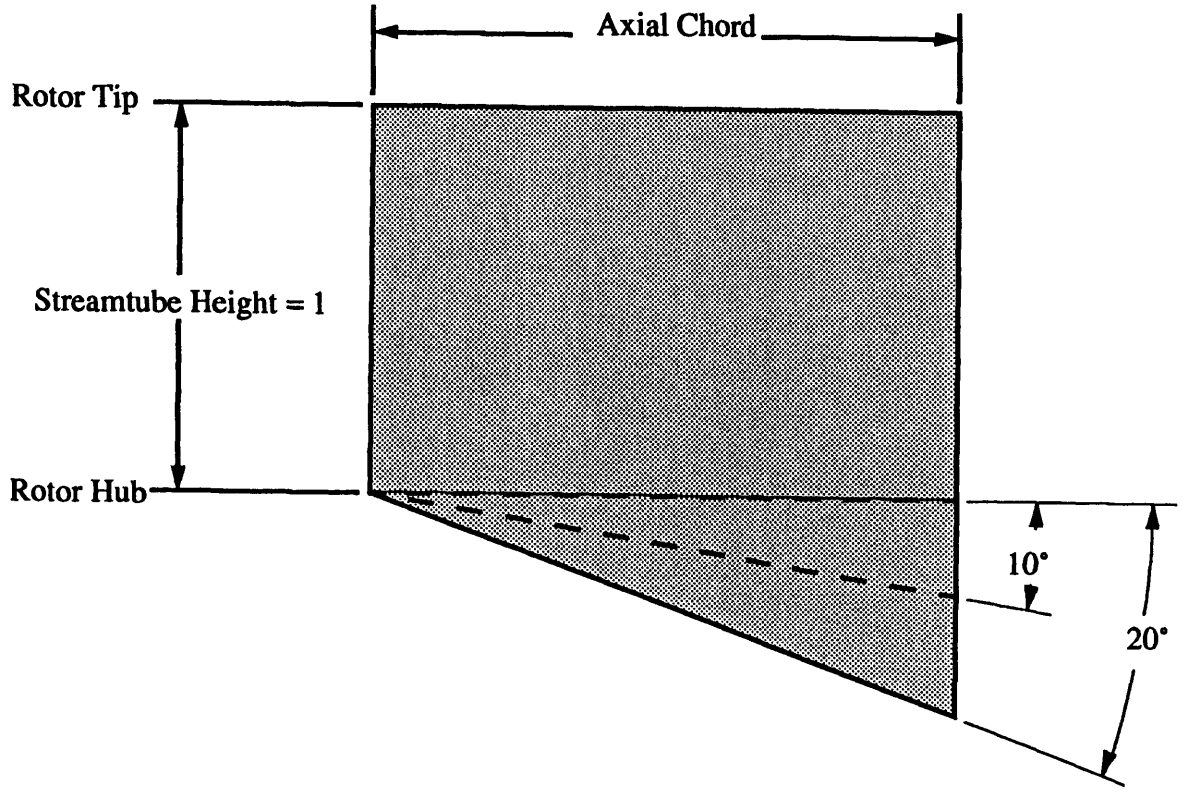

Figure (3.1) : Variations in Streamtube Height for Divergent Angles of 0°, 10°, and 20°

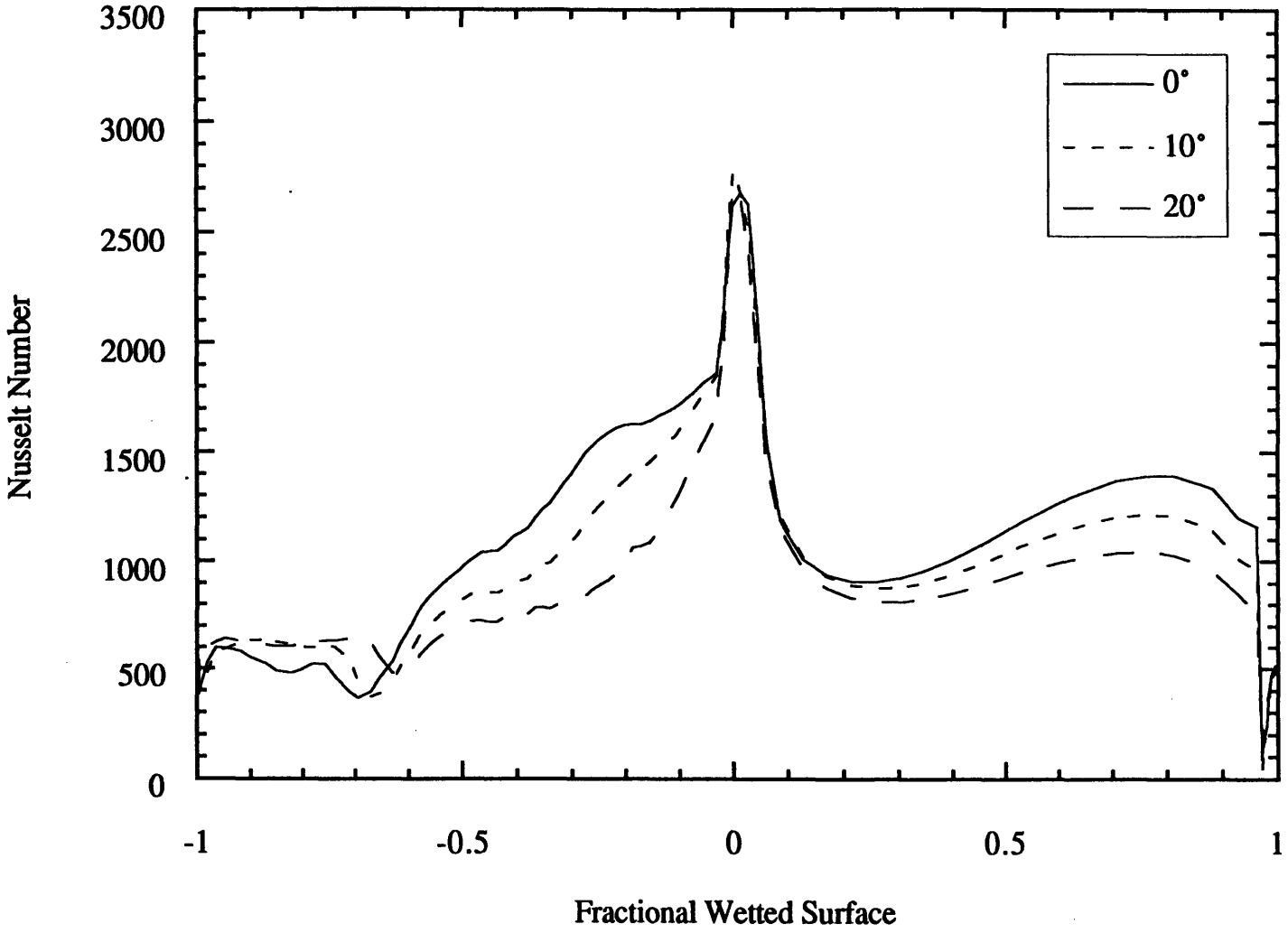

Figure (3.2) : Effect of Streamtube Height on Nusselt Number

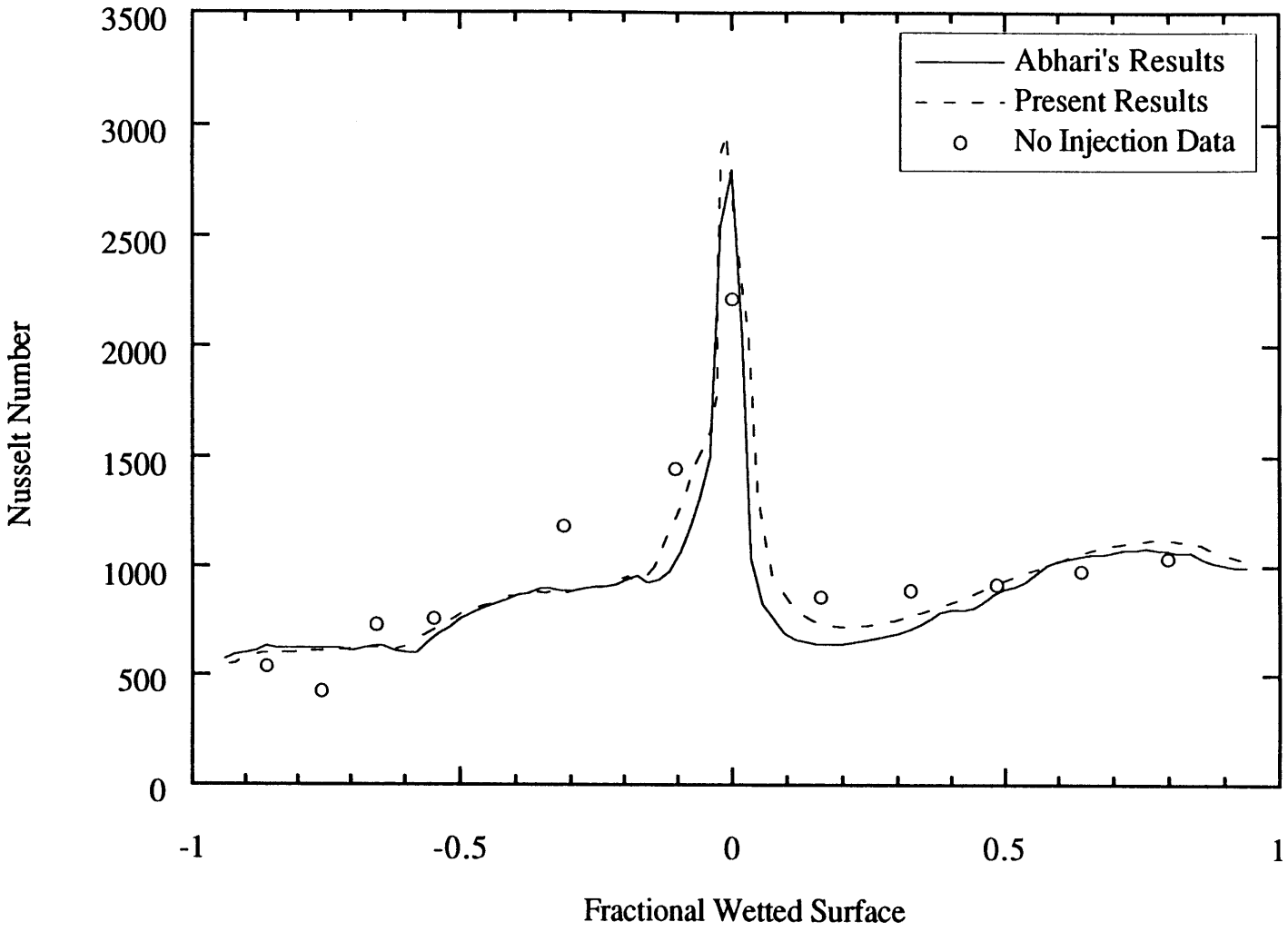

Figure (3.3) UNSFLO Calculated Steady Nusselt Numbers Versus Fractional Wetted Surface for the Present Results and Those of Abhari [19]

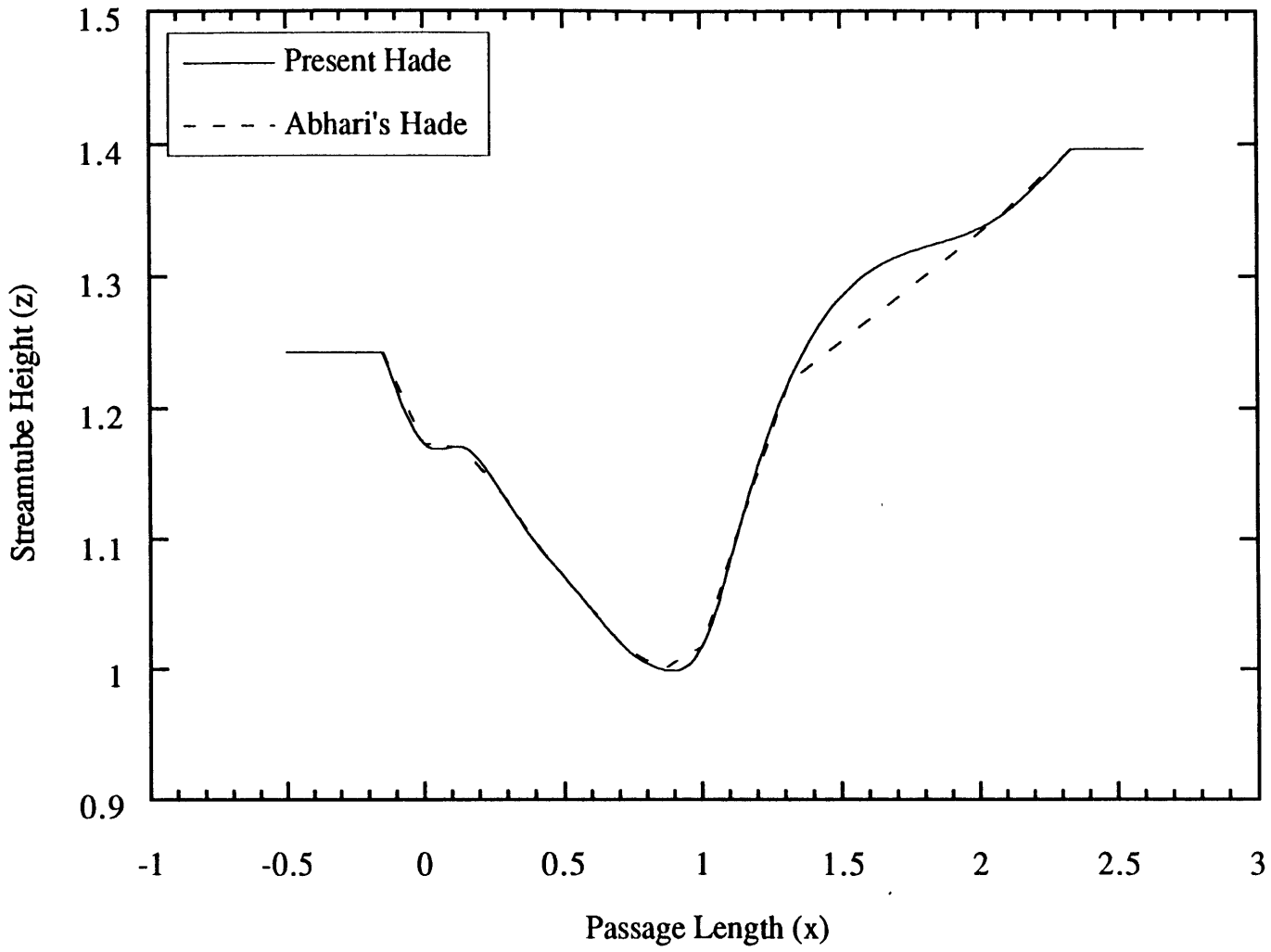

Figure (3.4) : Streamtube Height Versus Passage Length for the Present Results and Those of Abhari [19]

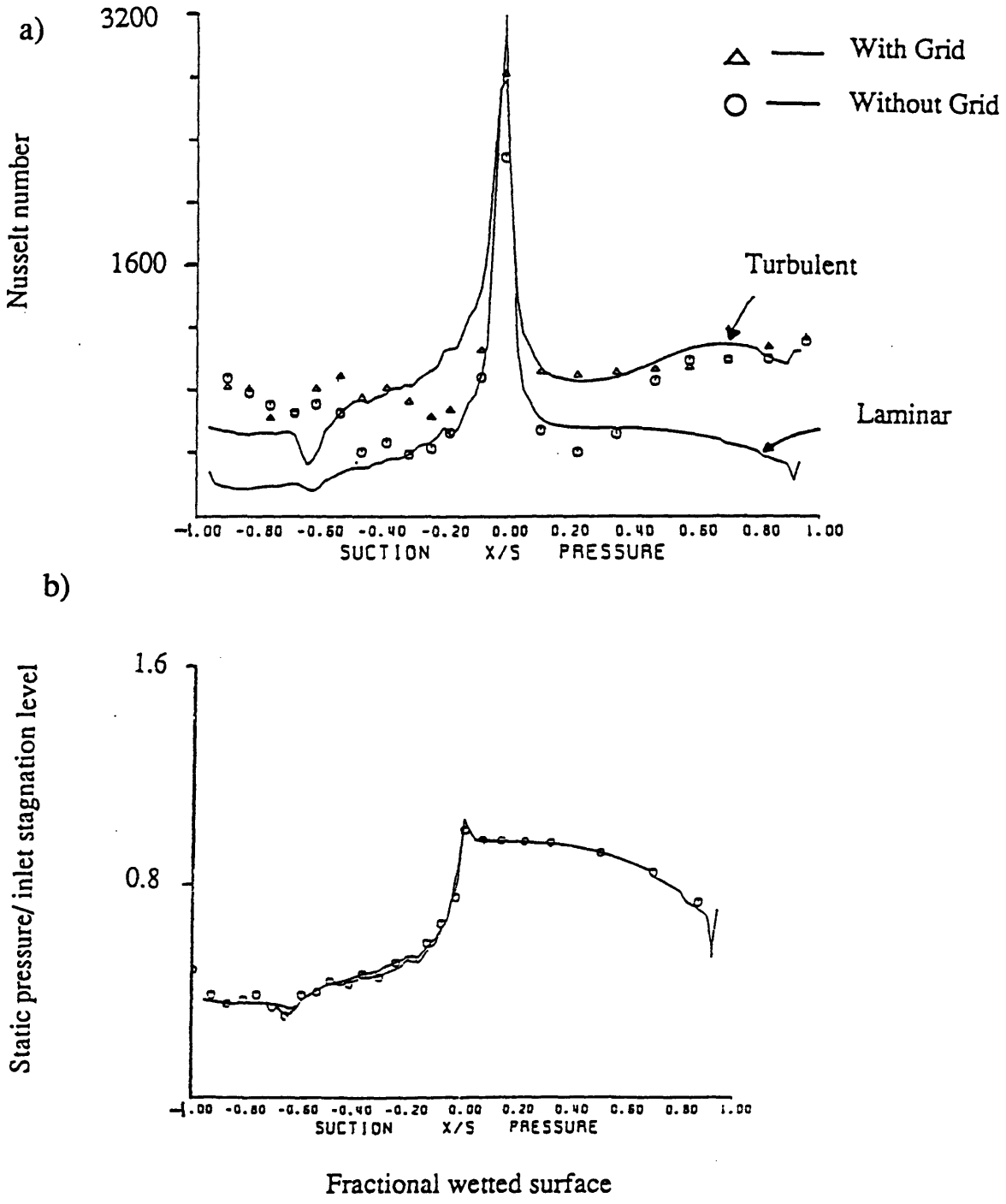

Figure (3.5) : Steady Nusselt Numbers and Surface Static Pressure Distributions for Steady UNSFLO Calculations by Abhari and Experimental Data From Ashworth [19]

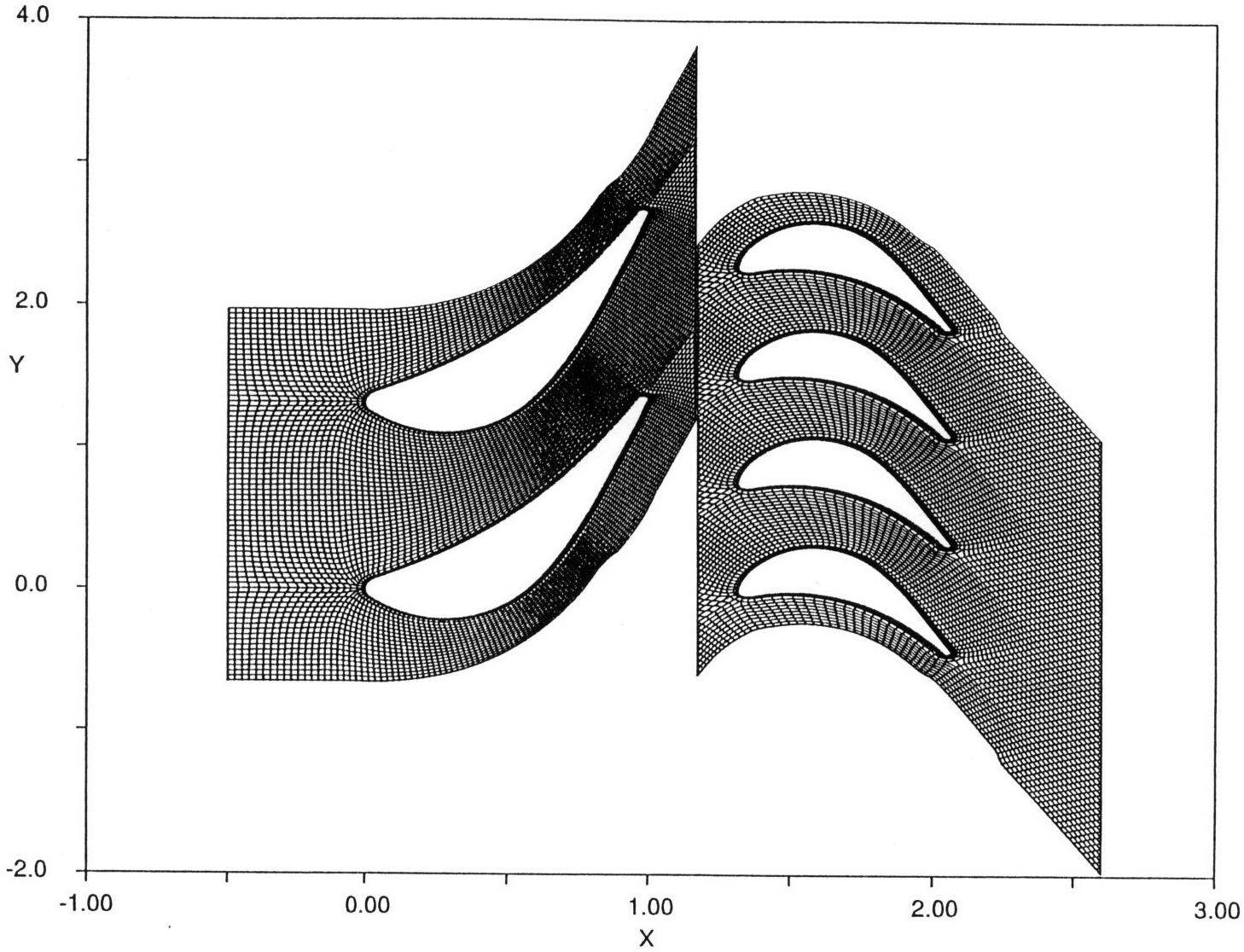

Figure (3.6) : Blade Setup and Grid Used in UNSFLO Calculations

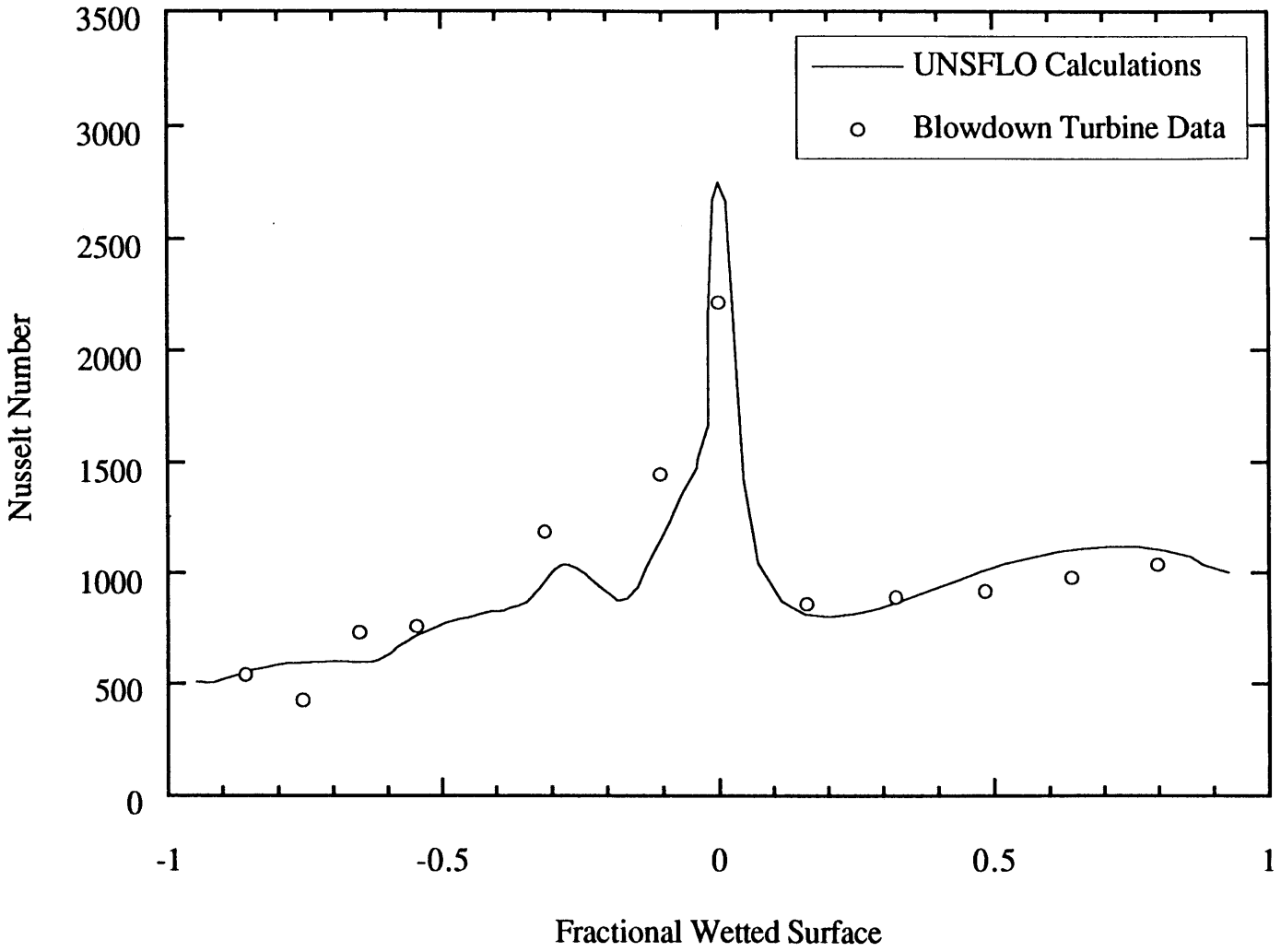

Figure (4.1) : Averaged Unsteady Nusselt Number Versus Fractional Wetted Surface for UNSFLO Calculations and Blowdown Turbine Data

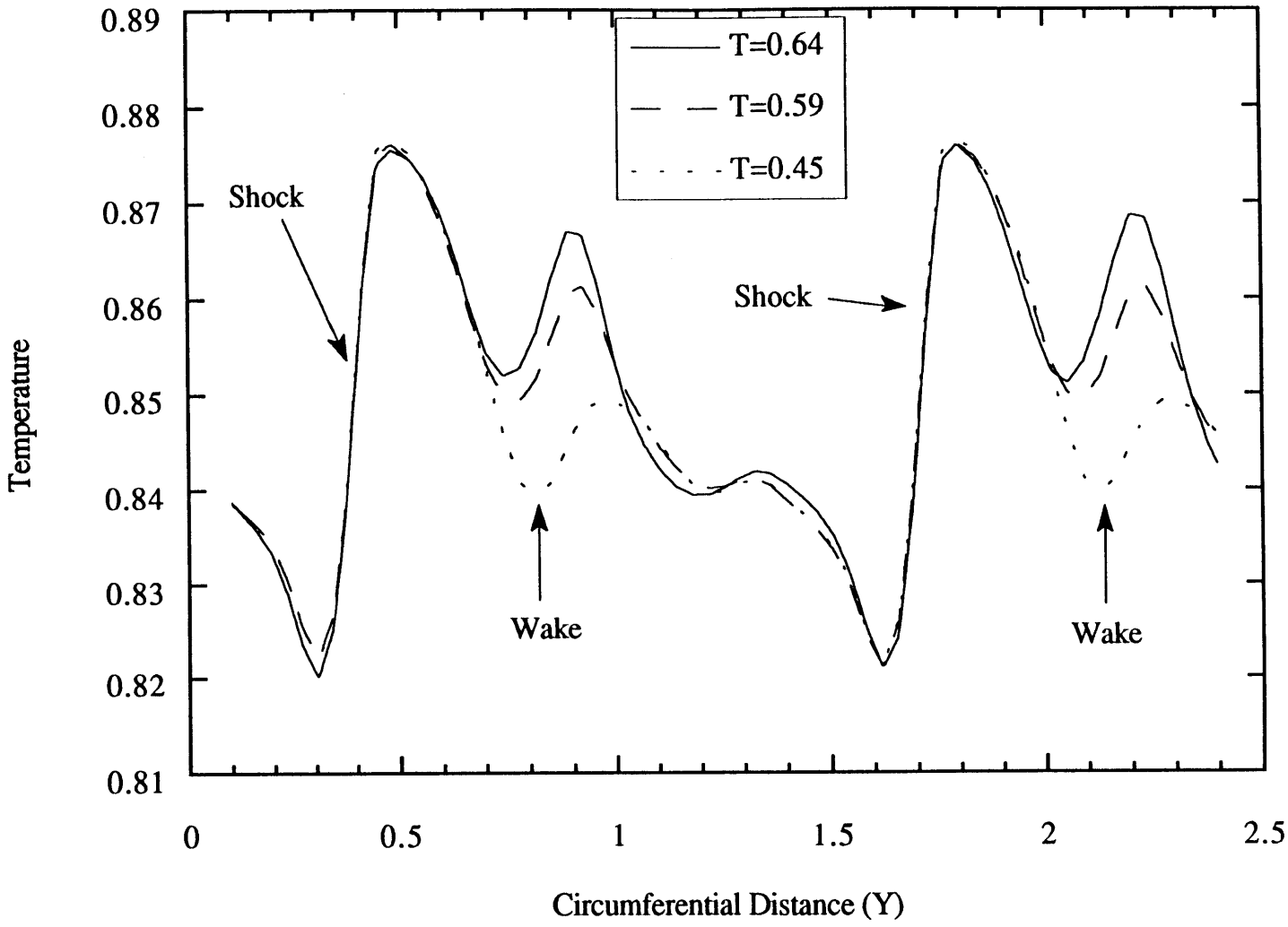

Figure (4.2) : Calculated Temperature Versus Circumferential Distance at X=1.17

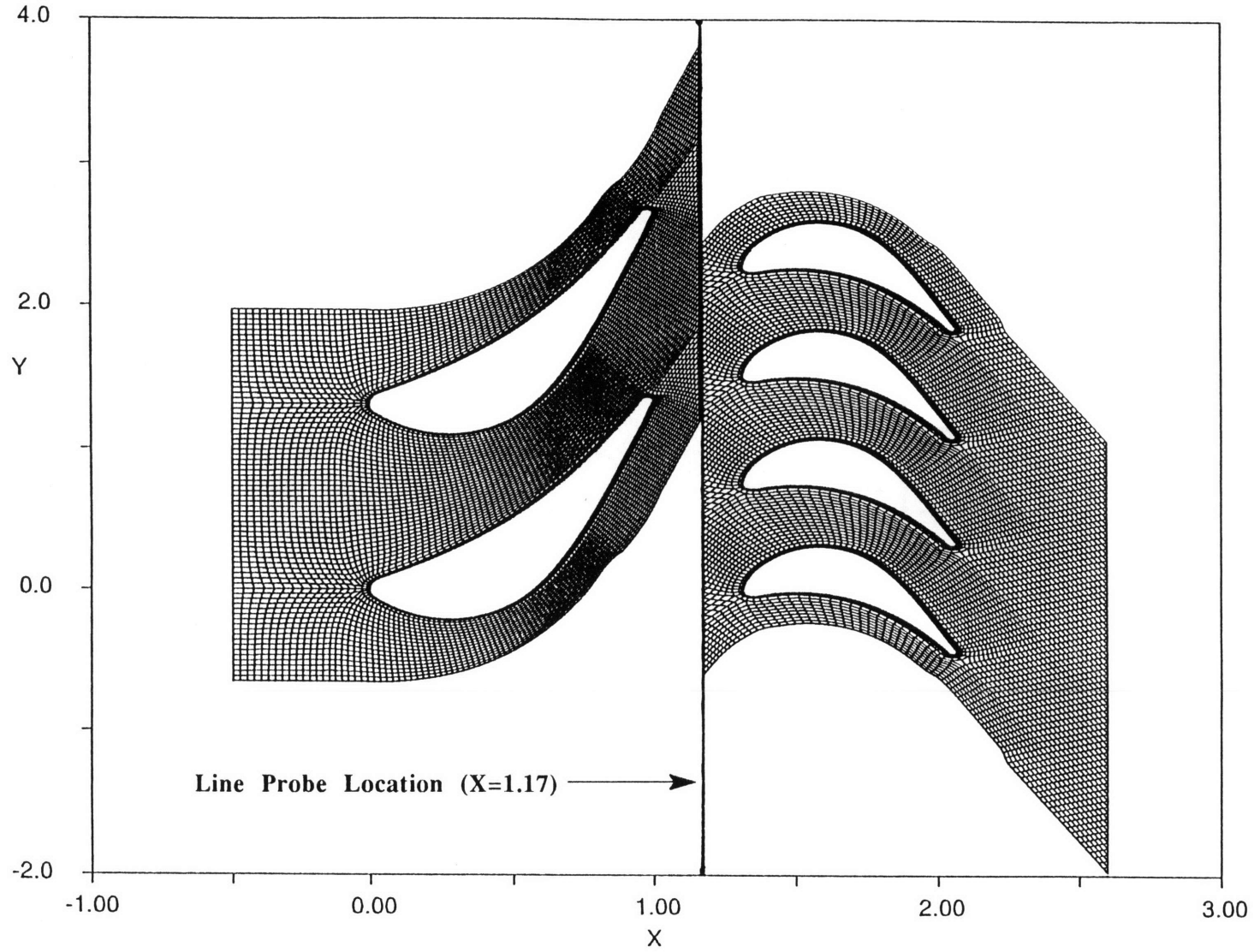

Figure (4.3) : Location of Line Probe at X=1.17

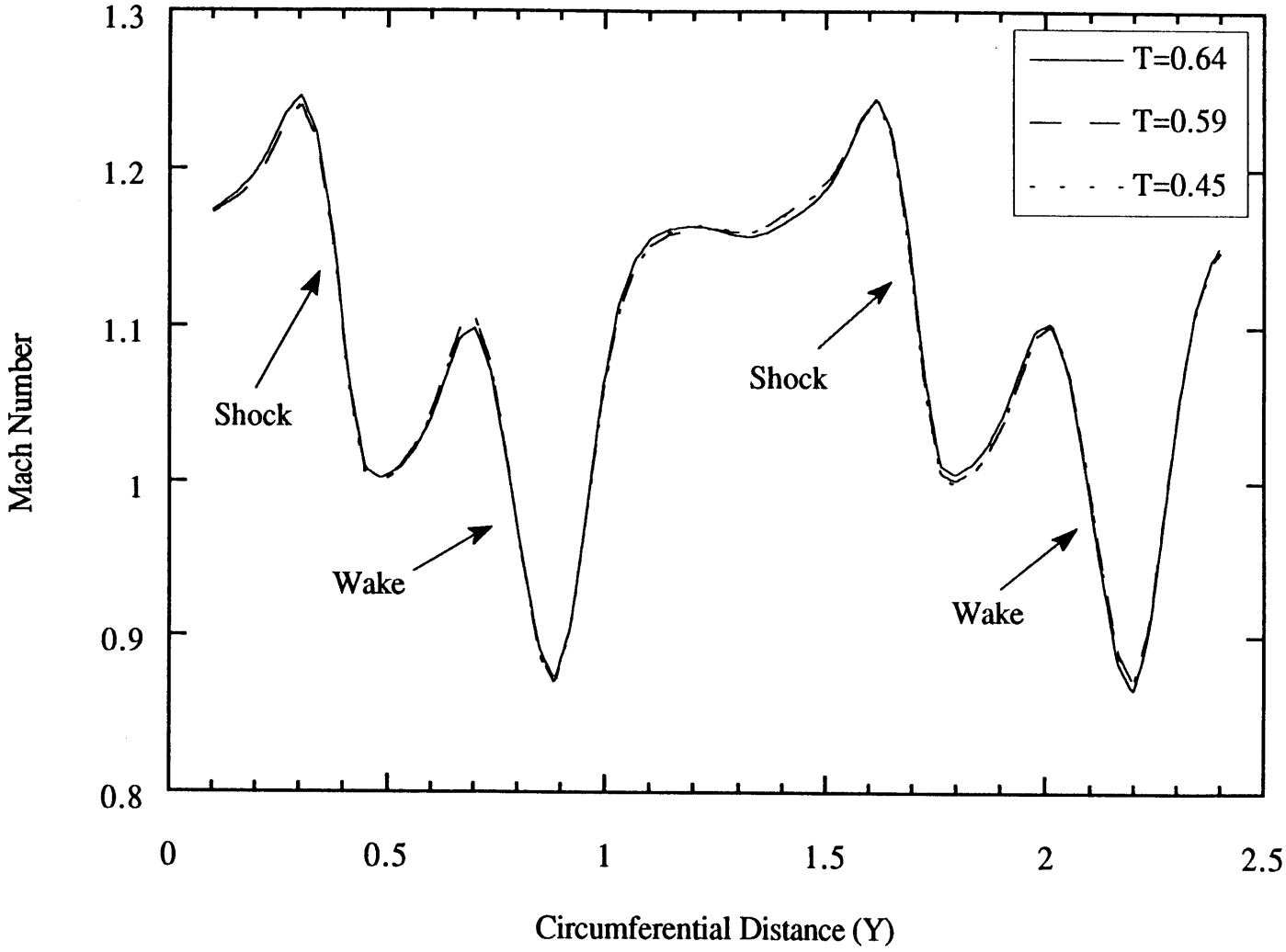

Figure (4.4) : Calculated Mach Number Versus Circumferential Distance at X=1.17

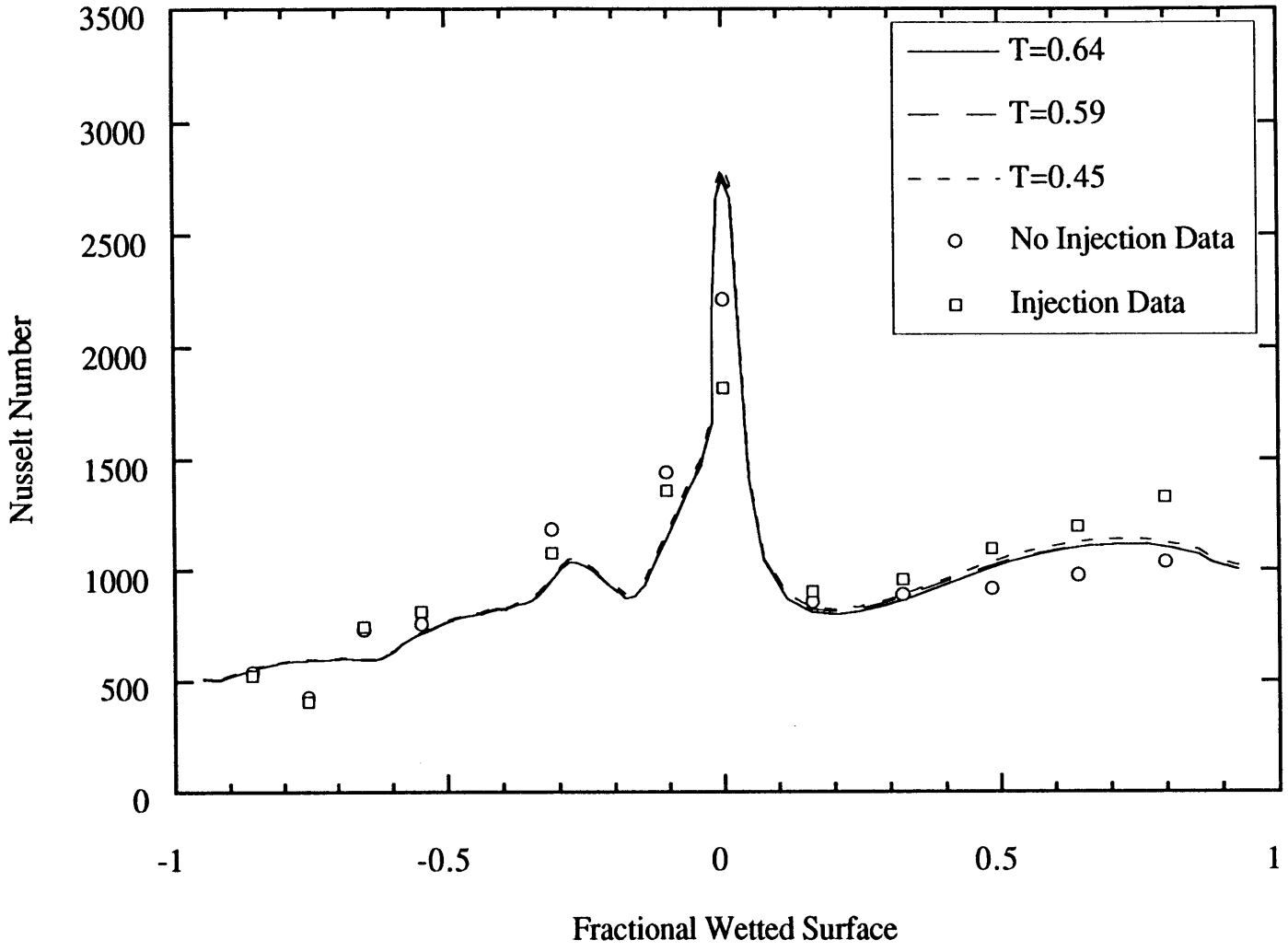

Figure (4.5) : Averaged Unsteady Nusselt Number Versus Fractional Wetted Surface for Three NGV Blade Temperatures

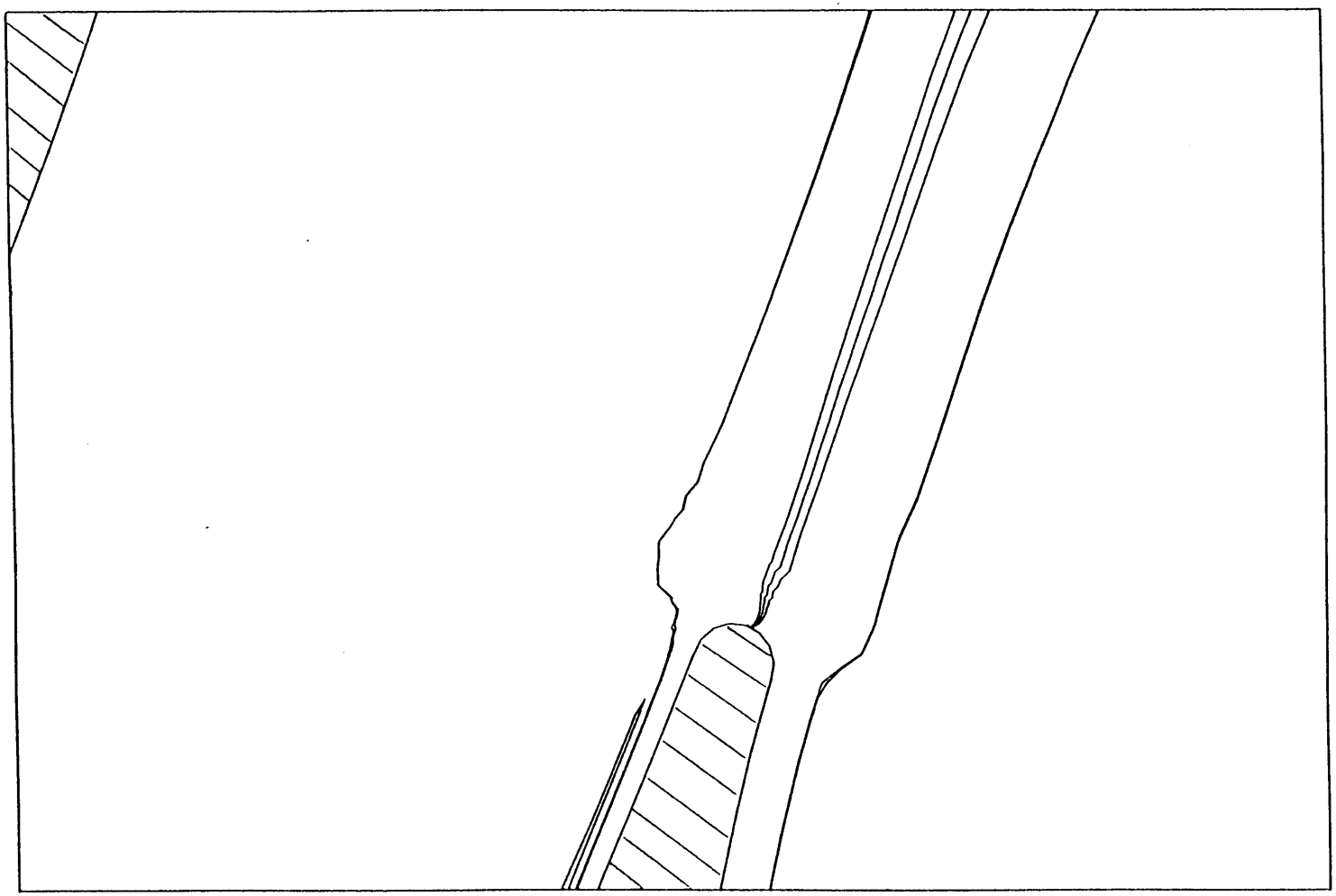

Figure (4.6) : Contour Plot of UNSFLO Calculated Vorticity at an Instant in Time With No Injection for Three NGV Blade Temperatures

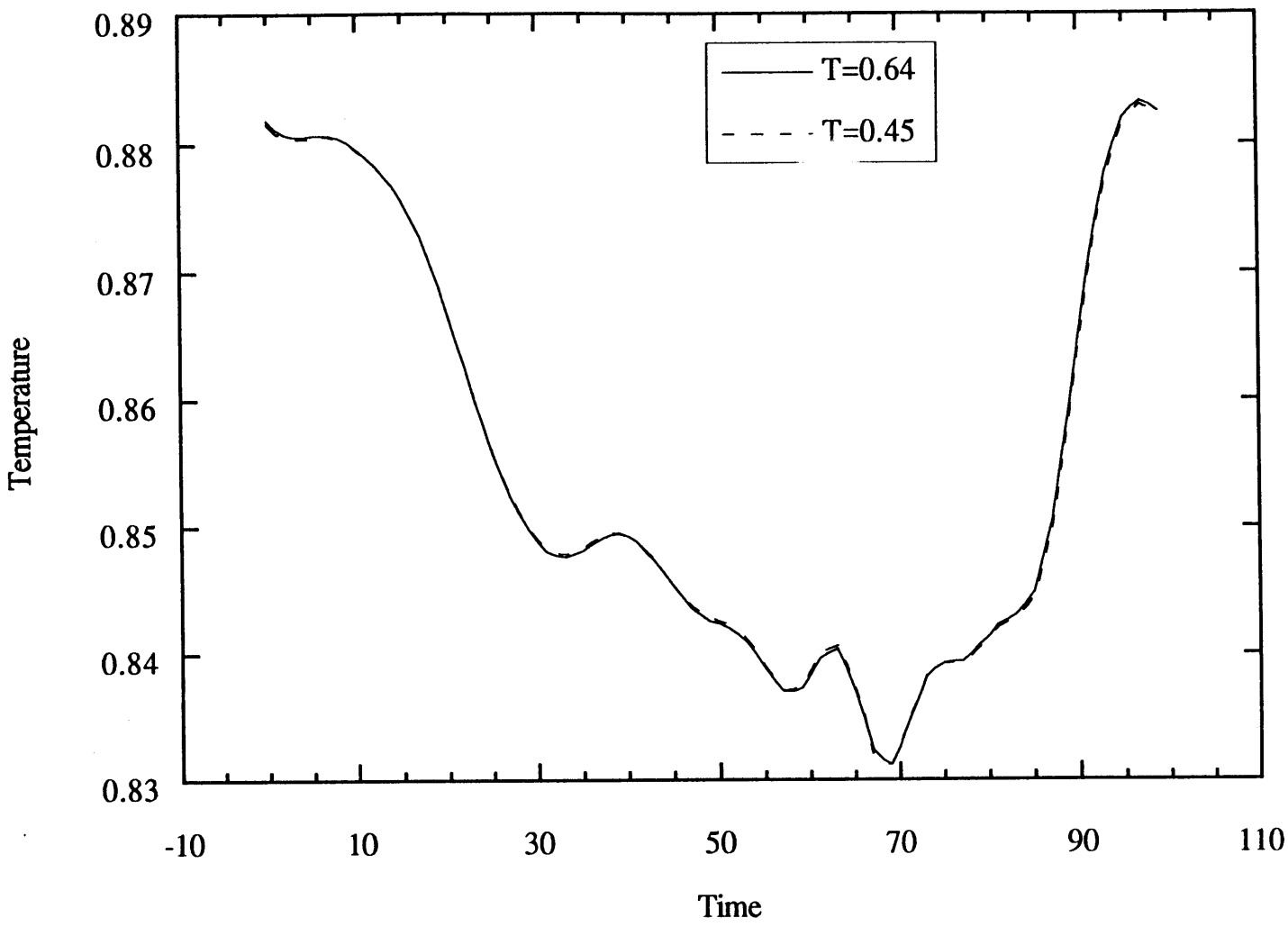

Figure (4.7) : Static Temperature Versus Time at the Boundary Layer Edge of Gauge 2 for Two NGV Blade Temperatures

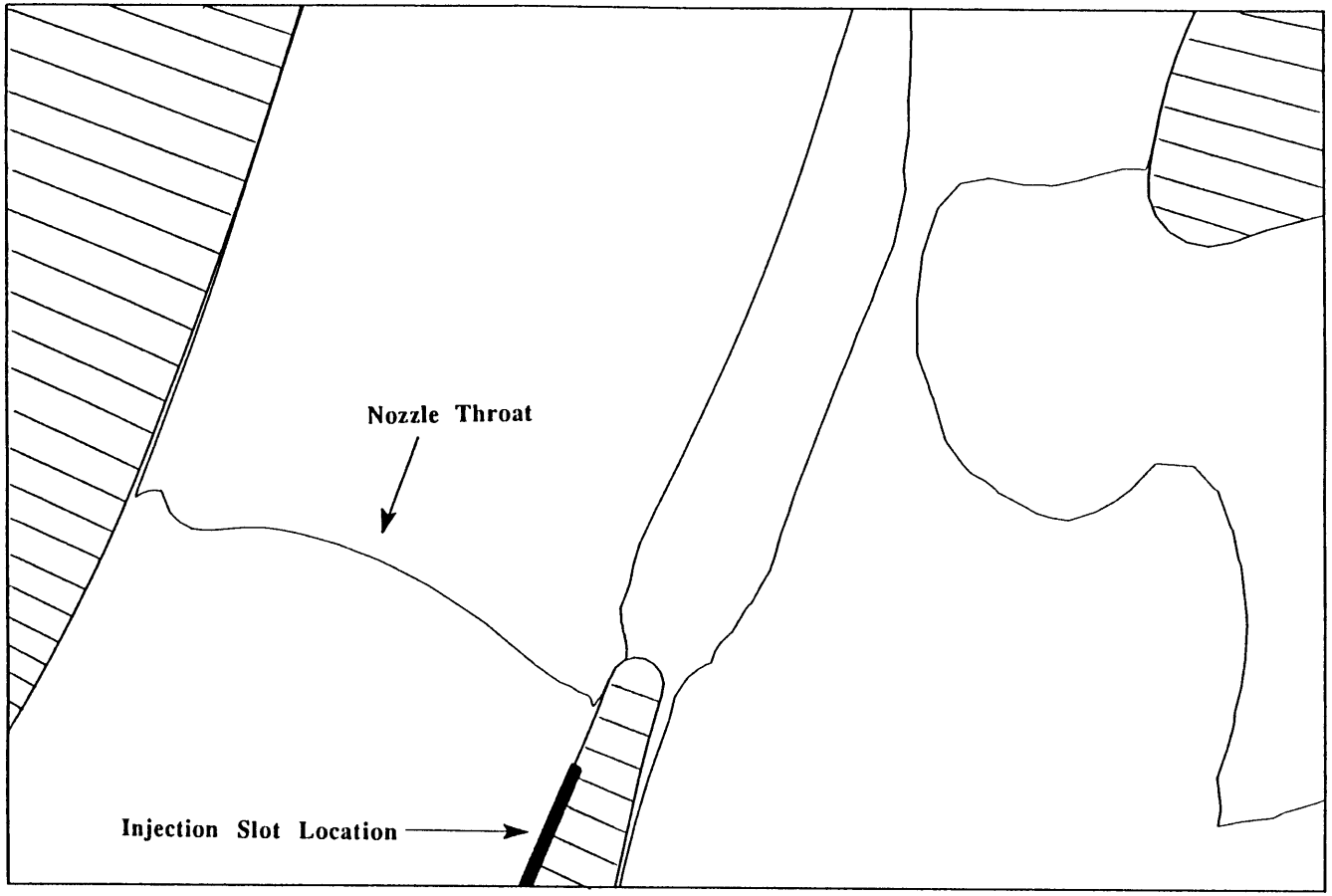

Figure (4.8) Contour Plot of UNSFLO Calculated Mach Number at an Instant in Time with Coolant Injection

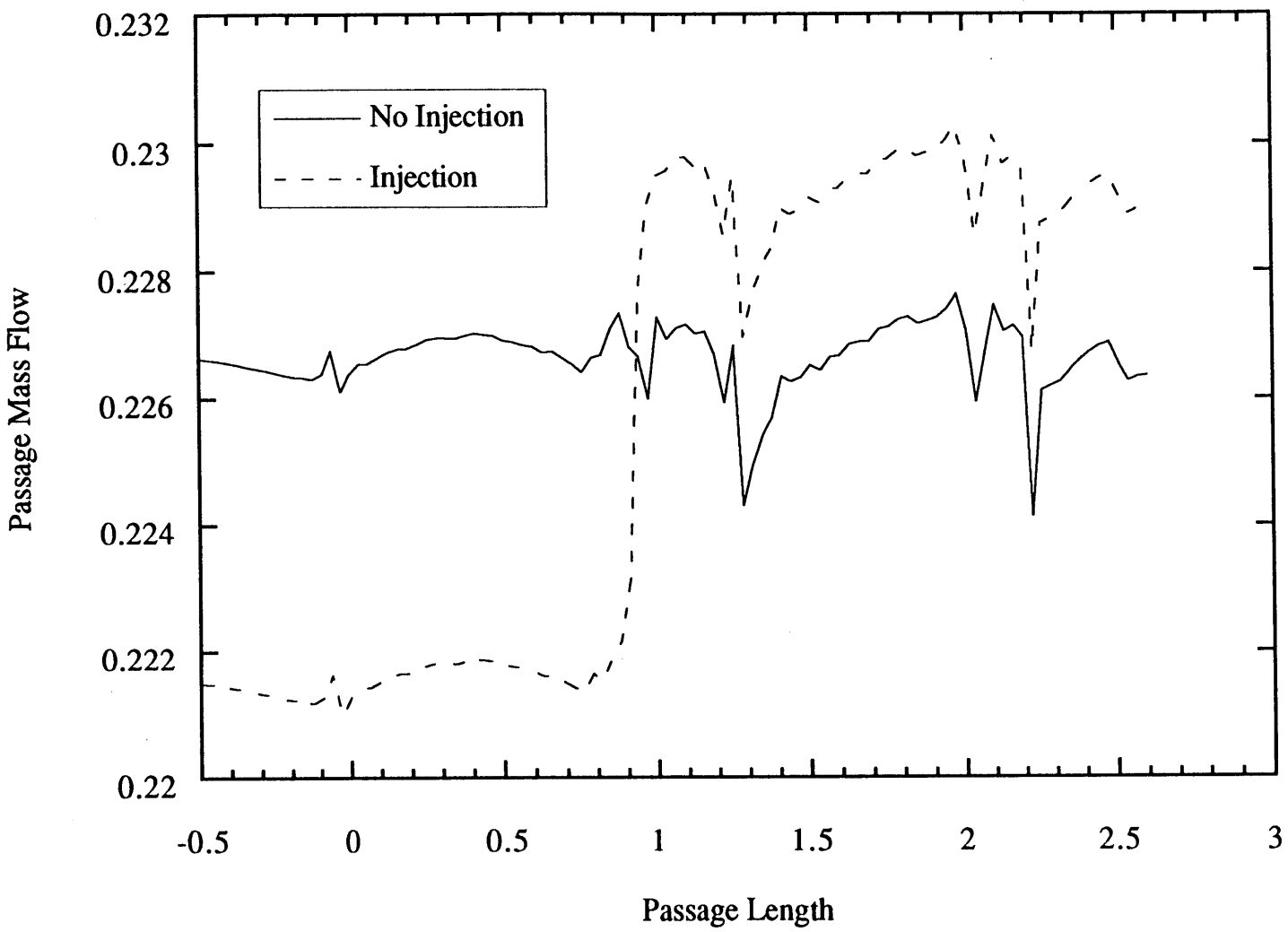

Figure (4.9) : Passage Length Versus Passage Mass Flow

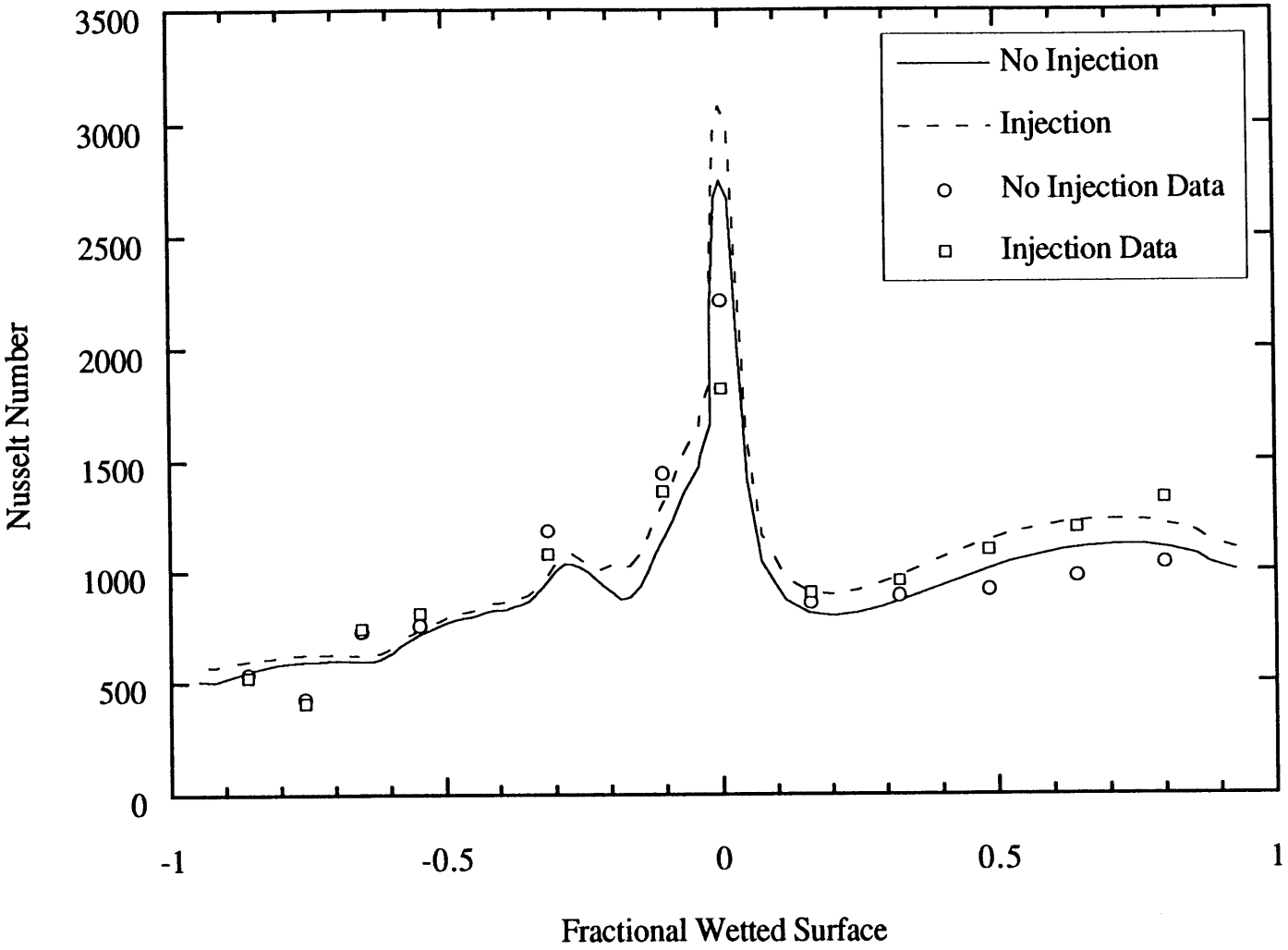

Figure (4.10) Averaged Unsteady Nusselt Number Versus Fractional Wetted Surface for Injection and No Injection Cases

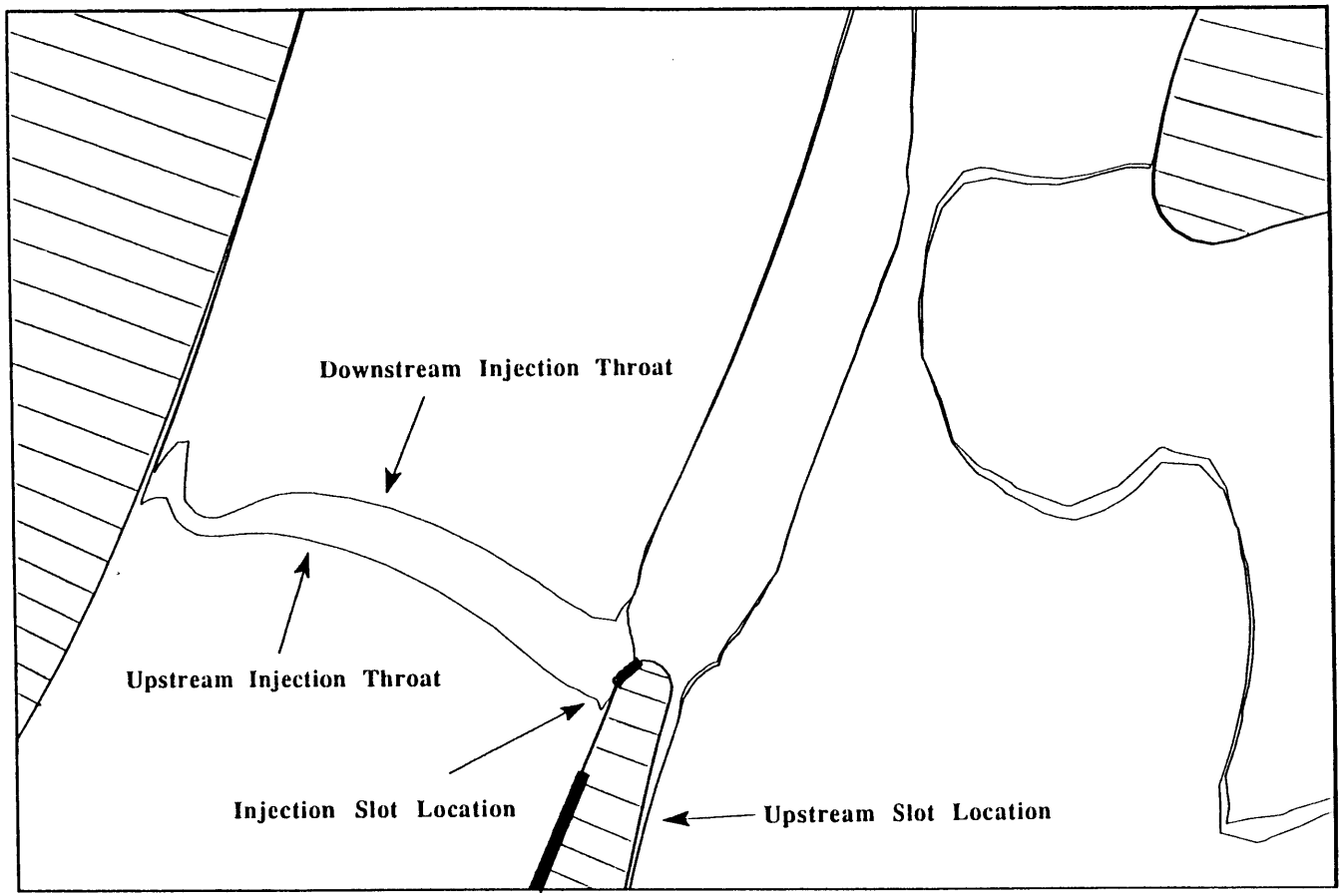

Figure (4.11) Contour Plot of UNSFLO Calculated Mach Number at an Instant in Time with Coolant Injection for Upstream and Downstream Injection

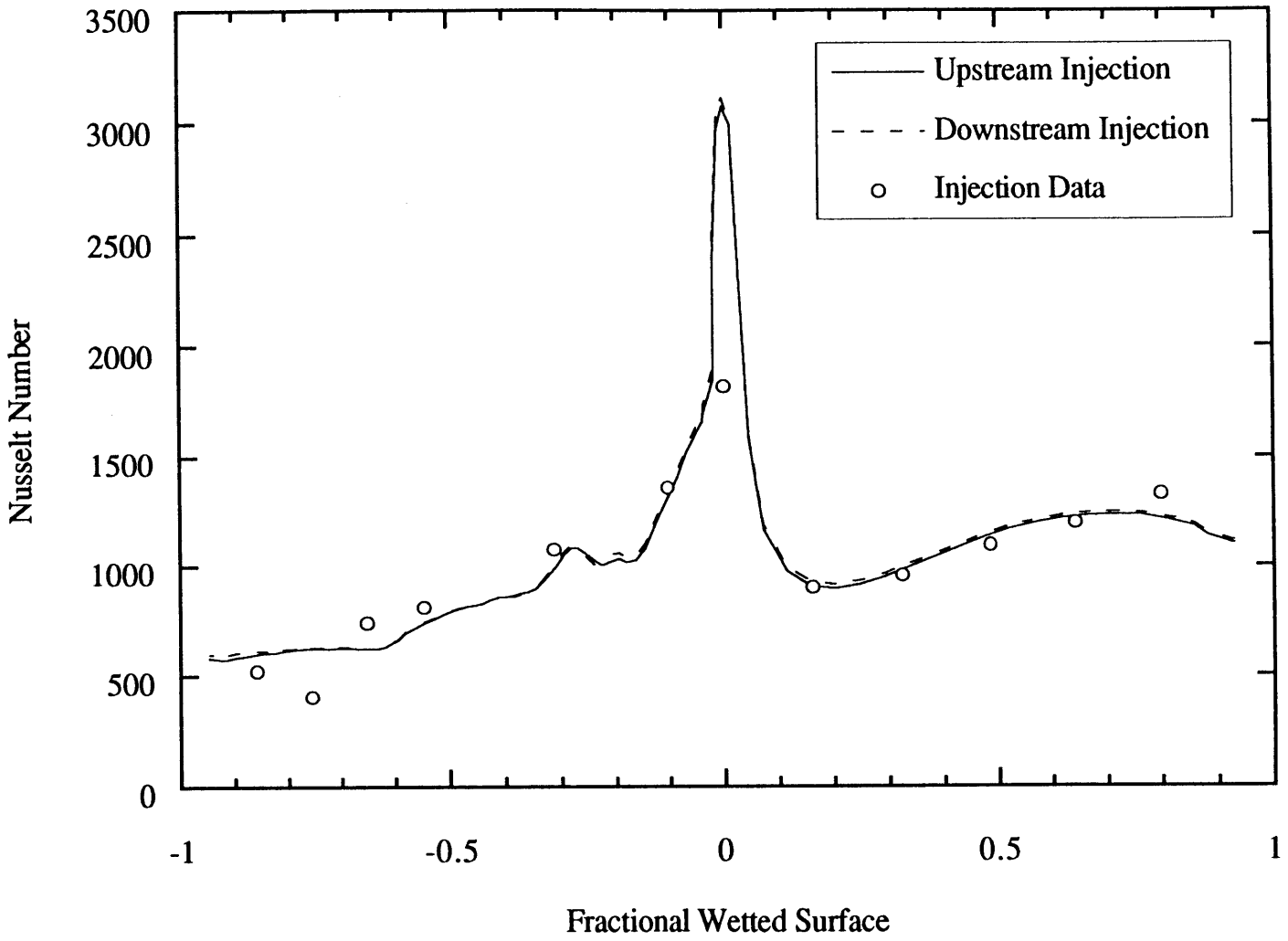

Figure (4.12) : Averaged Unsteady Nusselt Number Versus Fractional Wetted Surface for Coolant Injection Upstream and Downstream of Nozzle Choke Location

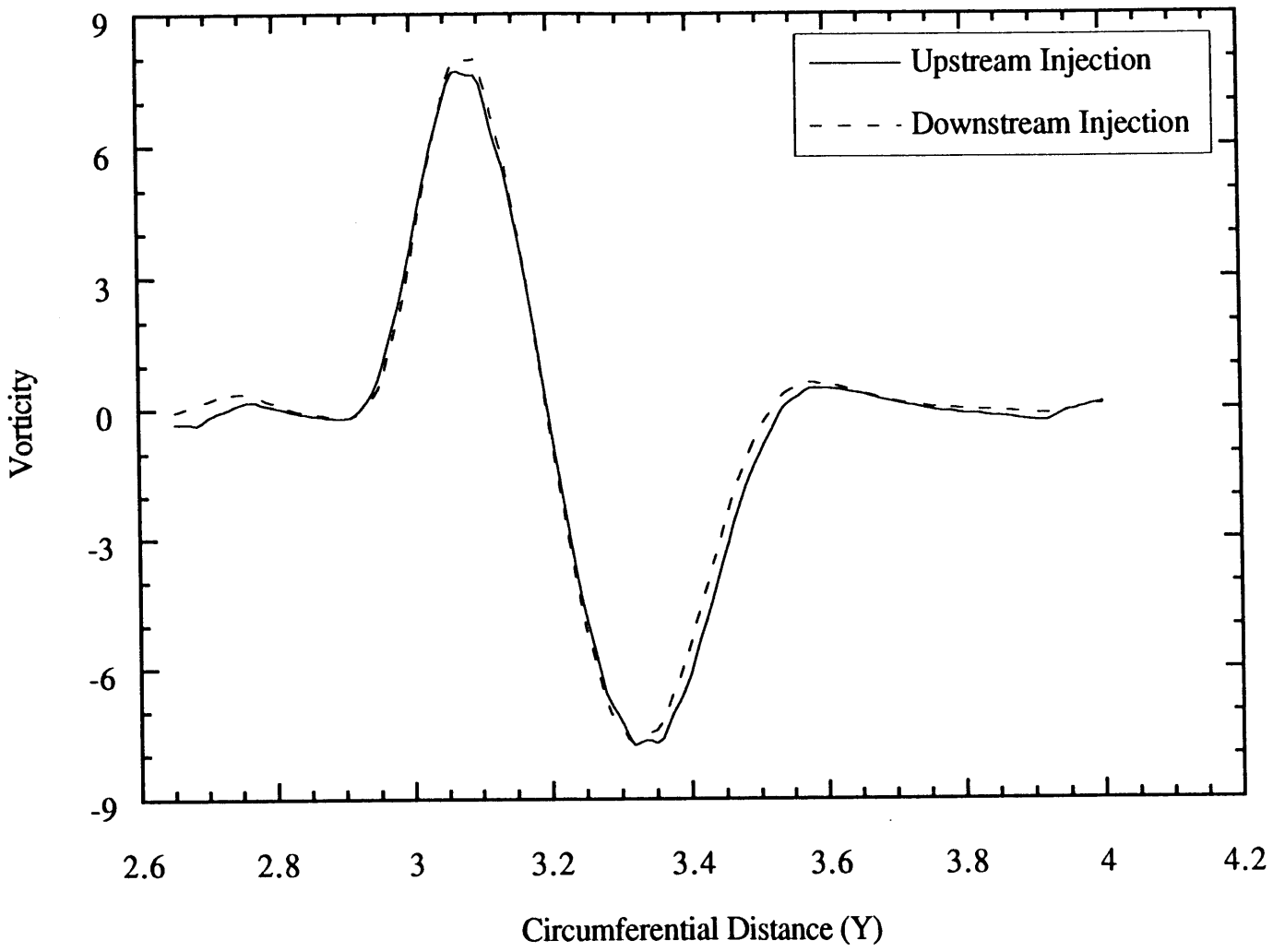

Figure (4.13) : Line Probe of Averaged Unsteady Vorticity Versus Circumferential Distance for the Upstream and Downstream Injection Locations at (X=1.17)

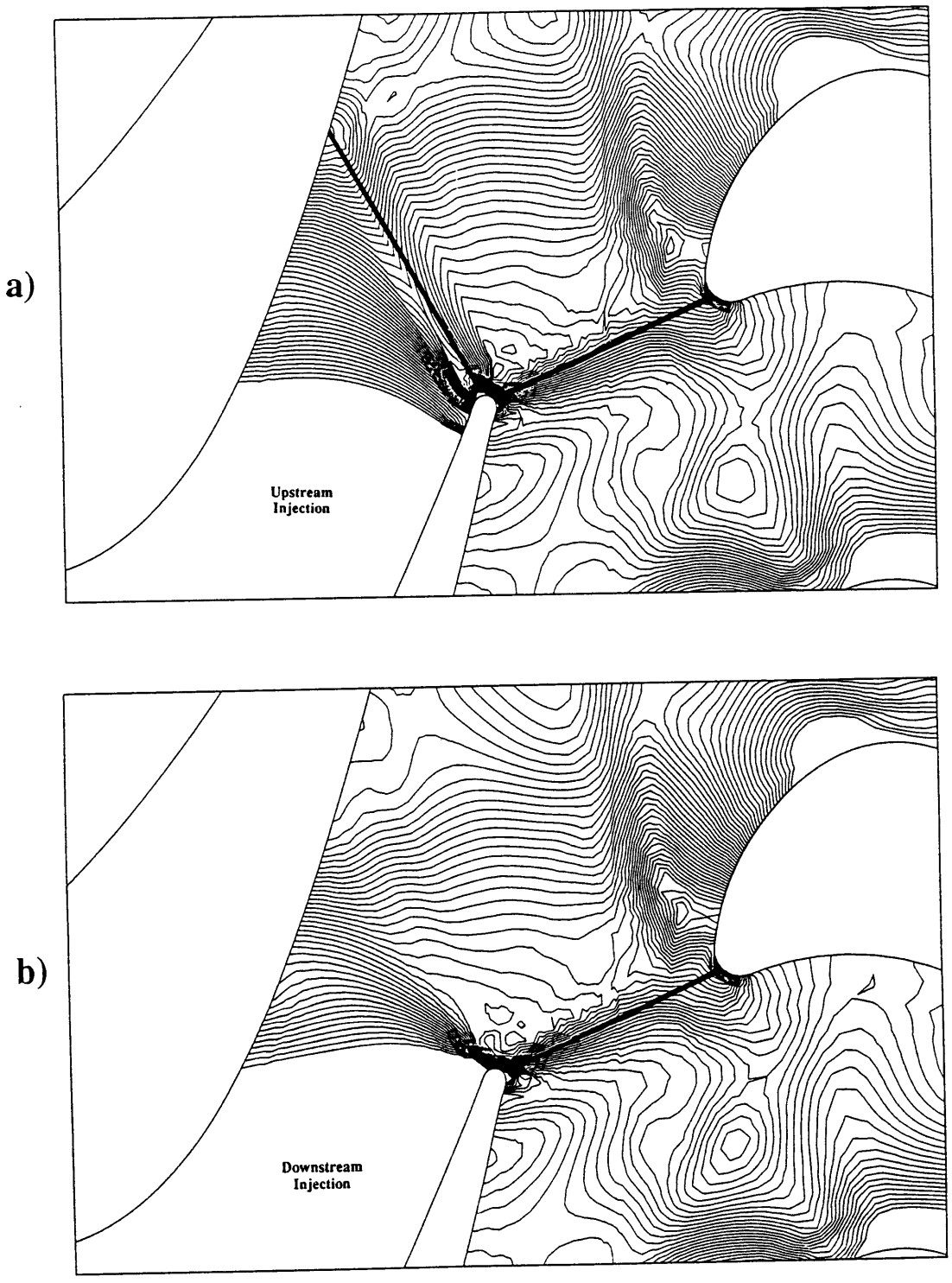

Figure (4.14) : Contour Plots of UNSFLO Calculated Static Pressure at an Instant in Time For Upstream and Downstream Injection

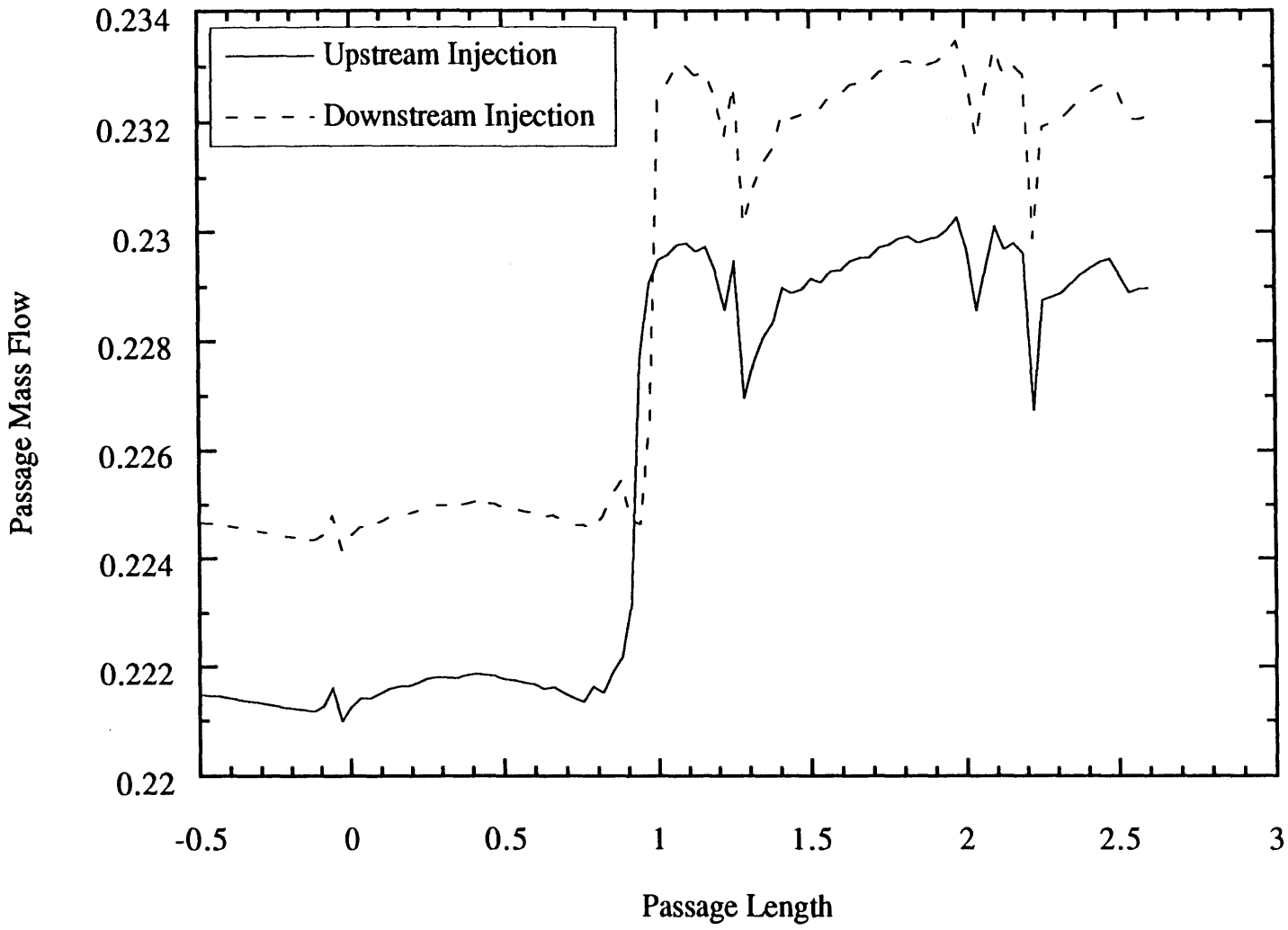

Figure (4.15) : Passage Length Versus Passage Mass Flow

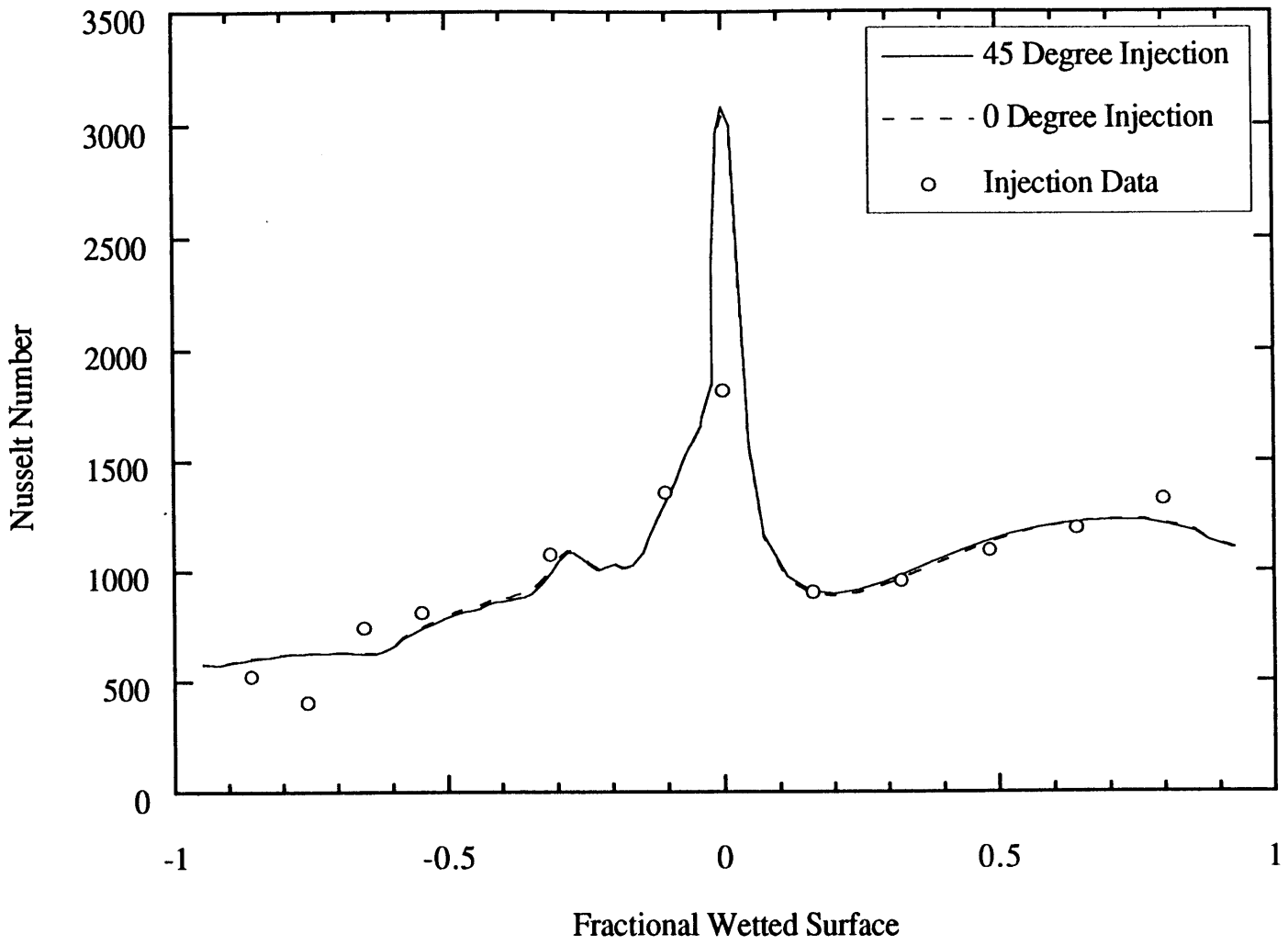

Figure (4.16) : Averaged Unsteady Nusselt Number Versus Fractional Wetted Surface for Two Injection Angles

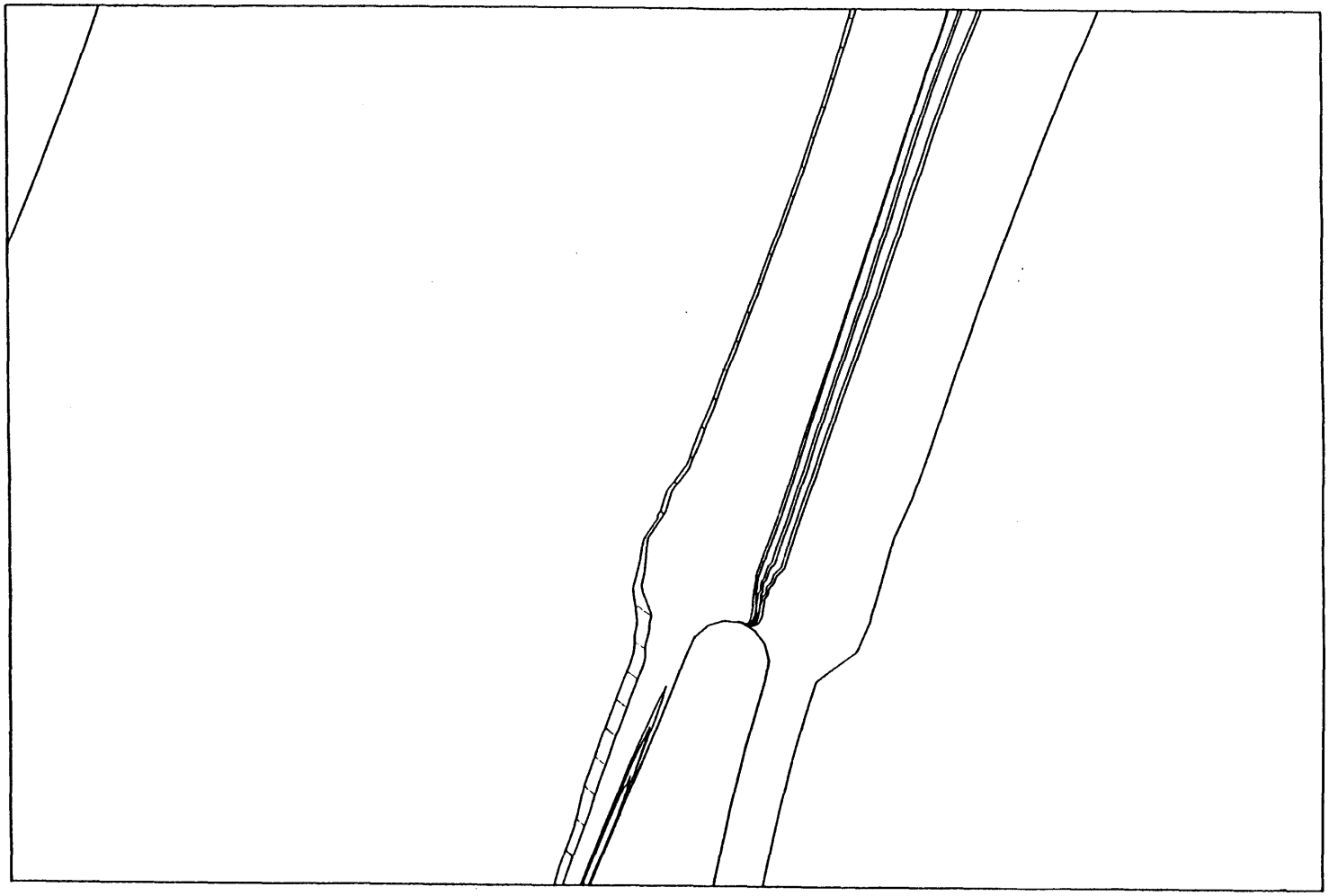

Figure (4.17) : Contour Plot of UNSFLO Calculated Vorticity at an Instant in Time With Injection for 0 and 45 Degree Injection Angles

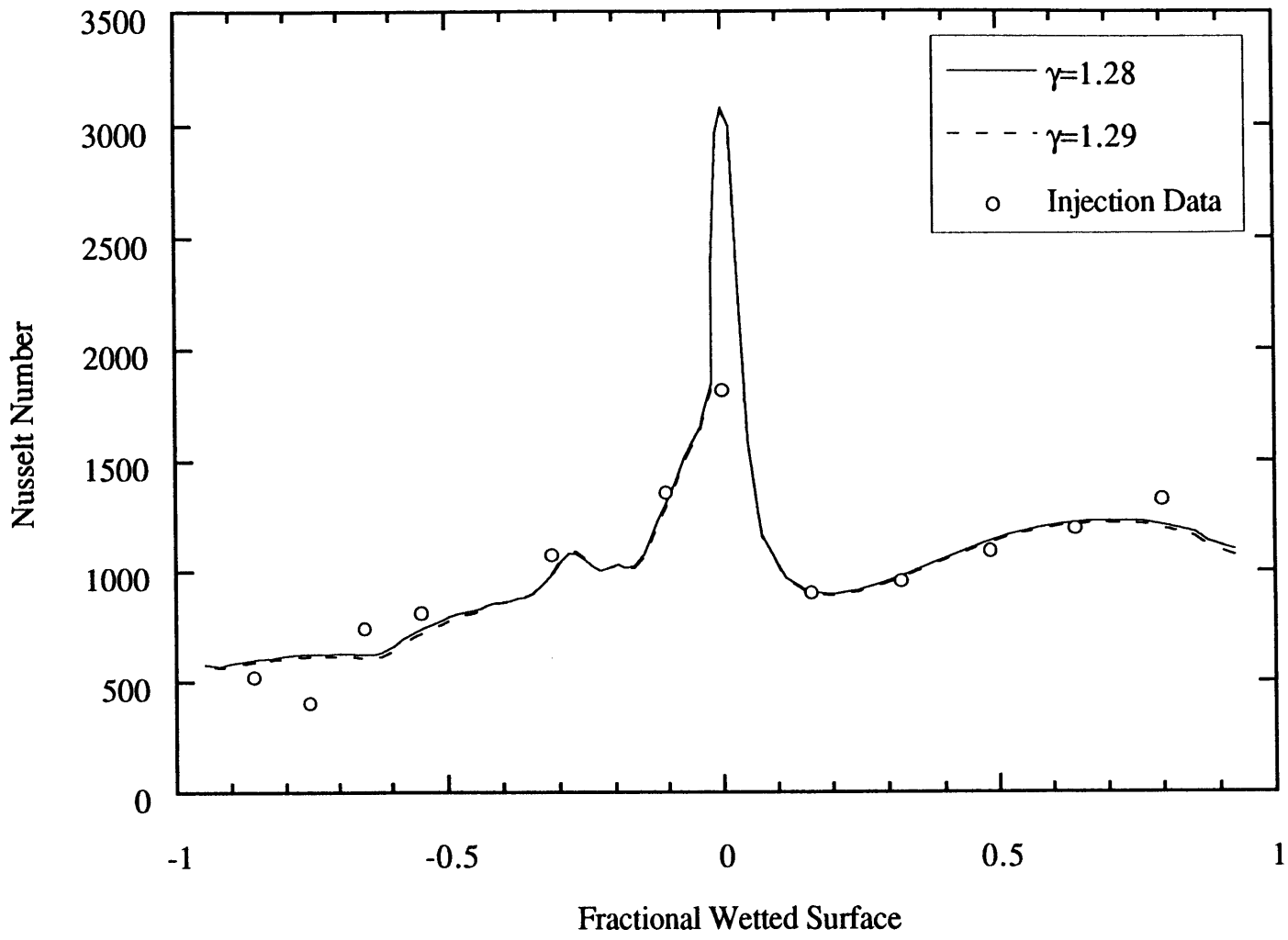

Figure (4.18) : Averaged Unsteady Nusselt Number Versus Fractional Wetted Surface for Two Ratios of Specific Heats

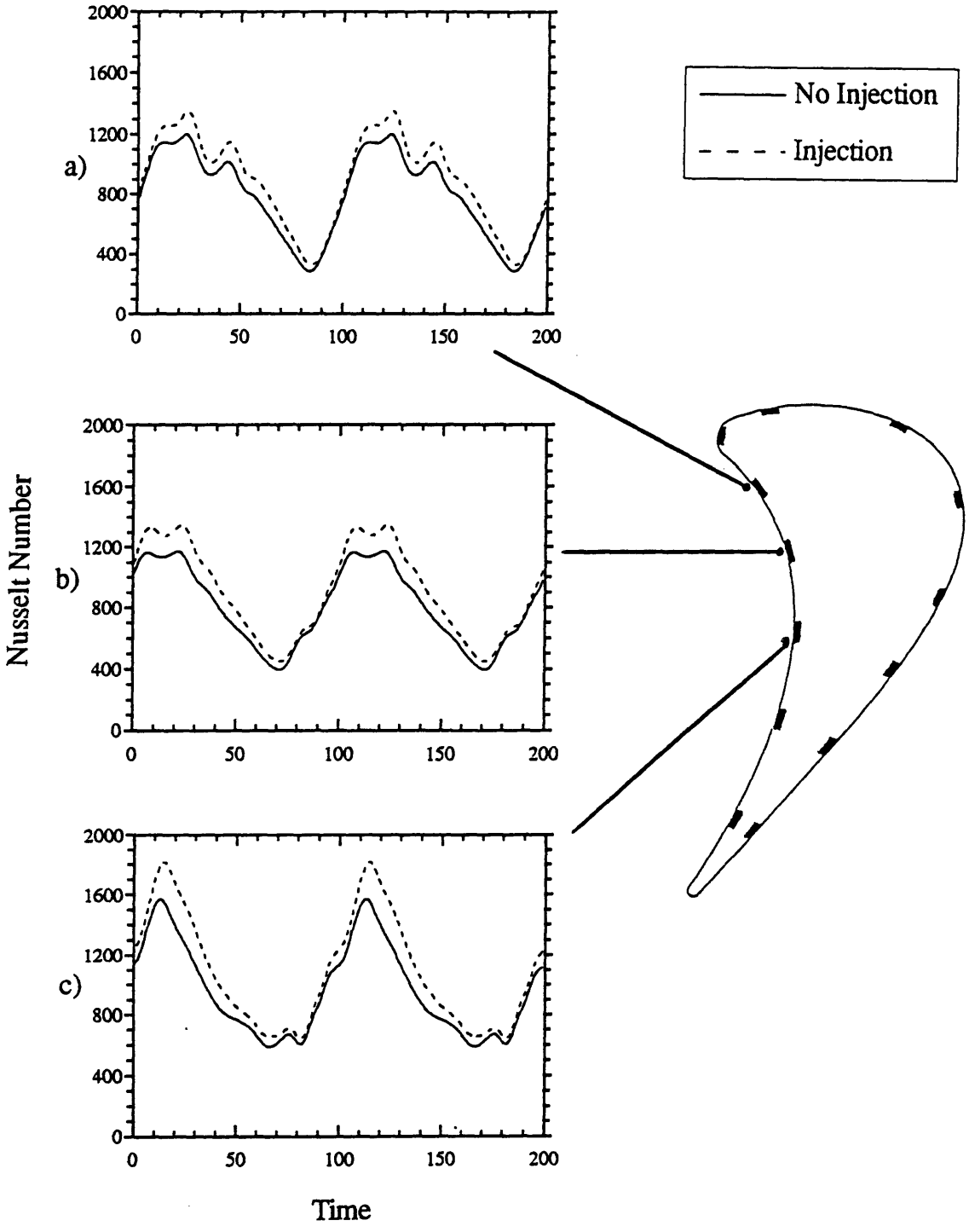

Figure (4.19) : UNSFLO Calculated Time Histories of Nusselt Number at the Five Gauge Locations on the Pressure Surface for the No Injection and Injection Cases

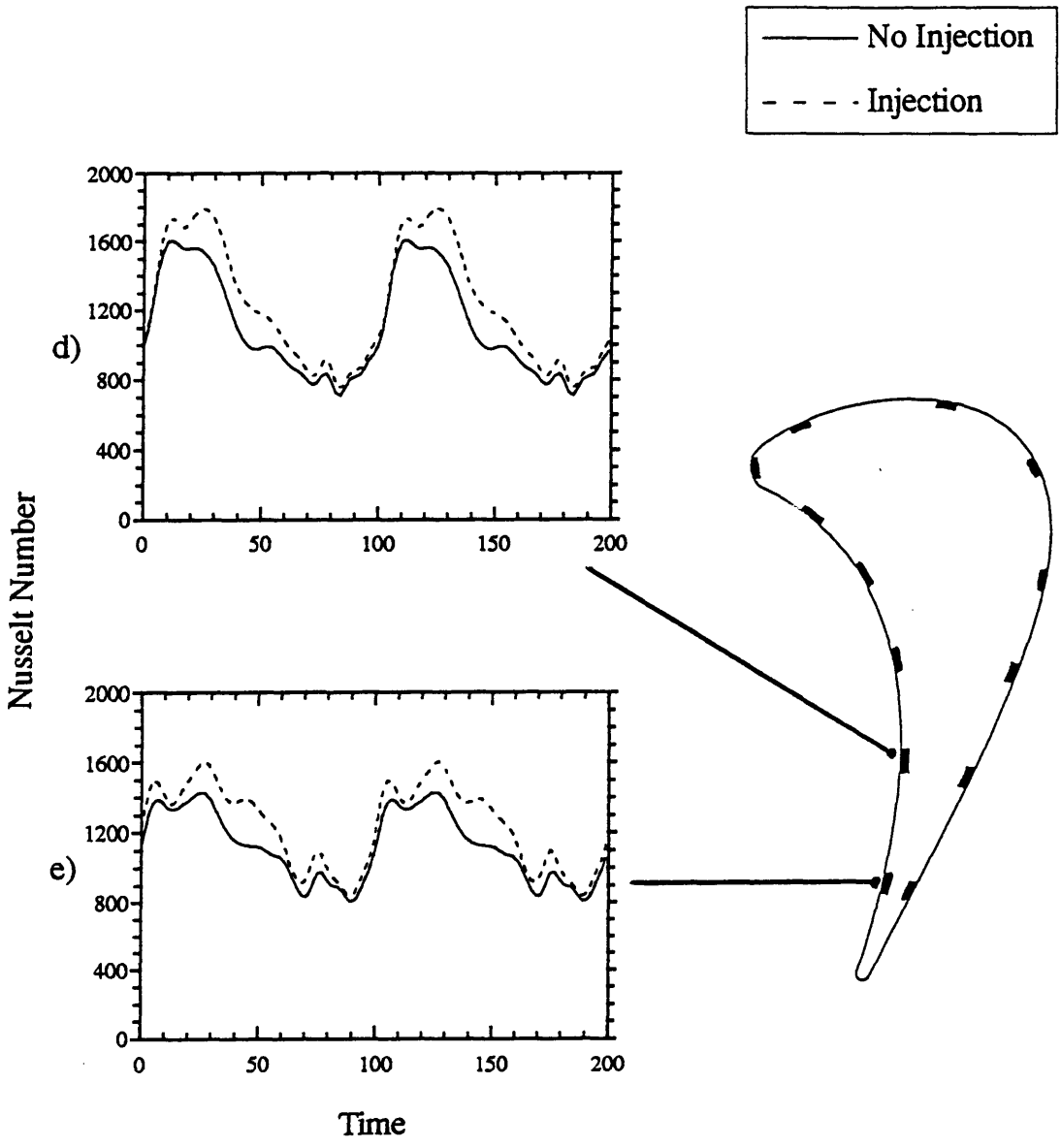

Figure (4.19) : Continued; UNSFLO Calculated Time Histories of Nusselt Number at the Five Gauge Locations on the Pressure Surface for the No Injection and Injection Cases

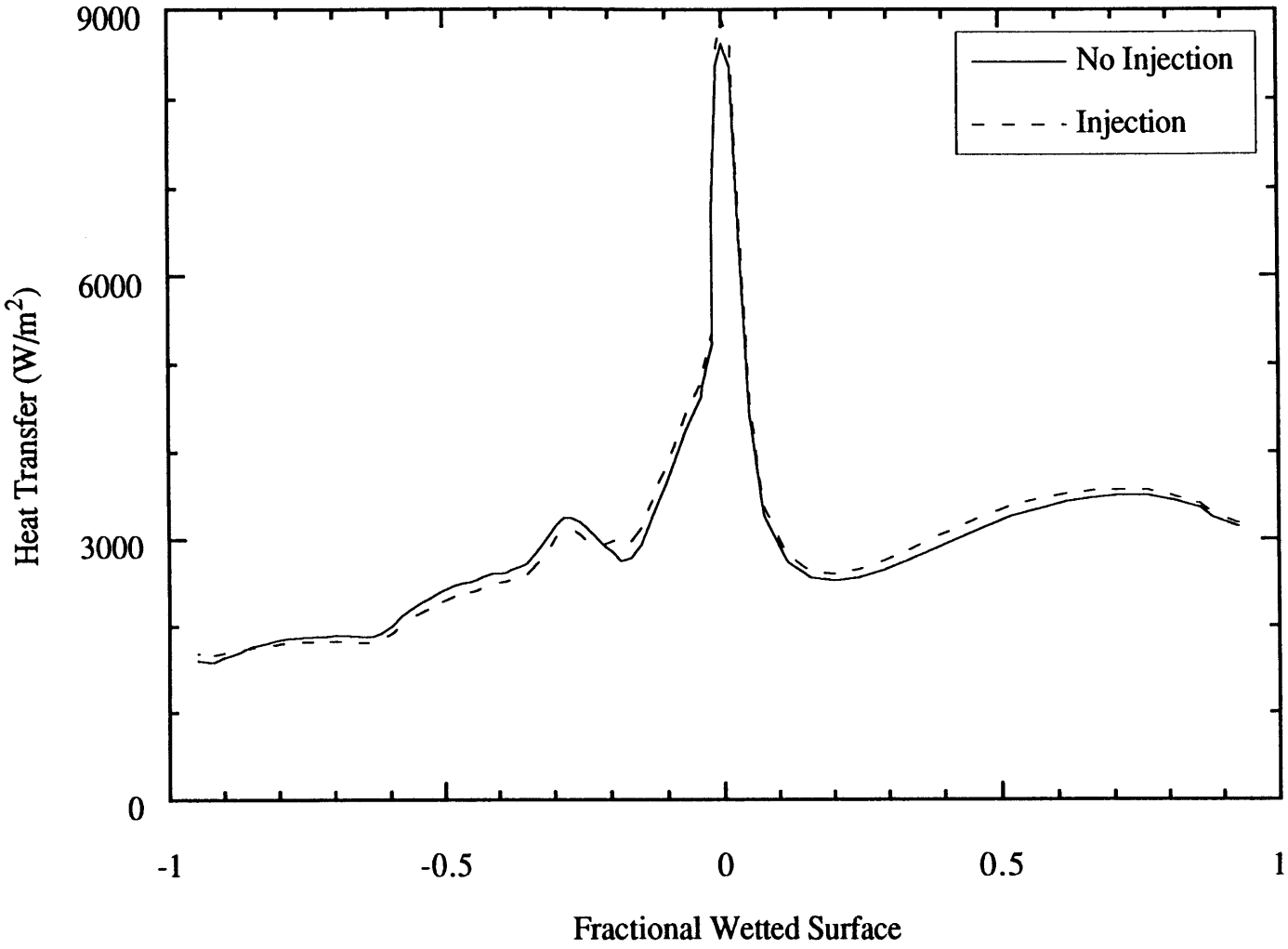

Figure (4.20) : Averaged Unsteady Heat Transfer Versus Fractional Wetted Surface for Injection and No Injection Cases

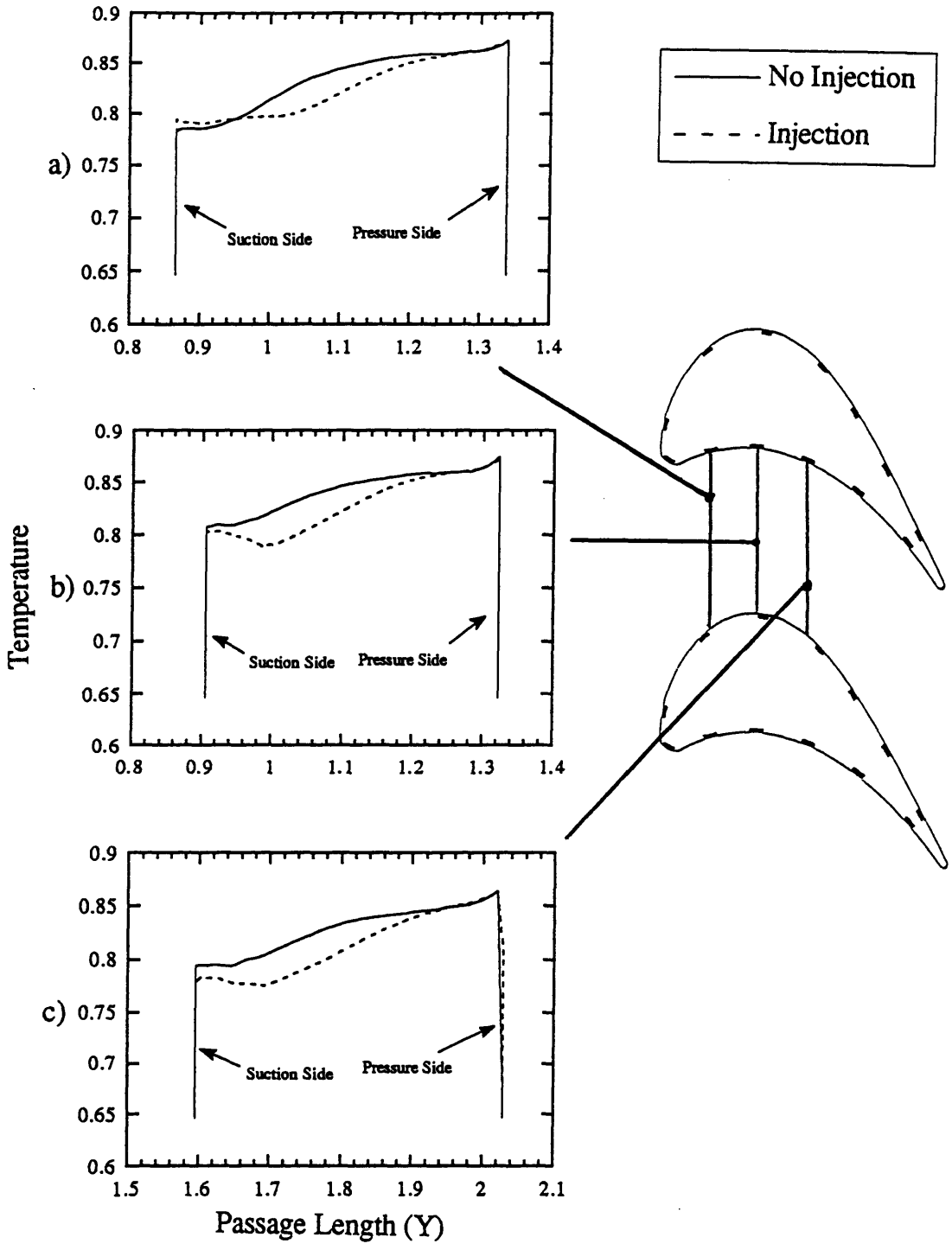

Figure (4.21) : Unsteady Averaged UNSFLO Calculated Static Temperature Versus Circumferential Distance at the Five Gauge Locations on the Pressure Surface

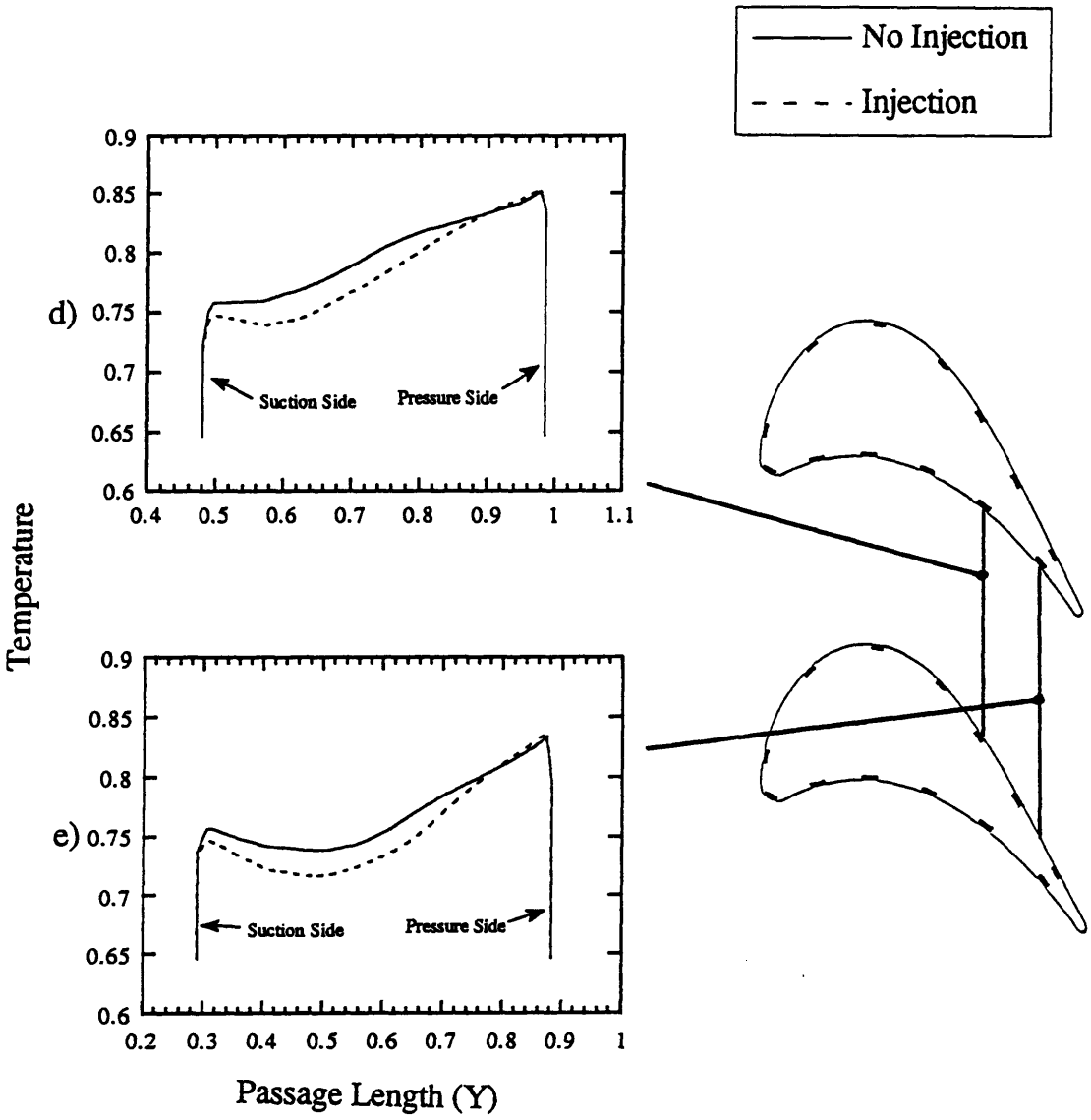

Figure (4.21) : Continued; Unsteady Averaged UNSFLO Calculated Static Temperature Versus Circumferential Distance at the Five Gauge Locations on the Pressure Surface

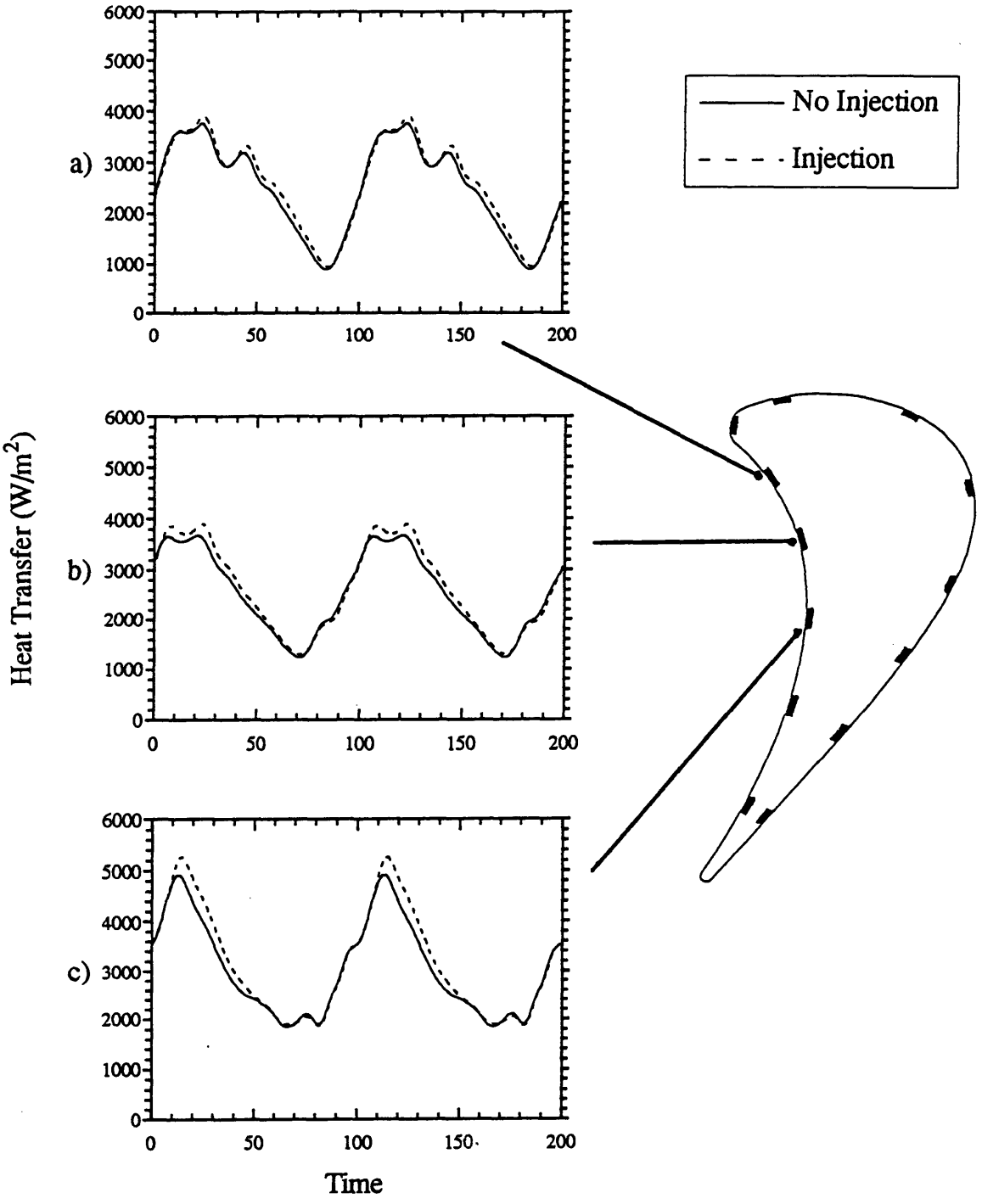

Figure (4.22) : UNSFLO Calculated Time Histories of Heat Transfer at the Five Gauge Locations on the Pressure Surface for the No Injection and Injection Cases

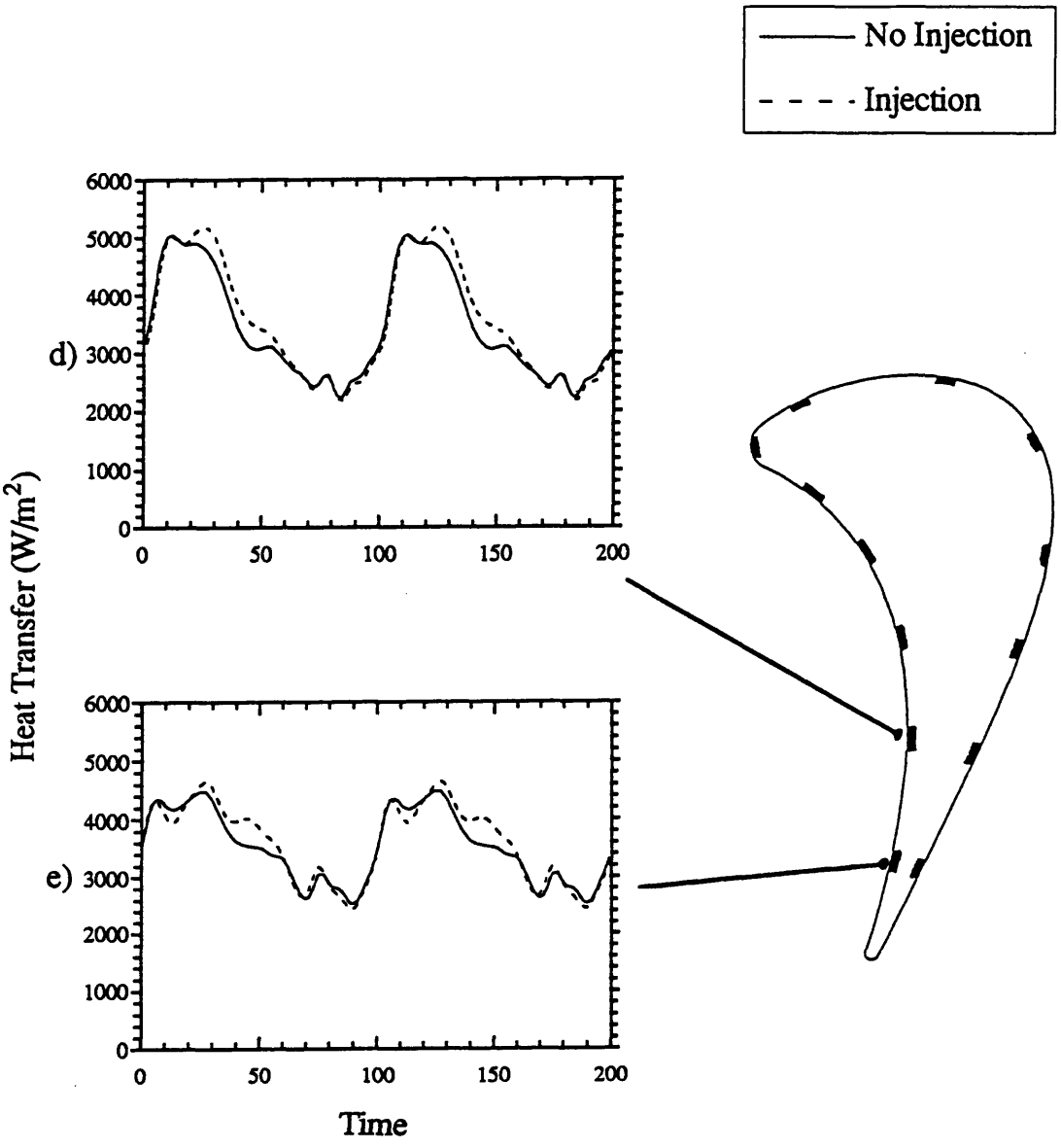

Figure (4.22) : Continued; UNSFLO Calculated Time Histories of Heat Transfer at the Five Gauge Locations on the Pressure Surface for the No Injection and Injection Cases

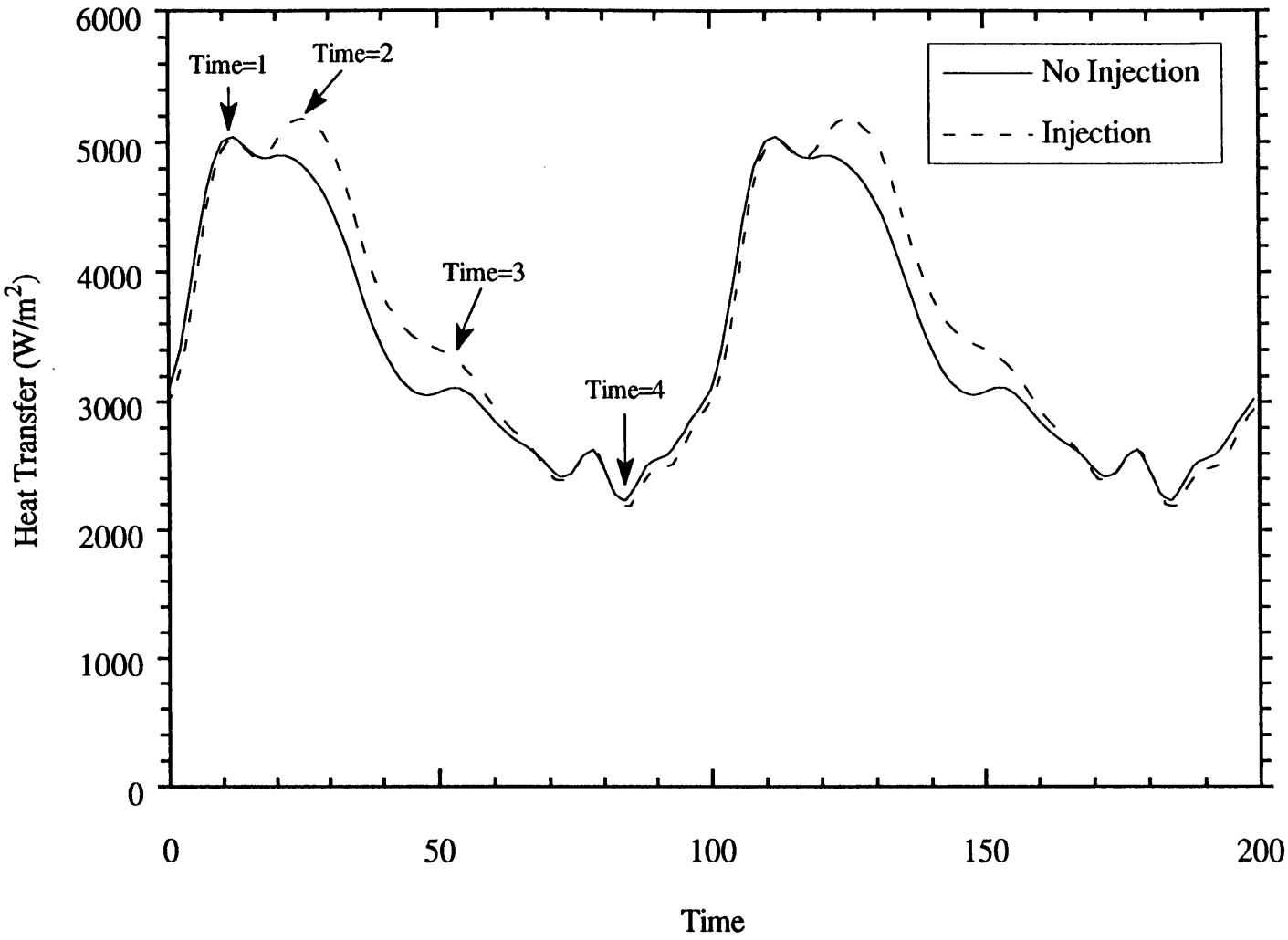

Figure (4.23) : Calculated Heat Transfer Time History at the Gauge 2 Location

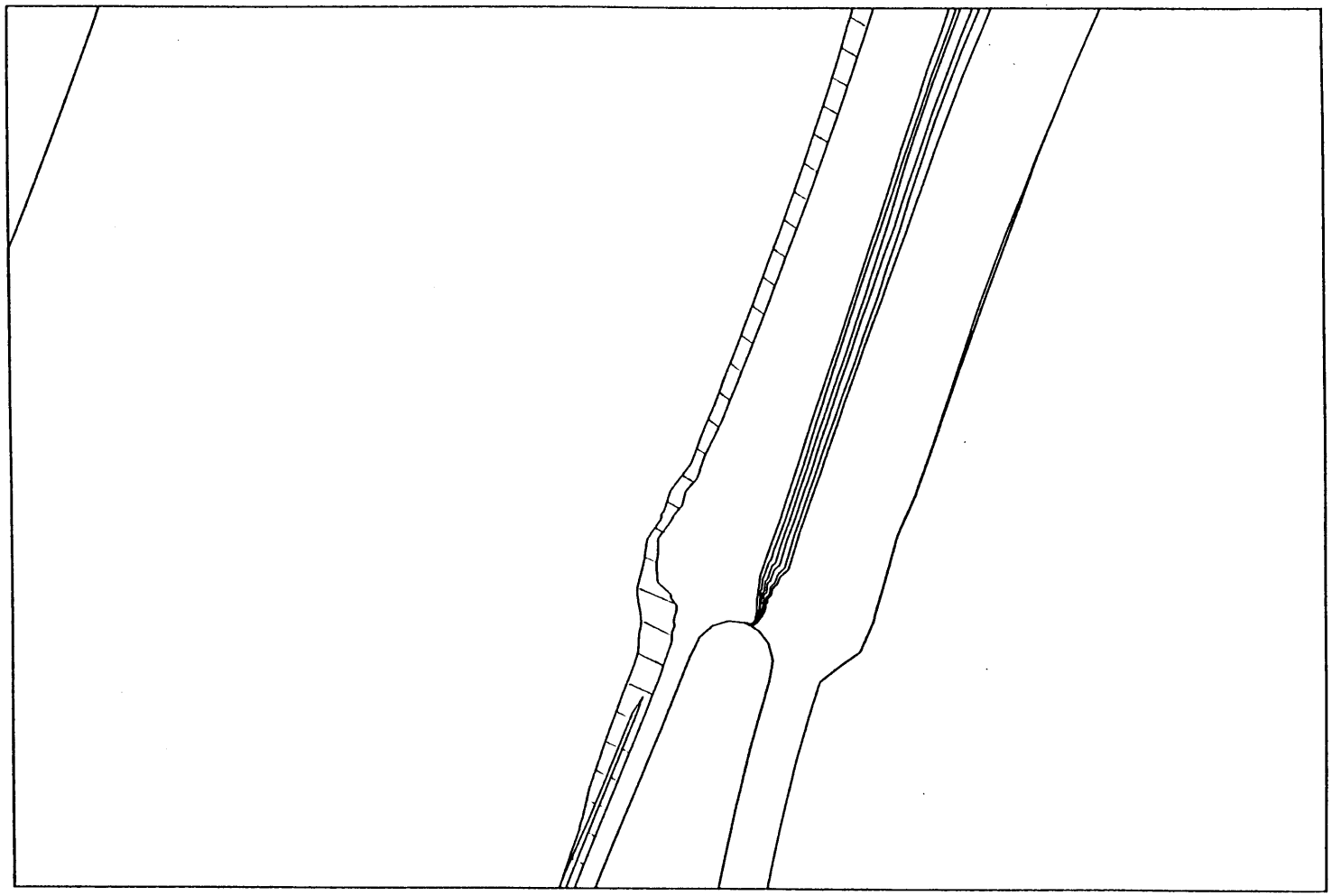

Figure (4.24) : Contour Plot of UNSFLO Calculated Vorticity at an Instant in Time for the No Injection and Injection Cases

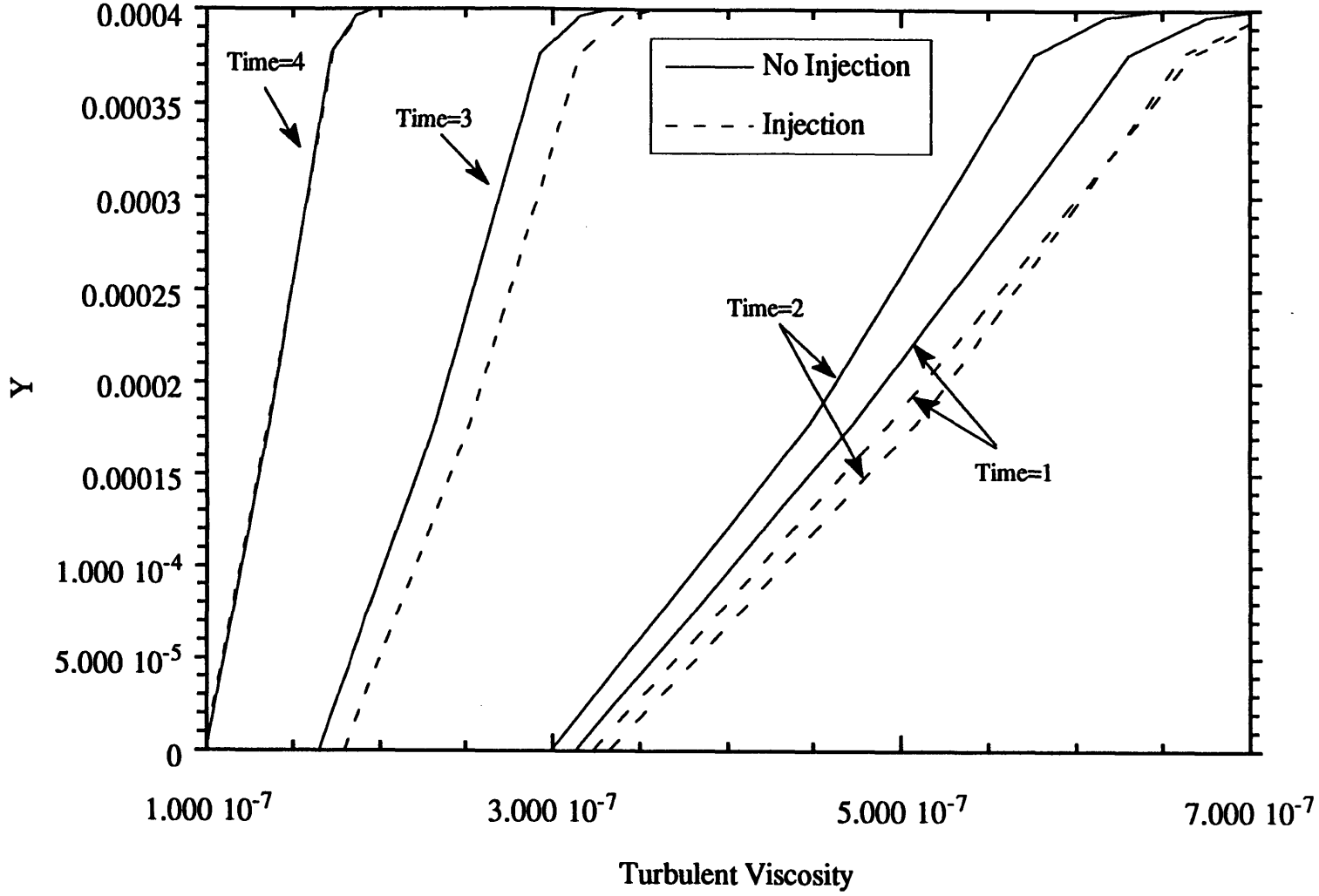

Figure (4.25) : Boundary Layer Profile of Turbulent Viscosity From the Wall to the First Grid Point Off the Wall

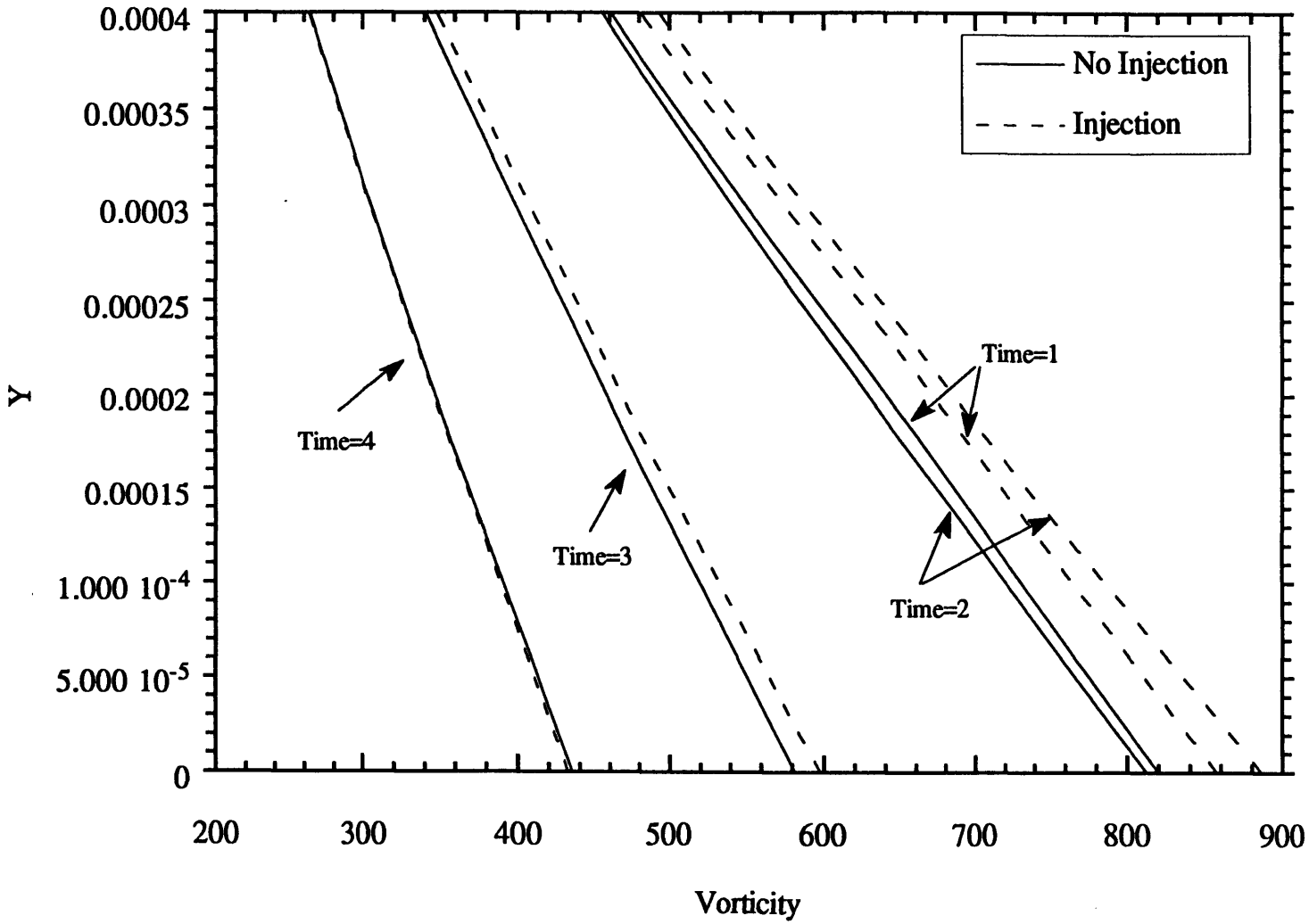

Figure (4.26) : Boundary Layer Profile of Vorticity From the Wall to the First Grid Point Off the Wall

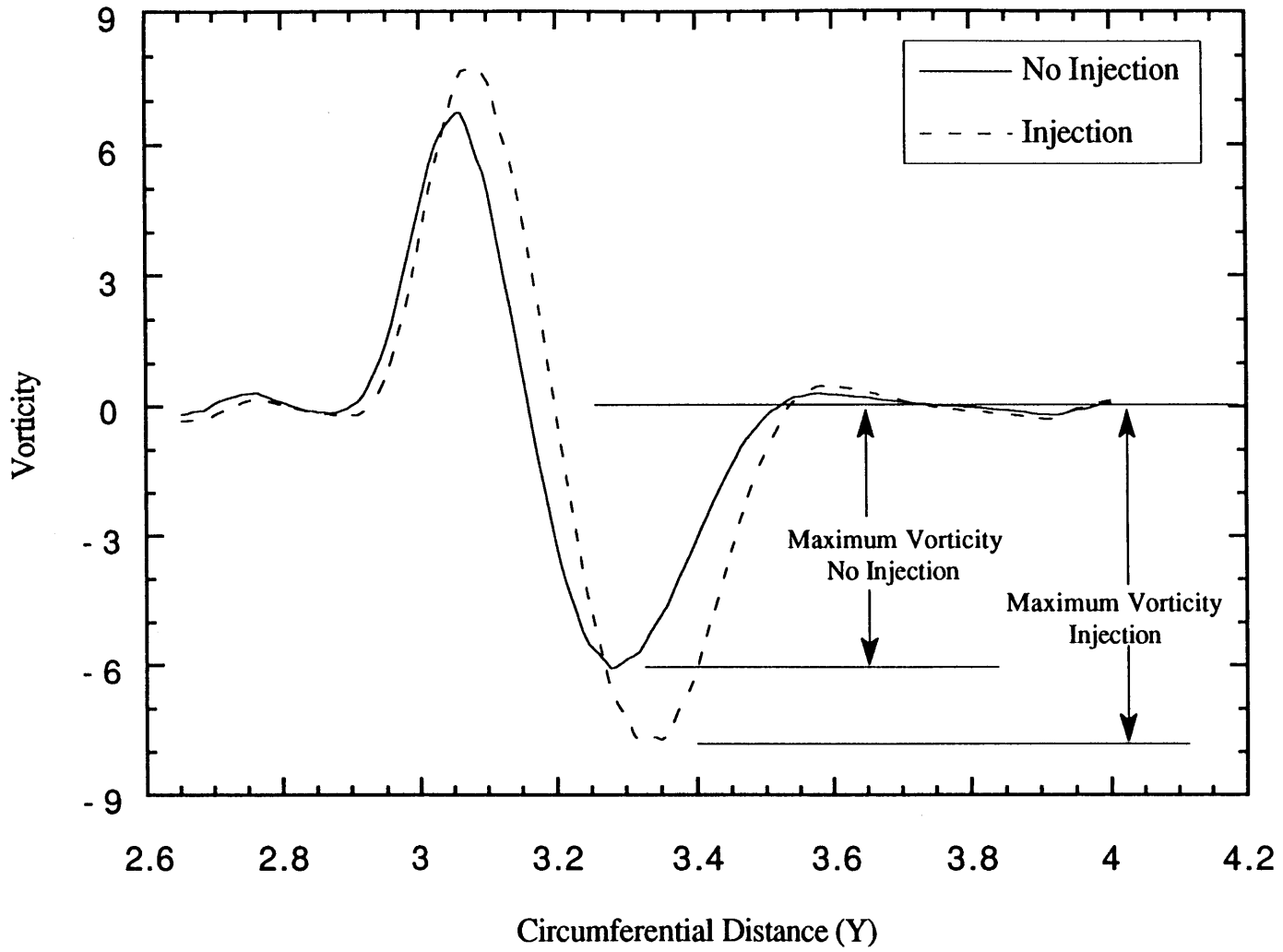

Figure (4.27) : Line Probe of Averaged Unsteady Vorticity Versus Circumferential Distance for The No Injection and Injection Cases at (X=1.17)

a)

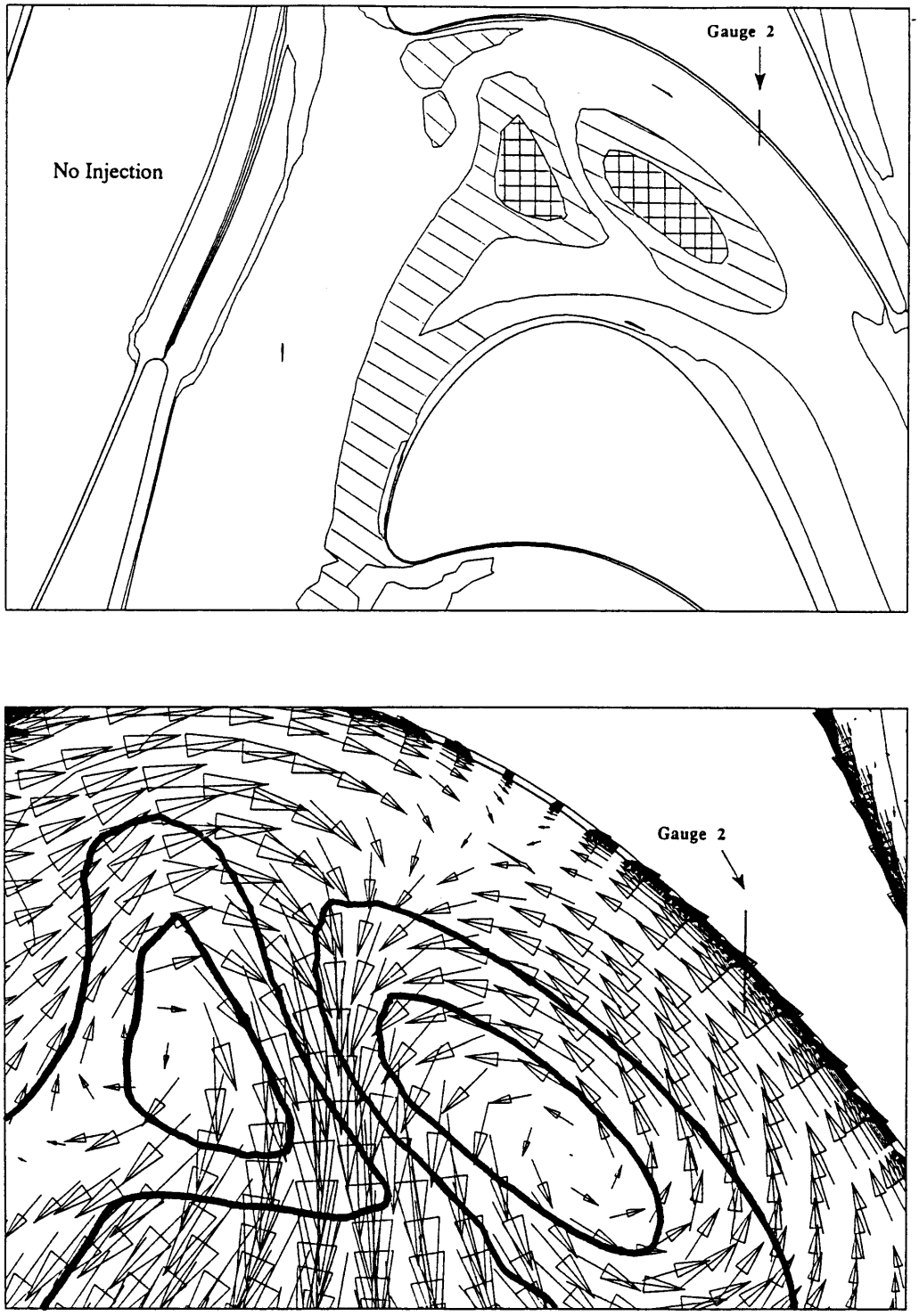

Figure (4.28a) : Contour Plots of UNSFLO Calculated Vorticity and Unsteady Velocity Vectors for the No Injection Case at Time=1

b)

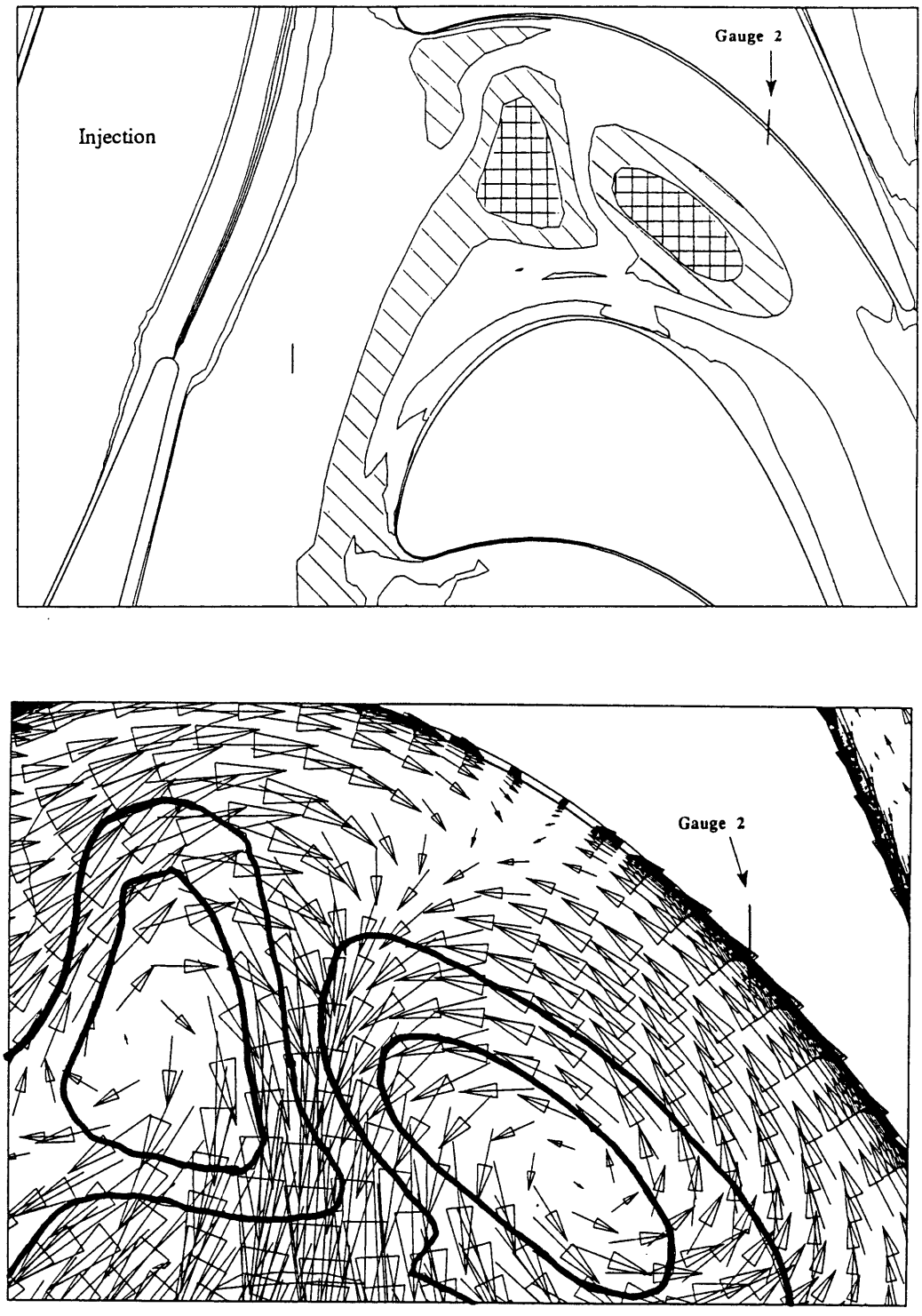

Figure (4.28b) : Contour Plots of UNSFLO Calculated Vorticity and Unsteady Velocity Vectors for the Injection Case at Time=1

a)

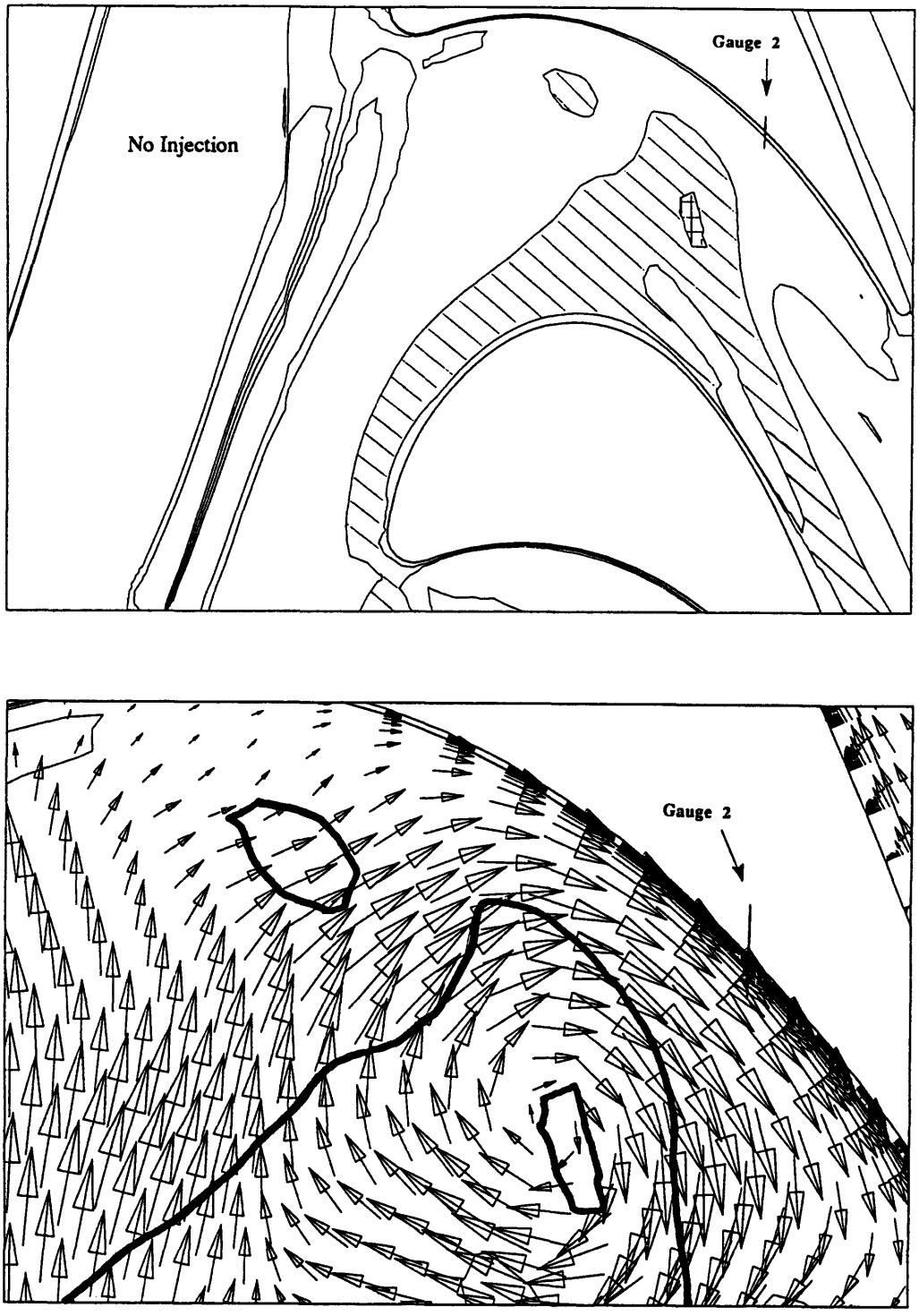

Figure (4.29a) : Contour Plots of UNSFLO Calculated Vorticity and Unsteady Velocity Vectors for the No Injection Case at Time=2

b)

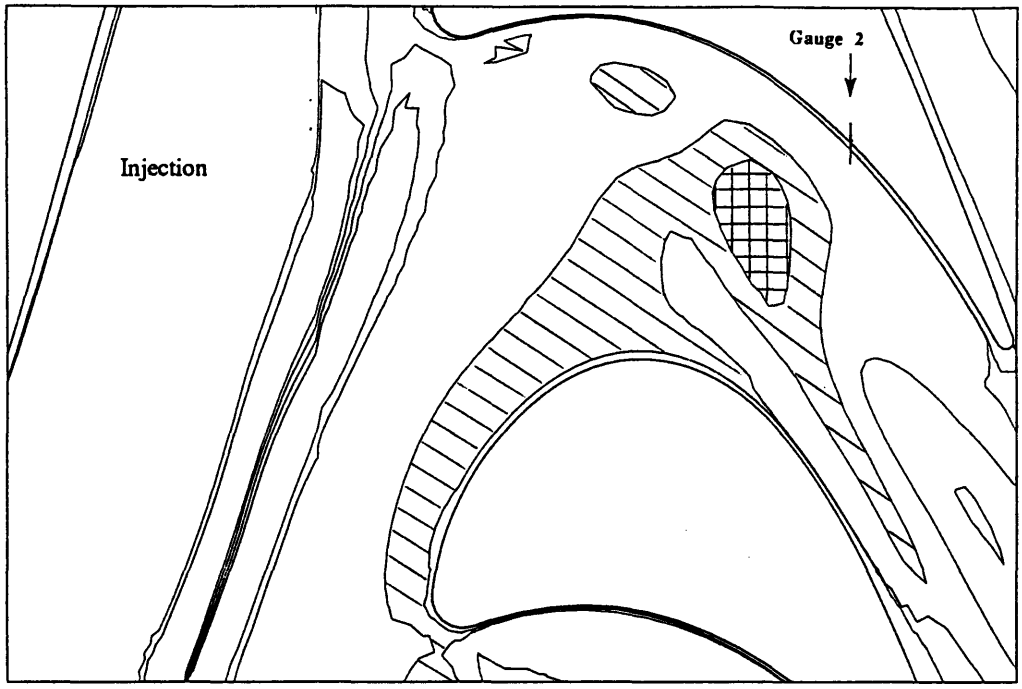

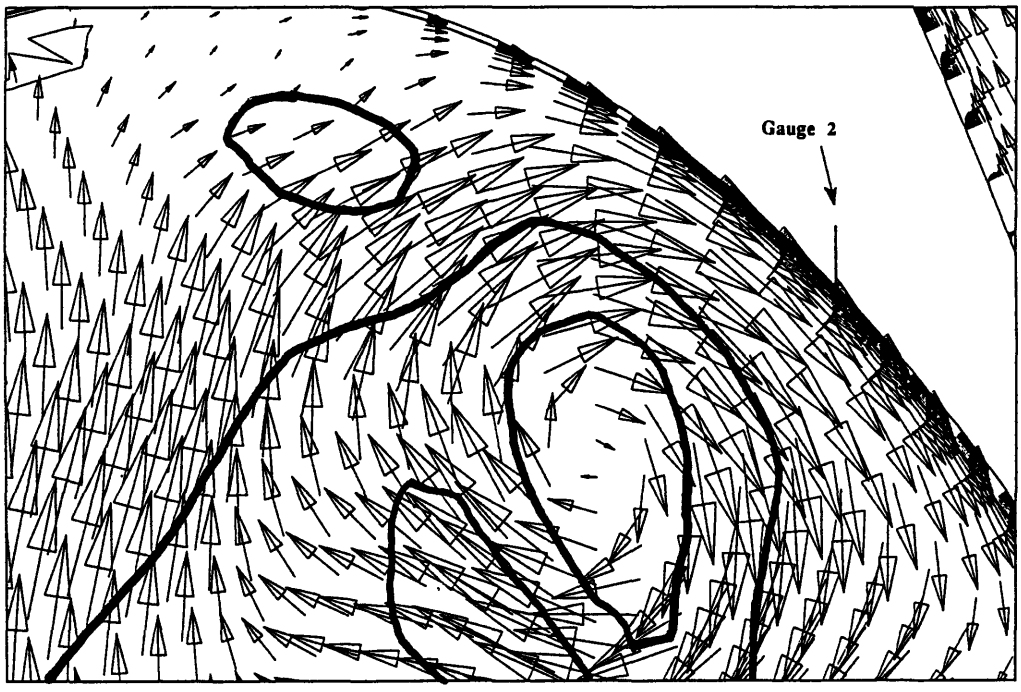

Figure (4.29b) : Contour Plots of UNSFLO Calculated Vorticity and Unsteady Velocity Vectors for the Injection Case at Time=2

a)

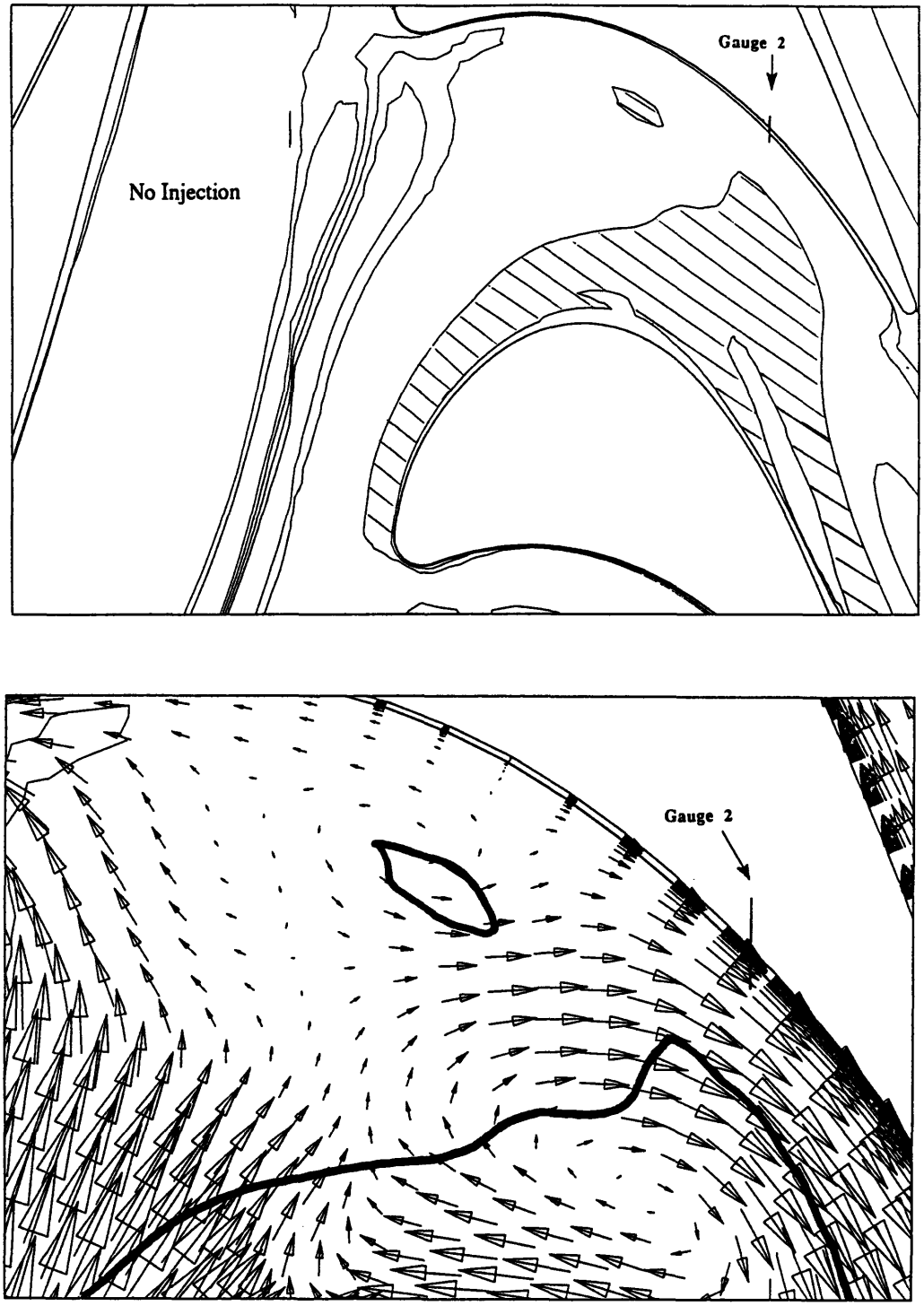

Figure (4.30a) : Contour Plots of UNSFLO Calculated Vorticity and Unsteady Velocity Vectors for the No Injection Case at Time=3

b)

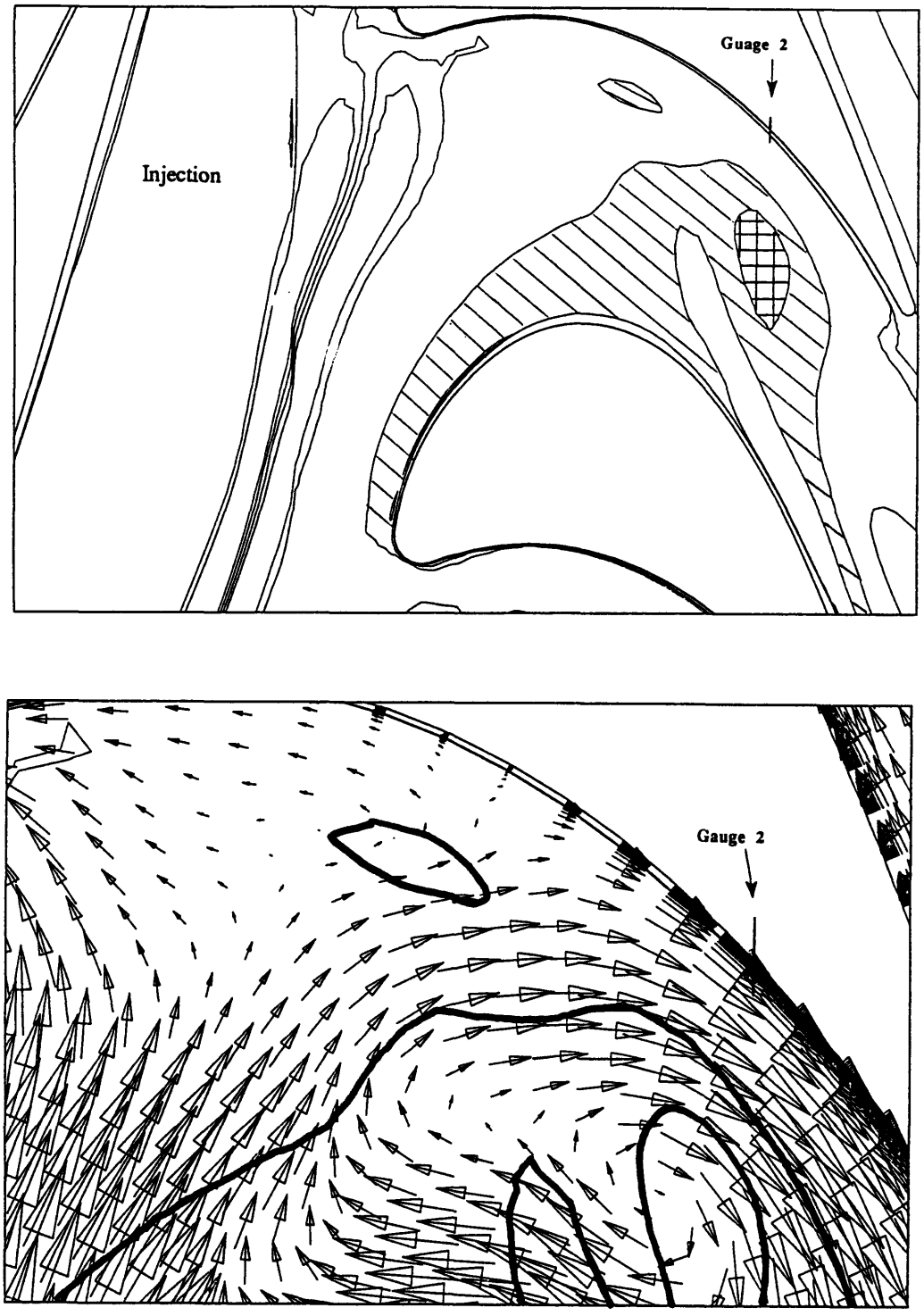

Figure (4.30b) : Contour Plots of UNSFLO Calculated Vorticity and Unsteady Velocity Vectors for the Injection Case at Time=3

a)

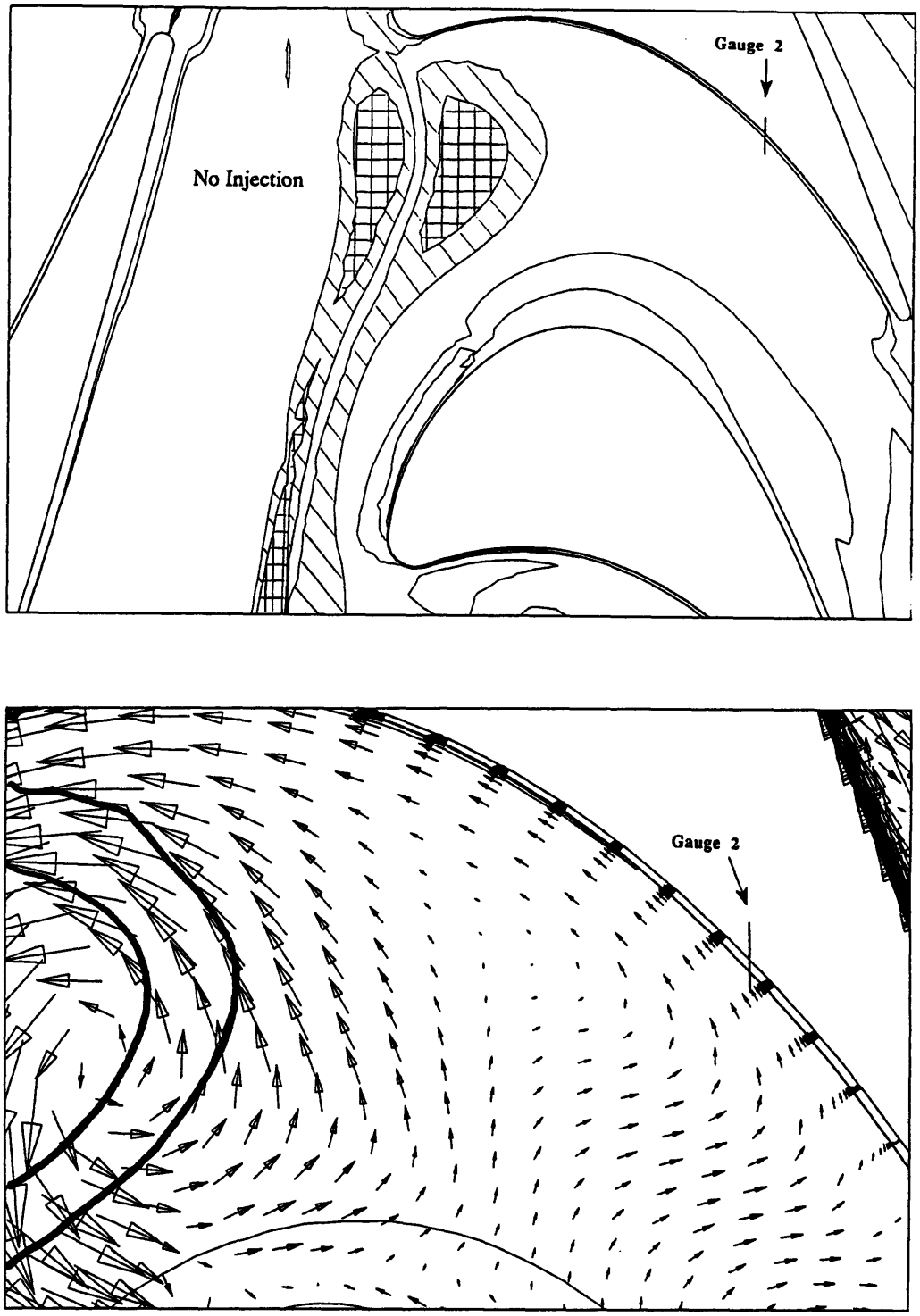

Figure (4.31a) : Contour Plots of UNSFLO Calculated Vorticity and Unsteady Velocity Vectors for the No Injection Case at Time=4

b)

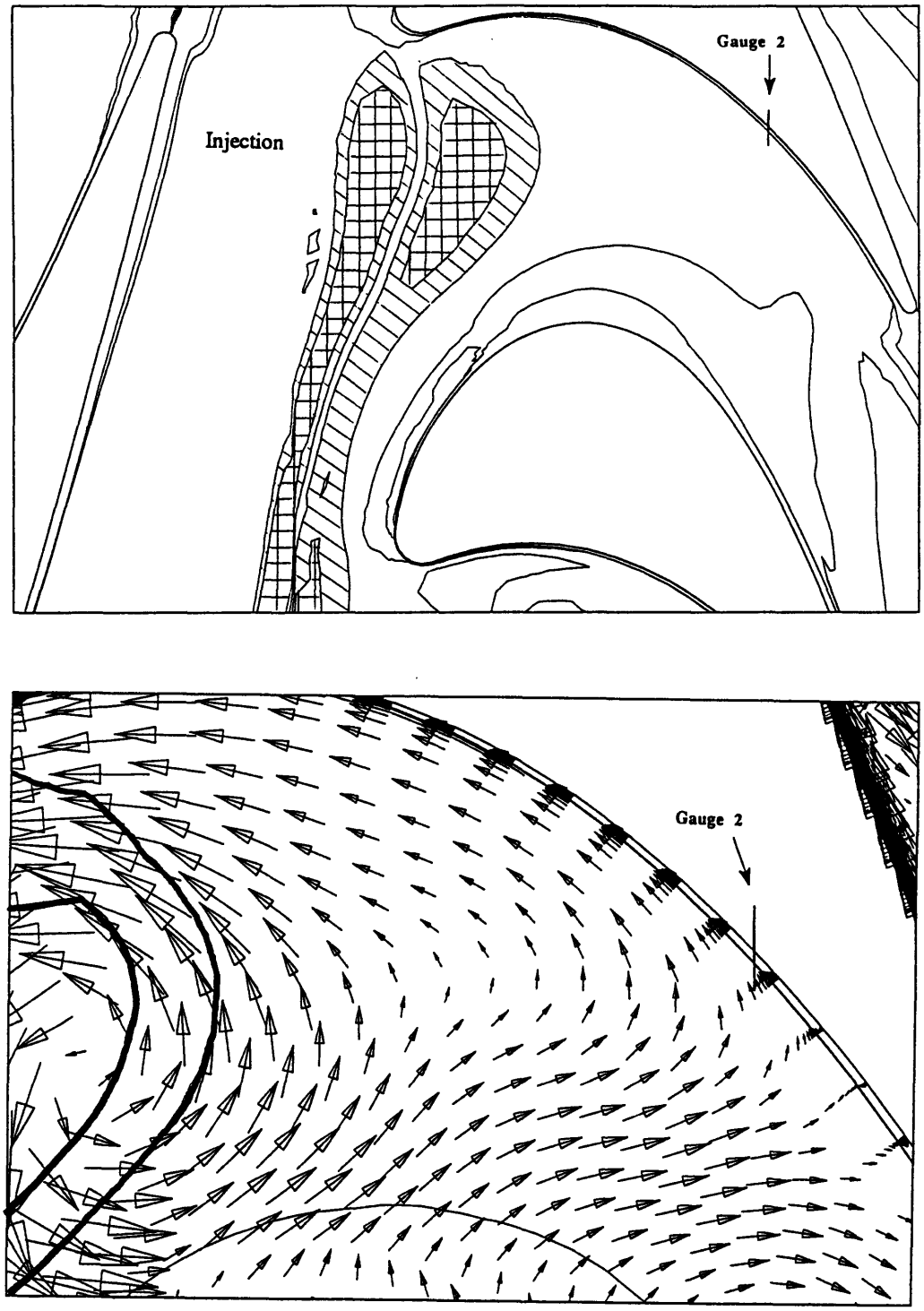

Figure (4.31b) : Contour Plots of UNSFLO Calculated Vorticity and Unsteady Velocity Vectors for the Injection Case at Time=4

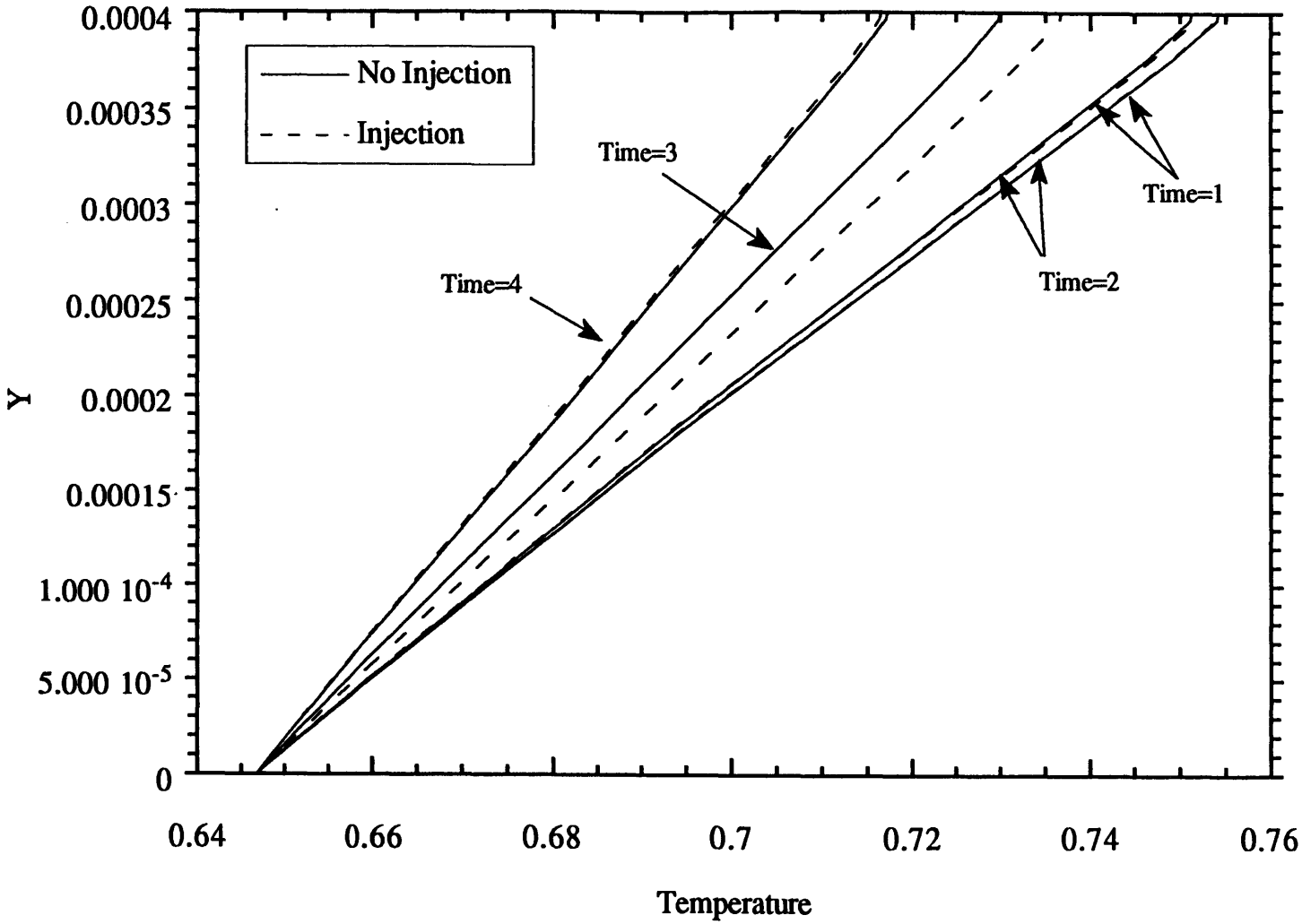

Figure (4.32) : Boundary Layer Profile of Temperature From the Wall to the First Grid Point Off the Wall

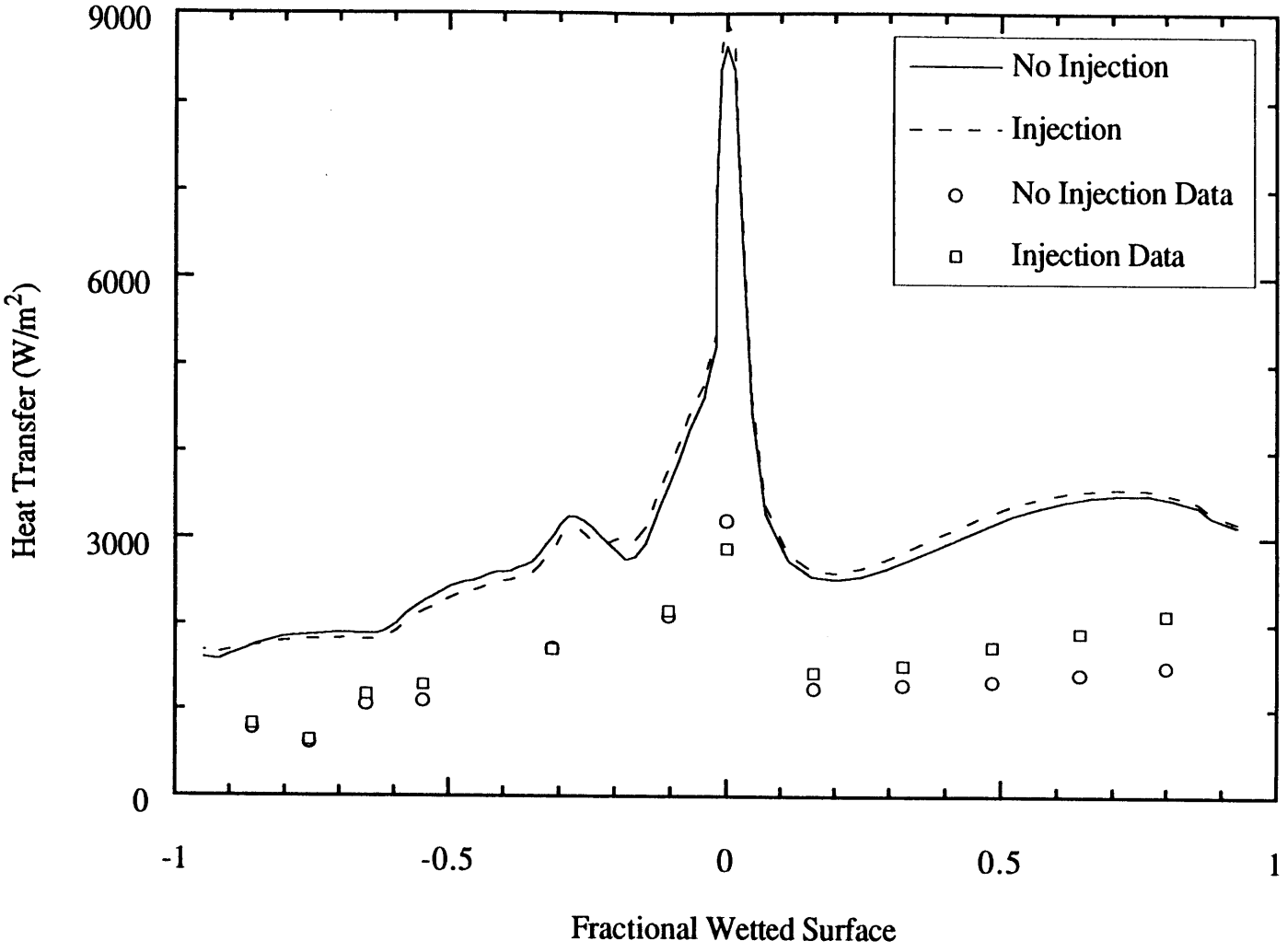

Figure (4.33) : Averaged Unsteady Heat Flux Versus Fractional Wetted Surface With and Without Coolant Injection For UNSFLO Calculated and Experimental Results

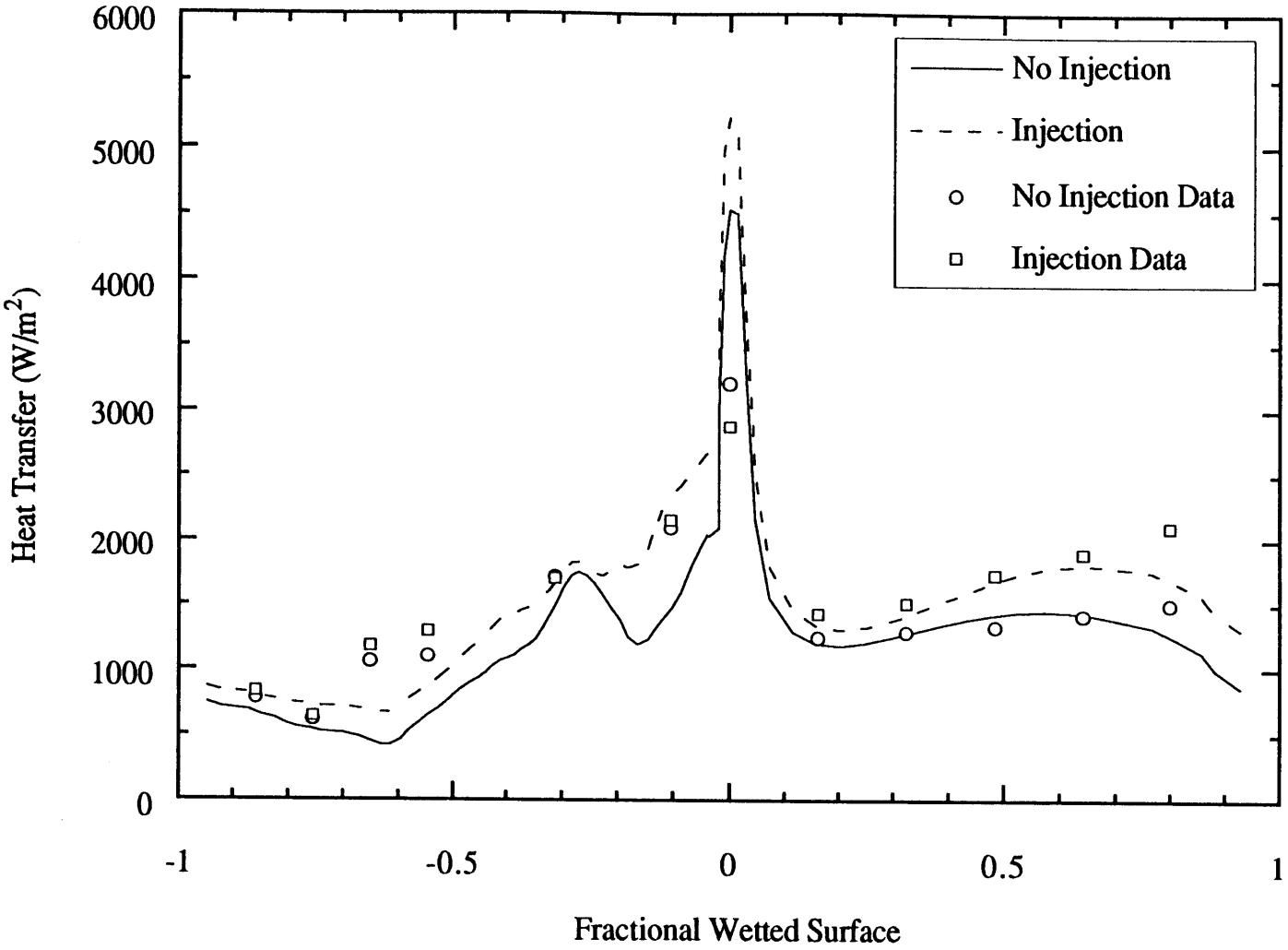

Figure (4.34) : Averaged Unsteady Heat Flux Versus Fractional Wetted Surface With and Without Coolant Injection Where the UNSFLO Rotor Blade Temperatures are Matched With Experimental Blade Temperatures

Table 2.1 : MIT Blowdown Turbine Facility Scaling

	Full Scale Engine	MIT Blowdown Facility
Fluid	Air	Argon-Freon 12
Ratio of Specific Heats	1.28	1.28
Coolant Fluid	Air	Argon-Freon 14
Coolant Ratio of Specific Heats	1.37	1.37
Coolant Mass Ratio	13%	13%
Mean Metal Temperature (T_m)	1118 K	295 K
Metal to Gas Temp. Ratio (T_m/T_g)	0.63	0.63
Inlet Total Temperature (T_g)	1780 K	478 K
Mean Coolant Temperature	790 K	212 K
True NGV Chord	8.0 cm	5.9 cm
Reynolds Number *	2.7×10^6	2.7×10^6
Inlet Pressure	19.6 atm	4.3 atm
Outlet Pressure	4.5 atm	1.0 atm
Outlet Total Temperature	1280 K	343 K
Prandtl Number	0.752	0.755
Rotor Speed	12,734 rpm	6,190 rpm
Mass Flow	49.00 kg/s	16.55 kg/s
Power	24,880 kW	1,078 kW
Test Time	Continuous	0.3 s

* Based on NGV Chord and Isentropic Exit Conditions

Table 2.2 : MIT Blowdown Turbine Facility Instrumentation

	Tanks			Test Section			
	Supply	Coolant	Dump	Upstream of NGV	On NGV	On Rotor	After the Rotor
Static Pressure	--	--	1	--	--	--	1
Main Gas Total Pressure	2	--	--	1	--	--	1-5
Main Gas Thermocouple	1	--	--	1	--	--	--
Metal Thermocouple	2	2	--	--	--	--	--
Coolant Gas Total Pressure	--	1	--	--	1	1	--
Coolant Gas Thermocouple	--	1	--	--	1	--	--
Tachometer	--	--	--	--	--	3	--
Heat Flux Gauges	--	--	--	--	--	13	--
Resistance Temperature Devices	--	--	--	--	--	1	1

-- Corresponds to No Instrumentation

Table 2.3 : Heat Flux Gauge Locations at Midspan (Uncooled Blades) [19]

	Sensor Number	Fractional Wetted Surface
	01	0.798
	02	0.641
Pressure Surface	03	0.484
	04	0.323
Length = 1.267 inches	05	0.161
	06	0.000
	07	-0.104
	--	-------
	09	-0.313
Suction Surface	10	-0.430
	11	-0.547
Length = 1.965 inches	12	-0.651
	13	-0.755
	14	-0.859

Fractional wetted surface uncertainty of measurements = ± 0.005 inches

-- Corresponds to a Failed Sensor

Table 2.4 : Data Acquisition Timing Sequence for the High Speed Channels

Start Time (ms)	End Time (ms)	Sampling Frequency (Hz)
0 *	250	20,000
250	550	200,000
550	1200	5,000
1200	600,000	50

* The Start Time of Zero Milliseconds Corresponds to the Opening of the Fast Acting Valve. Test Time Starts at the 250 Millisecond Mark.

Table 2.5a : Test Parameters for Uncooled Nozzle Guide Vane Tests at Mid-Span [19]

Test Number	T47	T50	T51	T52	T53
Initial Tunnel Temperature (C)	34.4	30.0	31.7	32.8	30.0
Inlet Total Temperature (K)	463	463	463	463	463
Inlet Total Pressure (Atm)	3.55	3.55	1.77	3.56	4.81
Exit Total Pressure (Atm)	0.86	0.96	0.43	0.83	1.16
Exit Static Pressure (Atm)	0.63	0.66	0.31	0.65	0.85
Mean Main Flow Gamma	1.28	1.28	1.28	1.28	1.28
Relative Total Temperature (K)	403	406	403	399	402
Rotor Inlet Mach Number*	0.68	0.85	0.68	0.46	0.67
Rotor Incidence* (Degrees)	60.5	63.2	60.5	51.0	60.3
Stage Pressure Ratio	4.12	3.70	4.11	4.27	4.15
Main Gas / Wall Temp Ratio	1.31	1.34	1.32	1.30	1.33

* At Rotor Blade Mid-Span Conditions

Table 2.5b : Ensemble Averaged Nusselt Numbers and Their Associated Uncertainty for the Uncooled Nozzle Guide Vane Tests at Mid-Span [19]

	T47	T50	T51	T52	T53
Sensor			Nusselt Number (Uncertainty*)		
1	1040 (57)	1469 (62)	434 (105)	994 (77)	1506 (61)
2	981 (83)	1464 (126)	487 (77)	876 (43)	1470 (71)
3	921 (76)	1163 (56)	484 (94)	848 (51)	1348 (64)
4	894 (95)	1038 (68)	465 (48)	844 (36)	1232 (43)
5	864 (43)	749 (34)	496 (75)	848 (28)	1168 (83)
6	2217 (161)	1897 (108)	1478 (119)	1730 (63)	2441 (99)
7	1448 (68)	1376 (85)	910 (38)	1240 (39)	1849 (64)
8	--	--	--	--	--
9	1189 (39)	1716 (70)	679 (111)	796 (25)	1486 (158)
10	973 (36)	--	--	--	--
11	765 (25)	1145 (49)	383 (83)	820 (41)	957 (70)
12	737 (25)	958 (31)	339 (38)	758 (39)	952 (34)
13	431 (17)	591 (32)	190 (53)	462 (18)	589 (28)
14	544 (18)	869 (39)	162 (33)	551 (17)	856 (38)

The Uncertainty Corresponds to the One Standard Deviation Uncertainty Level -- Corresponds to a Failed Sensor

Table 2.6a : Test Parameters for Cooled Nozzle Guide Vane Tests at Mid-Span [19]

Test Number	T55	T56	T57	T60	T61
Initial Tunnel Temperature (C)	26.8	23.9	25.5	28.7	34.3
Inlet Total Temperature (K)	458	463	465	460	502
Inlet Total Pressure (Atm)	3.46	3.48	3.45	3.49	4.71
Exit Total Pressure (Atm)	0.94	0.89	0.90	0.91	1.14
Exit Static Pressure (Atm)	0.75	0.68	0.68	0.69	0.92
Rotational Speed (RPS)	99	100	100	100	123
Mean Main Flow Gamma	1.28	1.28	1.28	1.28	1.24
Relative Total Temperature (K)	396	400	402	398	435
Rotor Inlet Mach Number*	0.57	0.57	0.57	0.57	0.48
Rotor Incidence* (Degrees)	56.7	56.7	56.7	56.7	52.5
Stage Pressure Ratio	3.67	3.89	3.84	3.82	4.13
Main Gas / Wall Temp Ratio	1.32	1.35	1.35	1.32	1.41
Vane Coolant Temperature (K)	282	290	296	273	293
Vane Coolant Pressure (Atm)	2.52	2.68	2.85	3.29	4.68
Coolant Gas Gamma	1.66	1.66	1.66	1.40	1.40
Coolant Gas / Wall Temp Ratio	1.61	1.60	1.63	1.72	1.73

* At Rotor Blade Mid-Span Conditions

Table 2.6b : Ensemble Averaged Nusselt Numbers and Their Associated Uncertainty for the Cooled Nozzle Guide Vane Tests at Mid-Span [19]

	T55	T56	T57	T60	T61
Sensor			Nusselt Number (Uncertainty*)		
1	1336 (168)	1332 (173)	1142 (66)	1341 (88)	1526 (47)
2	1191 (91)	1200 (153)	1187 (71)	1377 (203)	1778 (204)
3	1240 (118)	1097 (107)	951 (34)	1052 (82)	1488 (133)
4	1050 (101)	959 (55)	906 (30)	1235 (184)	1403 (111)
5	934 (65)	906 (65)	839 (31)	914 (46)	1416 (130)
6	2083 (168)	1822 (80)	1949 (77)	2236 (92)	2205 (241)
7	1372 (58)	1363 (43)	1278 (45)	1404 (46)	1567 (69)
8	--	--	--	--	--
9	1081 (45)	1080 (37)	1128 (96)	1113 (58)	1003 (48)
10	--	--	--	--	--
11	827 (25)	818 (26)	750 (40)	817 (28)	1125 (37)
12	740 (27)	747 (33)	684 (34)	710 (32)	1042 (52)
13	524 (30)	408 (12)	384 (13)	383 (20)	672 (32)
14	657 (33)	526 (33)	457 (20)	486 (22)	742 (30)

The Uncertainty Corresponds to the One Standard Deviation Uncertainty Level -- Corresponds to a Failed Sensor

Table 3.1 : UNSFLO Input Parameters for Hade Tests

NGV Inlet Angle	0 degrees
Ratio of Specific Heats	1.28
Metal to Gas Temp. Ratio (T_m/T_g)	0.6467
Inlet Total Temperature (T_g)	463 K
True NGV Chord	5.9 cm
Reynolds Number *	2.7×10^6
Stage Pressure Ratio	0.2433
Outlet Pressure	1.0 atm
Prandtl Number	0.761
Rotor Speed	6,190 rpm
NGV Suction Side Transition Point	0.5158
NGV Pressure Side Transition Point	0.6905

* Based on NGV Chord and Isentropic Exit Conditions

Table 4.1 : UNSFLO Input Parameters for No Injection Tests

NGV Inlet Angle	0 degrees
Ratio of Specific Heats	1.28
Metal to Gas Temp. Ratios (T_m/T_g)	0.6467, 0.59, 0.458
Inlet Total Temperature (T_g)	463 K
True NGV Chord	5.9 cm
Reynolds Number *	2.7×10^6
Stage Pressure Ratio	0.2433
Outlet Pressure	1.0 atm
Prandtl Number	0.761
Rotor Speed	6,190 rpm
NGV Suction Side Transition Point	0.5158
NGV Pressure Side Transition Point	0.6905

* Based on NGV Chord and Isentropic Exit Conditions

Table 4.2 : UNSFLO Input Parameters for Coolant Injection Tests

NGV Inlet Angle	0 degrees
Ratio of Specific Heats	1.28
Metal to Gas Temp. Ratios (T_m/T_g)	0.6467
Inlet Total Temperature (T_g)	463 K
True NGV Chord	5.9 cm
Reynolds Number *	2.7×10^6
Stage Pressure Ratio	0.2433
Outlet Pressure	1.0 atm
Prandtl Number	0.761
Rotor Speed	6,190 rpm
NGV Suction Side Transition Point	0.5158
NGV Pressure Side Transition Point	0.6905
Coolant Mass Flow	3% of Mainflow
Coolant Injection Angle	45 degrees
Coolant Slot Location	X=0.91 to 0.94
Coolant Velocity	80% of Mainflow

* Based on NGV Chord and Isentropic Exit Conditions